RADC-TR-76-406
Interim Technical Report
December 1976
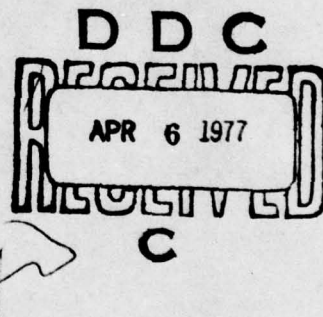
ADVANCED CONCEPTS OF MICROWAVE GENERATION
AND CONTROL IN SOLIDS

Cornell University
School of Electrical Engineering

DDC

APR 6 1977

C

ROME AIR DEVELOPMENT CENTER
AIR FORCE SYSTEMS COMMAND
GRIFFISS AIR FORCE BASE, NEW YORK 13441

G. C. Dalman, L. F. Eastman, C. A. Lee, J. Frey and W. Ku
are the co-responsible investigators for this contract. Sven
Roosild (ETSD), is the RADC Project Engineer.

This report has been reviewed by the RADC Information Office (OI)
and is releasable to the National Technical Information Service (NTIS).
At NTIS it will be releasable to the general public, including foreign
nations.

This technical report has been reviewed and approved for publication.

APPROVED: *Sven A. Roosild*

        SVEN A. ROOSILD
        Project Engineer

APPROVED: *Robert M. Barrett*

        ROBERT M. BARRETT
        Director
        Solid State Sciences Division

FOR THE COMMANDER: *John P. Huss*

                      Plans Office

REPORT DOCUMENTATION PAGE	READ INSTRUCTIONS BEFORE COMPLETING FORM

1. REPORT NUMBER	2. GOVT ACCESSION NO.	3. RECIPIENT'S CATALOG NUMBER
RADC-TR-76-406		

4. TITLE (and Subtitle)	5. TYPE OF REPORT & PERIOD COVERED
ADVANCED CONCEPTS OF MICROWAVE GENERATION AND CONTROL IN SOLIDS	Biannual Report No. 5
	6. PERFORMING ORG. REPORT NUMBER

7. AUTHOR(s)	8. CONTRACT OR GRANT NUMBER(s)
G. C. Dalman J. Frey L. F. Eastman W. Ku C. A. Lee	F30602-74-C-0001

9. PERFORMING ORGANIZATION NAME AND ADDRESS	10. PROGRAM ELEMENT, PROJECT, TASK AREA & WORK UNIT NUMBERS
Cornell University Ithaca, New York 14853	62702F 2305J101

11. CONTROLLING OFFICE NAME AND ADDRESS	12. REPORT DATE
Deputy for Electronic Technology(RADC) Hanscom AFB, Massachusetts 01731 Monitor/Sven A. Roosild/ETSD	December 1976
	13. NUMBER OF PAGES
	156

14. MONITORING AGENCY NAME & ADDRESS(if different from Controlling Office)	15. SECURITY CLASS. (of this report)
	Unclassified
	15a. DECLASSIFICATION/DOWNGRADING SCHEDULE

16. DISTRIBUTION STATEMENT (of this Report)

Approved for public release; distribution unlimited.

17. DISTRIBUTION STATEMENT (of the abstract entered in Block 20, if different from Report)

18. SUPPLEMENTARY NOTES

19. KEY WORDS (Continue on reverse side if necessary and identify by block number)

IMPATT diodes
Parameters
TRAPATT device-circuit
Microwave FET
Broadband GaAs FET amplifier

20. ABSTRACT (Continue on reverse side if necessary and identify by block number)

The work accomplished during the fifth biannual period of the program is discussed in this report. Included are: GaAs Read Diodes; Small and Large-Signal Effects on IMPATT Diodes; Measurement of Read and IMPATT Diode Amplifier Parameters; Computer Simulation of TRAPATT Device-Circuit Interactions; High Power, High Efficiency CW TEO's; Automated Network Analyzer; Microwave FET Fabrication Studies; Investigation of Ion Implanted Silicon Read IMPATT Diodes; Broadband GaAs FET Amplifier Study; Optimum

DD FORM 1 JAN 73 1473   EDITION OF 1 NOV 65 IS OBSOLETE

Design of Broadband IMPATT Reflection Amplifiers; The Growth and
Evaluation of Thin GaAs Layers for Use in Microwave FET's;
Experimental and Theoretical Studies of Ion Implanted Silicon Read
IMPATT Diode.

PERSONNEL

Faculty

G. C. Dalman, Professor
C. A. Lee, Professor
L. F. Eastman, Professor
Jeffrey Frey, Assoc. Professor
W. Ku, Professor

Staff

P. Lumbard, Technician
A. Schwoeble, Secretary

Graduate Students

Berenz, John

*Bogan, Zeev

Gupta, Aditya

Gurney, Richard

*Herlihy, Gary

Kwor, Richard

McClymonds, James

*Morkoc, Hadis

*Petersen, Wendell

*Souza, Rui

Sutherland, Jack

Wu, Jing-Shown

*Contributors not supported by contract funds.

TABLE OF CONTENTS

*Project Supervisor

v

PREFACE

This is the fifth biannual progress report on research conducted at the School of Electrical Engineering, Cornell University, under Contract F30602-74-C-0001, Job Order Number 55730383. The research is under the overall direction of G. C. Dalman, L. F. Eastman, C. A. Lee, J. Frey and W. Ku. The results of research for the period 1 November 1975 to 30 April 1976 are discussed.

The RADC Project Engineer is R. H. Chilton (OCTE).

The major objective of this contract is to perform research and development in advanced techniques of microwave power generation and control in solids. It is intended that the devices resulting from this effort will be competitive with or replace microwave tubes at low and medium power levels. The new areas of application whose feasibility could not be evaluated in advance were also studied. It is expected that these solid state sources will be widely used in future microwave systems.

This report presents progress in the research and development of microwave solid state devices and circuits. The devices include avalanche devices, transferred electron devices, and field effect transistors.

INTRODUCTION

This program is concerned with research and development of solid state microwave signal generators and amplifiers. The emphasis of the investigation is centered on studies of active microwave effects in avalanche diodes, transferred electron diodes, microwave field-effect transistors, and on related microwave circuit, materials growth, and physical electronic techniques. The program is being undertaken to further the understanding of the physical mechanisms and processes which are involved. The main objective is to obtain information of use in the design of improved solid state microwave devices and is directed toward the eventual inclusion of these devices in advanced microwave systems such as are required for communications, detection, and other related applications.

The work accomplished during the fifth biannual period of the program is discussed in this report. Included are: GaAs Read Diodes; Small and Large-Signal Effects on IMPATT Diodes; Measurement of Read and IMPATT Diode Amplifier Parameters; Computer Simulation of TRAPATT Device-Circuit Interactions; High Power, High Efficiency CW TEO's; Automated Network Analyzer; Microwave FET Fabrication Studies; Investigation of Ion-Implanted Silicon Read IMPATT Diodes; Broadband GaAs FET Amplifier Study; Optimum Design of Broadband IMPATT Reflection Amplifiers; The Growth and Evaluation of Thin GaAs Layers for Use in Microwave FET's; Experimental and Theoretical Studies of Ion-Implanted Silicon Read IMPATT Diode.

GaAs READ DIODES

J. Berenz, G. C. Dalman,* C. A. Lee*

Introduction

Several factors which affect the performance of GaAs
Read diodes are explored in greater detail. The relatively
large reverse saturation current previously reported is
shown to originate mainly from the narrow band-gap
platinum arsenide ($PtAs_2$) which forms the Schottky-barrier
junction. A comparison between reached-through and not-
reached-through diode types is presented to illustrate the
effect this parameter has on diode performance. For
example, a not-reached-through diode, which performs as
high-power, high-efficiency oscillator, suffers from a
greater degree of phase distortion than a comparable
reached-through diode when employed as a reflection
amplifier. The reached-through diode on the other hand,
exhibits a lower dc-to-rf conversion efficiency. The
fundamental differences between these two diode types
are explored using dc, microwave small-signal admittance,
and low-frequency noise measurements. The results are
interpreted in terms of the "Quasi-static" theory.

*Project Supervisor

The results of measurements of the impedance presented
to the diode by the circuit at low frequencies are presented
to illustrate the differences between bias circuit designs.
The effect of this impedance on the stability of the diode at
low frequencies is illustrated by low-frequency noise measure-
ment results. Since the reactance of the diode at low fre-
quencies can be either capacitive or inductive, depending upon
the bias current and frequency, proper design of the bias
circuit impedance is shown to be an important consideration.

Finally, this report concludes with plans for further
study.

Origins of I_S

Previously we reported that the small-signal properties
of GaAs Read diodes were governed by low values of multiplica-
tion, and, therefore, by a relatively large reverse saturation
current, I_S. The large signal properties of these diodes may
also be explained in terms of a large I_S. Thus, it is important
to understand the origins of I_S, in order to be able to control
this parameter in a reproducible manner. Two sources of I_S
are described in this report.

1. The Schottky-Barrier Contact

All of the GaAs diodes employed in this study have platinum
(Pt) Schottky-barrier contacts. It is well known that platinum
reacts with GaAs at relatively low temperatures to form a
variety of Pt-Ga and Pt-As compounds.[1] Several authors have
reported a layered GaPt-PtAs$_2$-GaAs interface.[1,2] We elected
to study the composition of the Schottky-barrier contact
employed on GaAs Read diodes which have performed as high
efficiency oscillators.

The following analysis was performed using a Raytheon
GaAs Read diode. The GaAs mesa was removed from its platinum
contact by etching in sulfuric-peroxide solution. Figure 1
presents a photograph of the Pt surface after the GaAs mesa
has been removed. As can be seen, the Pt served to replicate
the original GaAs crystal surface. The circular outline of
the removed GaAs mesa is clearly evident in the photograph.
This circular area is higher than the surrounding Pt as
indicated by a "Talystep" measurement. This height is pro-
portional to the amount of intermetallic compounds formed
during processing and operation of the diode. Characteristically,
more alloying occurs around the outer periphery of the mesa,
where the heat flux is greater due to the temperature and
current distribution across the solid-circular area of the
diode.[3]

In order to study the composition of the alloyed region,
Secondary Ion Mass Spectrometry (SIMS) was employed to obtain
an in-depth profile of the constituent elements present in the alloyed
area.[4] In the SIMS technique a primary ion beam of oxygen is
used to erode the sample surface over a 250 square micron area
by sputtering.[5] The resulting secondary ions which are
produced as a result of this interaction are mass-analyzed and
detected. Thus, it is possible to obtain a profile of the
relative concentration of an element with depth into the sample.
This process is schematically depicted in Figure 2. The
resulting in-depth profiles are presented in Figures 3(a)
and (b).

The profiles show that the relative concentrations of
both Pt and As (arsenic) rapidly increase from low levels at
the surface to their maximum values and then decrease again
with increasing depth to very low levels (effectively zero
beyond the titanium (Ti) layer). The depletion of Pt and
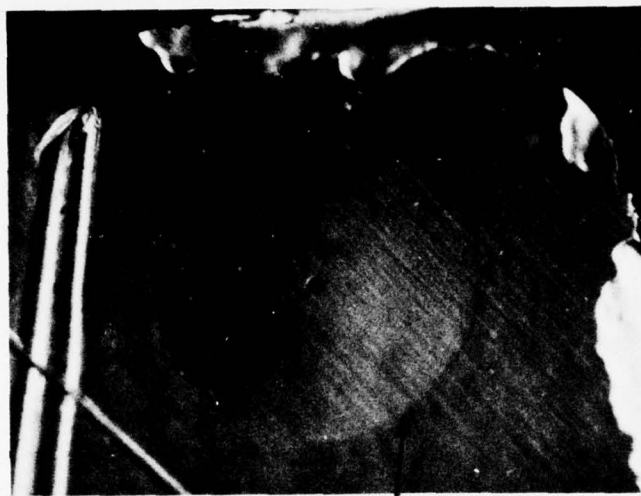
Pt-GaAs
ALLOYED AREA
EXPOSED BY
REMOVAL OF
GaAs MESA

Figure 1. Photograph of Pt Schottky-barrier Metallization
after Removal of GaAs Mesa (Diameter ≈ 250
microns). Top View.

4

Secondary Ion Beam (+ and −)

Primary O_2^+
Ion Beam

Pt-GaAs alloy

Pt (200Å)
Ti (1000Å) } sputtered
Au (2000Å)

Au plated heatsink
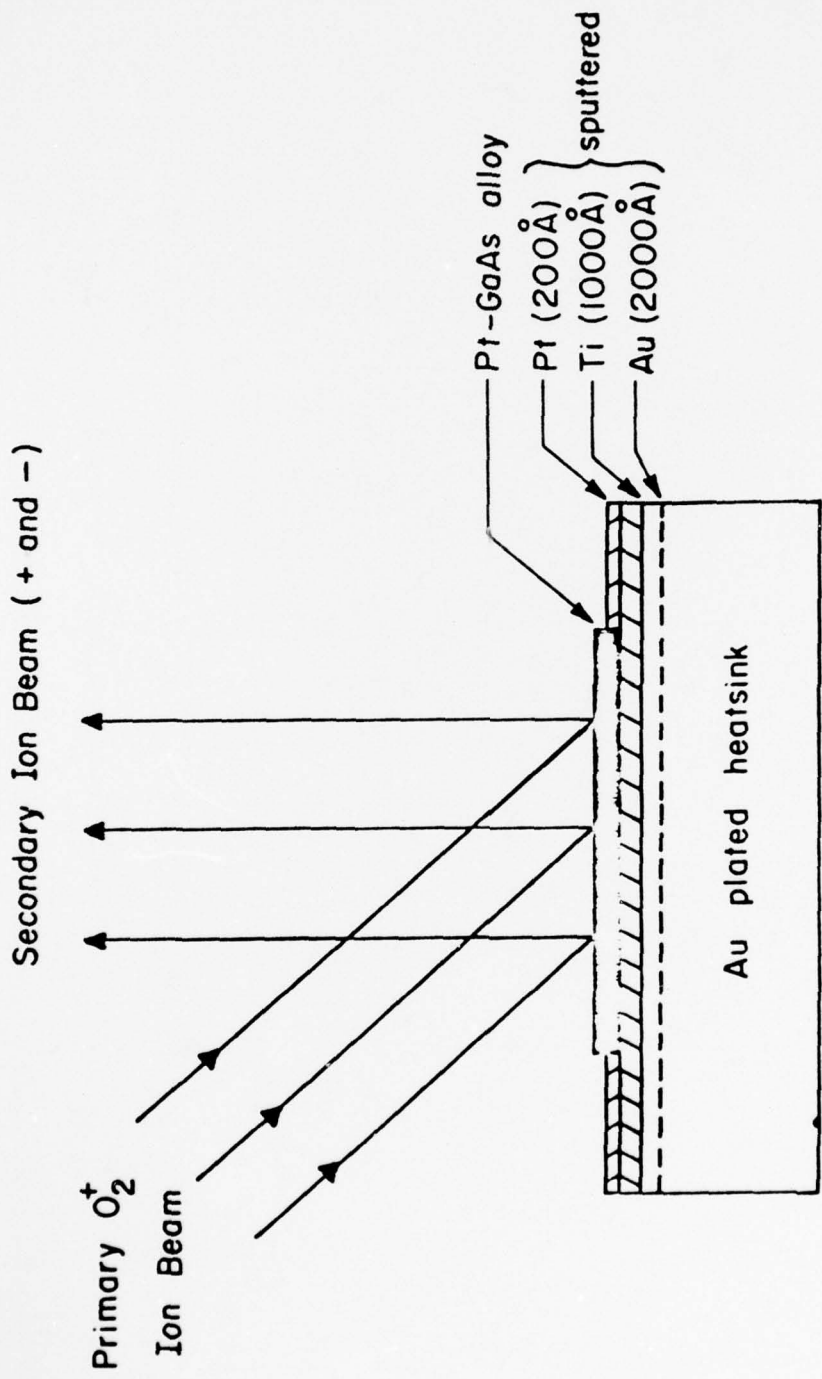
Figure 2. SIMS Analysis of Schottky-barrier Metallization – Sputtering Geometry. Cross-section.

ELEMENT1 - 195PT
ELEMENT2 - 197AU
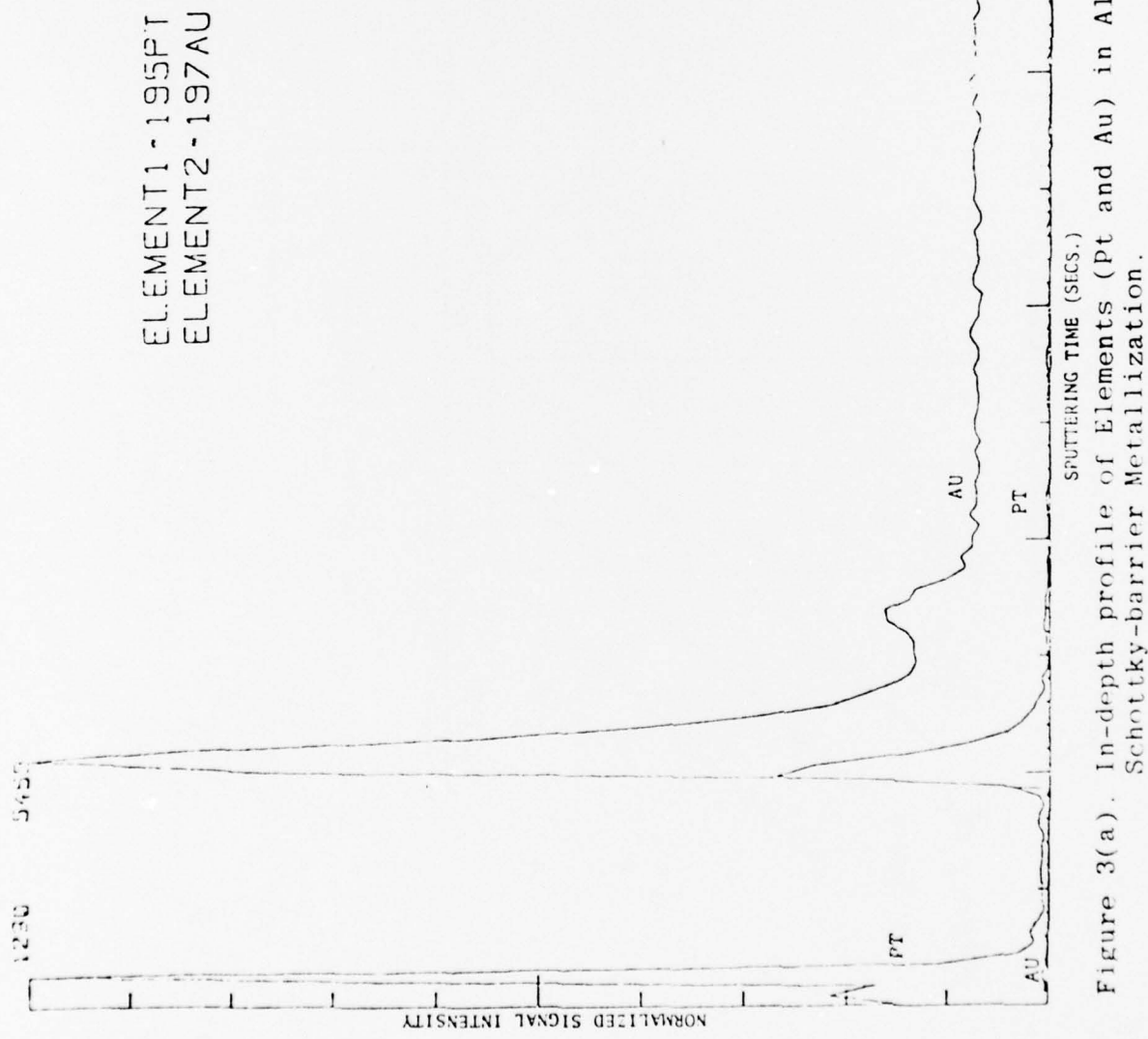
Figure 3(a). In-depth profile of Elements (Pt and Au) in Alloyed area of
Schottky-barrier Metallization.

SPUTTERING TIME (SECS.)

NORMALIZED SIGNAL INTENSITY

6

ELEMENT1 - 48TI
ELEMENT2 - 75AS
ELEMENT3 - 69GA
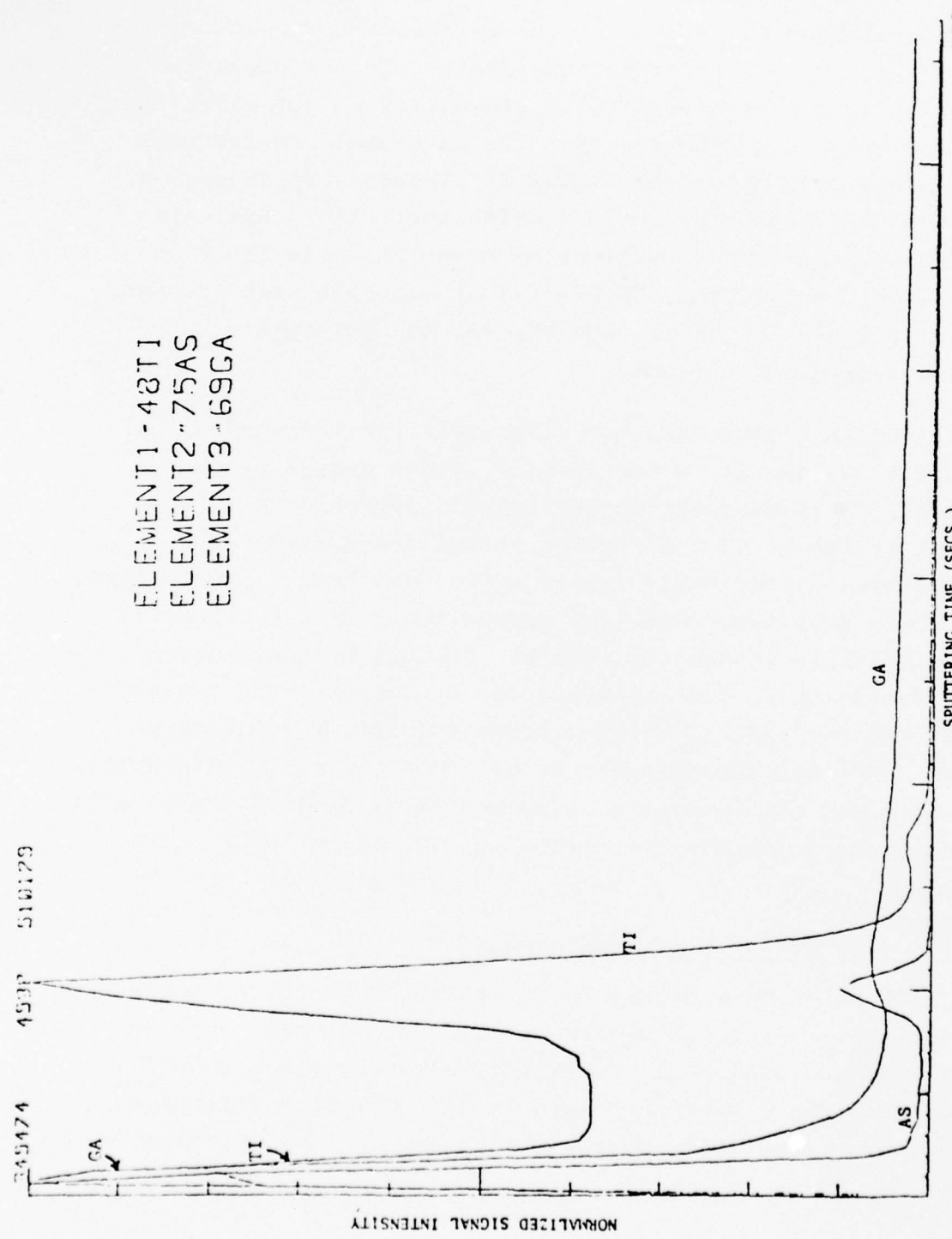
Figure 3(b)   In-depth Profile of Elements (Ti, Ga, and As) in Alloyed
Area of Schottky-barrier Metallization.

SPUTTERING TIME (SECS.)

NORMALIZED SIGNAL INTENSITY

GA

TI

AS

GA

TI

7

As at the surface is due to the etchant preferentially re-moving $PtAs_2$, leaving a gallium (Ga) rich surface. The Ga concentration is maximum at the surface and decreases (but not to zero) with increasing depth. This implies that the titanium is not effective in preventing Ga out-diffusion from the interface. Notice that the Ga signal remains near its maximum even after the Pt and As signals have decreased. This behavior supports the contention that $PtAs_2$ nucleates at the interface as a result of Ga dissolution in the Pt (and Ti). Thus, $PtAs_2$ forms the electrical junction with the GaAs, and, we believe, it is responsible for the relatively large reverse saturation current.

$PtAs_2$ is a semiconductor with an intrinsic band-gap of about 0.5 eV, and it is degenerately doped p-type by the gallium.[6] This band-gap energy closely corresponds to the activation energy of the reverse saturation current with temperature as previously reported for GaAs Read diodes. Thus, it appears that the conduction mechanism in this contact is very similar to conduction in a p-n Ge-GaAs heterojunction[7]. This contention is further supported by the observed variation in reverse current, I_R, with reverse voltage, V_R, for these diodes. The reverse current varies according to: $I_R = AV_R \exp(BV_R)$, where A and B are constants which may be determined empirically. The dominant conduction mechanism appears to be field emission.

2. The Effect of Reach-Through

Although a more detailed comparison of reached-through and not-reached-through diodes is given in the next section, it is germane to discuss the effect reach-through has on I_s in this section. Once the electric field reaches through to the higher conductivity buffer layers any further increase in

voltage across the diode will result in an increase in the field strength at this interface. Experimentally, I_R is observed to increase faster than the heterojunction expression when reach-through occurs. This is illustrated by the data presented in Figure 4 for a Read diode which reaches-through before break-down. One possible source of this "excess" current is trapping centers due to misfit dislocations at the buffer-active layer interface. Another possible explanation is once reachthrough occurs the field at the Schottky-barrier junction increases more rapidly than when the diode is not-reached-through, and this in turn increases I_R. Without performing additional experiments it is not possible to more closely identify the source of this "excess" current.

Reach-Through Versus Not-Reach-Through

1. Diode Description

The available single mesa L-H-L GaAs Read diodes have been surveyed using C-V profiling to identify the reach-through and not-reach-through types. Only one diode, 637A-24Q, was found to clearly reach-through before breakdown. This diode, and a not-reach-through diode, 647A-11J, were selected for further study.

The measured doping profiles of these diodes are presented in Figure 5 in order to show the magnitude and position of the donor spike in the material. The distance, x_p, of the donor spike from the junction essentially determines the width of the avalanche zone, and together with the integrated charge in the spike, determines the width of the depletion region in the lower doped material. The total width of the lower doped material then determines whether or not a diode reaches through before breakdown.
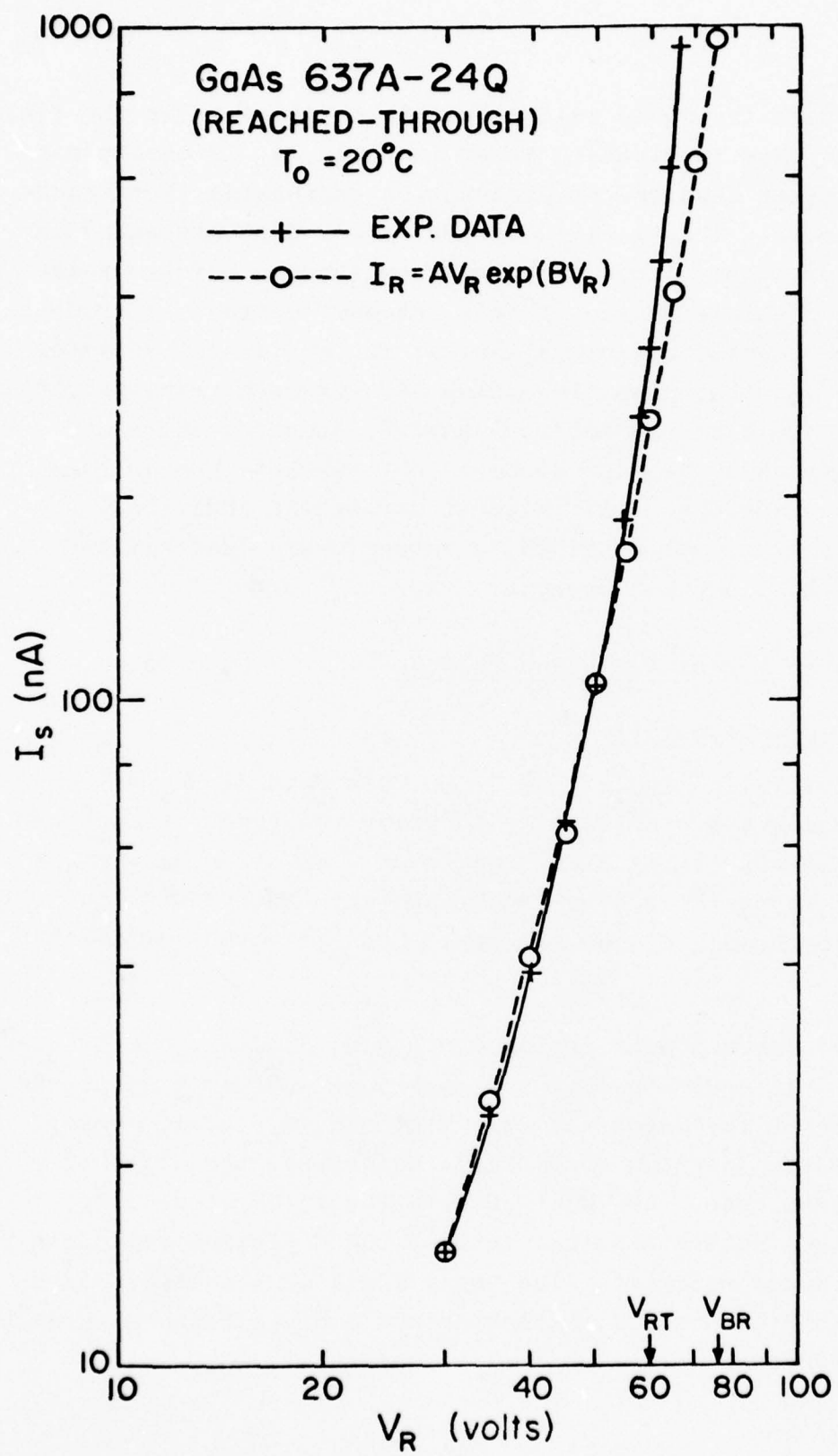
9

Figure 4. Reverse Saturation Current as a Function of Reverse Voltage Below Breakdown for GaAs 637A-24Q. $A=5.77 \times 10^{-11}$ ohms^{-1} and $B = .072$ v^{-1}
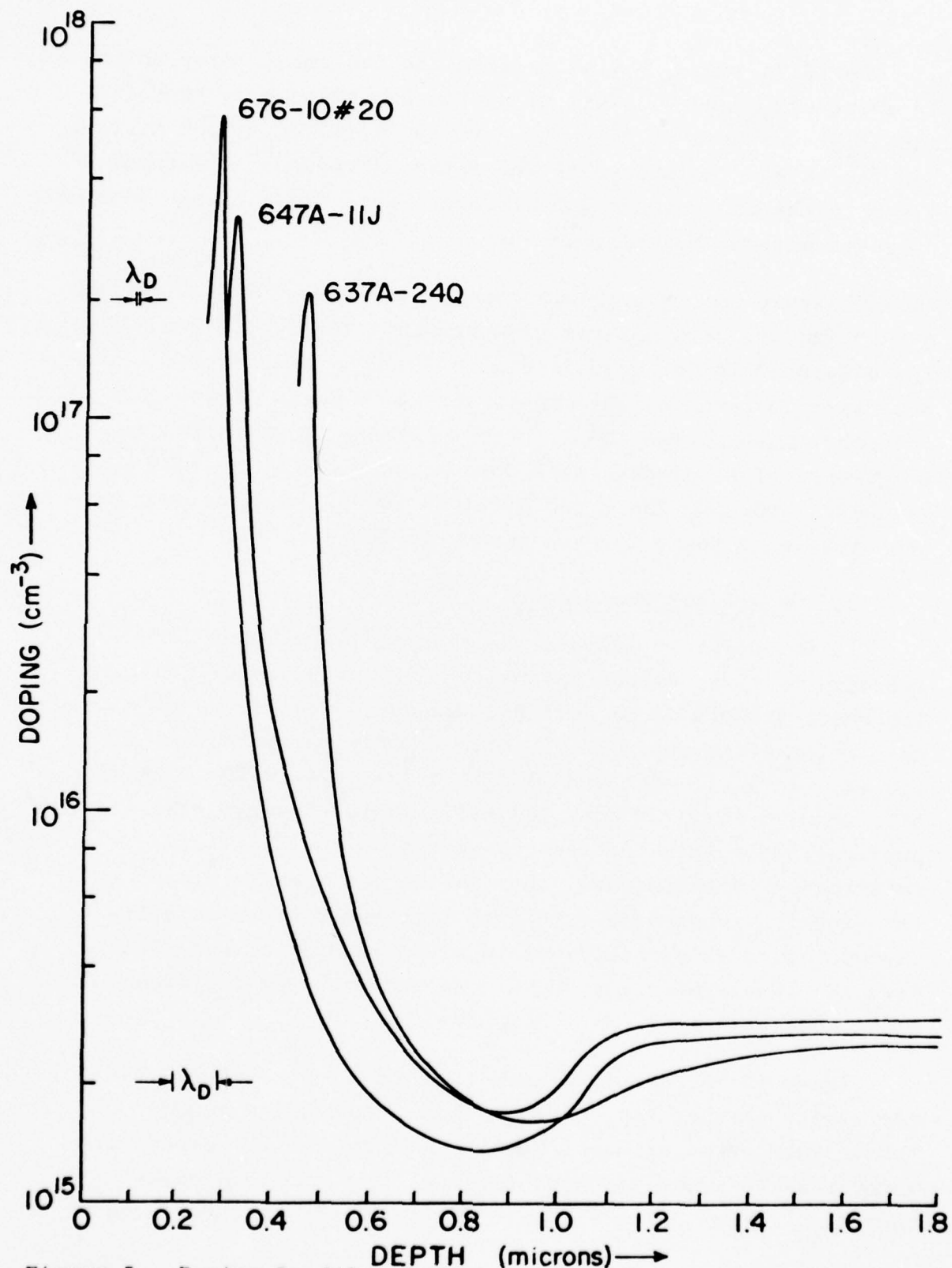
Figure 5. Doping Profiles Computed from C-V Measurements on GaAs Read Diodes Employed in This Study.

11

For 637A-24Q $x_p \cong 0.47$ microns and the total layer thickness is about 5.3 microns. This diode reaches through at 60 volts, and it breaks down at 76 volts. For 647A-11J, $x_p \cong 0.32$ microns, and the integrated charge in the spike is larger. The total layer thickness is about 7.5 microns. This diode breaks down at 60 volts without reaching through.

Contrary to our previous report, the diodes 676-10 #2 and 676-10 #20 are both not-reached-through. The doping profile for 676-10#20 is included in Figure 5. x_ρ, in this case, is 0.27 microns, and the integrated charge is again larger than the other diodes. The total layer thickness is greater than 8 microns. This diode breaks down at about 70 volts without reaching through. The diode 676-10#2 is very similar, except that the donor spike is even closer to the junction.

2. Oscillator Performance

It is useful to compare the reported oscillator performance of these diodes against the measured doping profiles.[8] The reach-through diode 637A-24Q has the lowest dc-to-rf conversion efficiency, 13.5%, with 1.75W power output at I = 140 mA. 647A-11J achieved 2W with 18%; 676-10#20: 2.5W with 21%; and 676-10#2: 3W with 26% efficiency. Clearly, the doping profile has a pronounced effect on the oscillator performance of the diodes. Moving the donor spike closer to the junction appears to result in improved conversion efficiency. This is probably due to a combination of beneficial effects: a narrower avalanche zone and enhanced depletion width modulation.

There is an additional reported difference between the oscillator performance of reach-through and not-reached-through GaAs Read diodes. Namely, reached-through diodes are more prone to tuning induced failures than the not-reach-through. These tuning failures are usually associated with

12

low-frequency bias circuit oscillations. One factor which influences the threshold of these oscillations is the space-charge resistance of the diode. Figure 6 presents the measured space charge resistance of the reach-through and not-reached-through diodes. Clearly, the not-reach-through diode has a much larger space charge resistance. We believe this larger space charge resistance acts as built-in protection against tuning induced failures.[9]

3. Amplifier Performance

Unfortunately the enhanced depletion width modulation of the not-reached-through diodes is not beneficial to reflection amplifier performance, since it introduces an additional component of electronic susceptance which contributes to phase distortion. In order to illustrate this point, the microwave small-signal admittance of reach-through and not-reach-through diodes was measured under comparable experimental conditions. Measurements were performed using the automatic network analyzer (ANA) technique described in the previous report. The results are presented in Figures 7 and 8. The differences, particularly at the highest current density, are most dramatic.

At comparable current density, the not-reach-through diode's negative conductance is more compressed with respect to its total susceptance than the reach-through diode. This would explain the previously reported difficulty in fitting the "Quasi-static" impedance equation to the experimental G-B data for diode 676-10#2. The "Quasi-static" theory employs a simple transport factor to describe the drift region of the diode. It does not take into account the effect of non-saturated drift velocity, and in particular, the effect of negative differential mobility in GaAs.

The other interesting feature of the not-reach-through
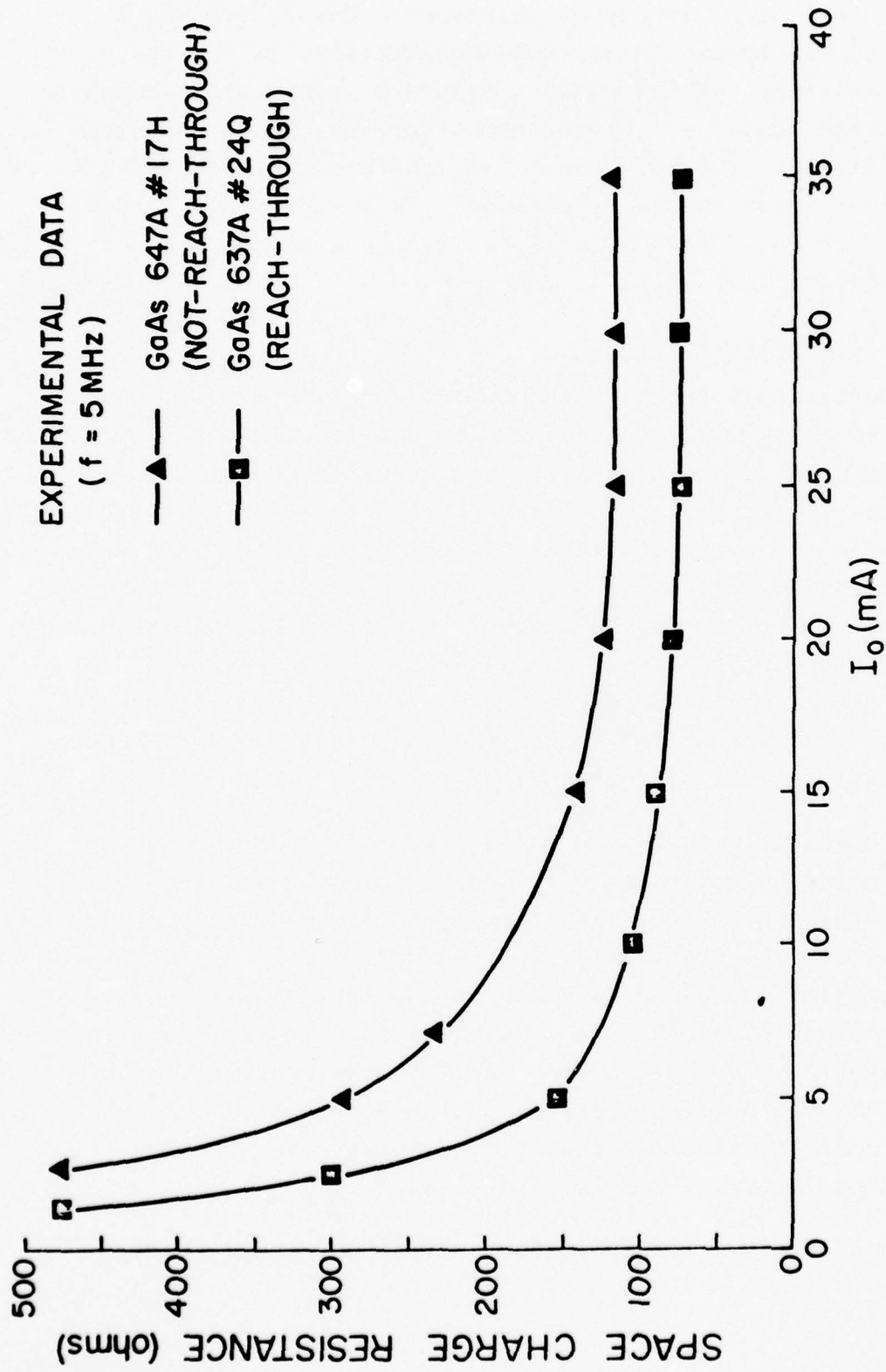
13

Figure 6. Space Charge Resistance of Reached-Through and Not-Reached-Through GaAs Read Diodes as a Function of Bias Current.
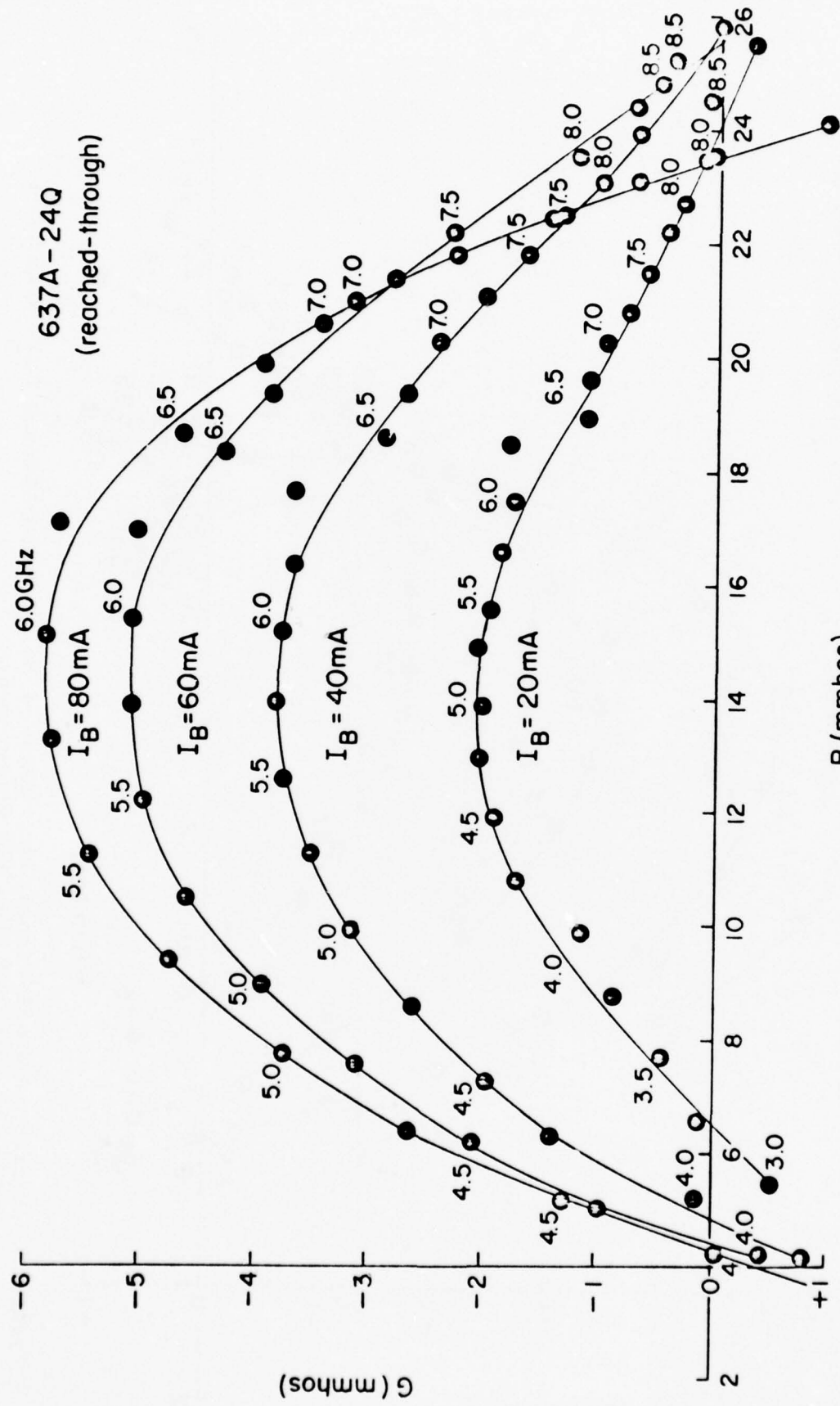
Figure 7. Microwave Small-Signal Admittance of Reached-Through GaAs Read Diode 637A-21;
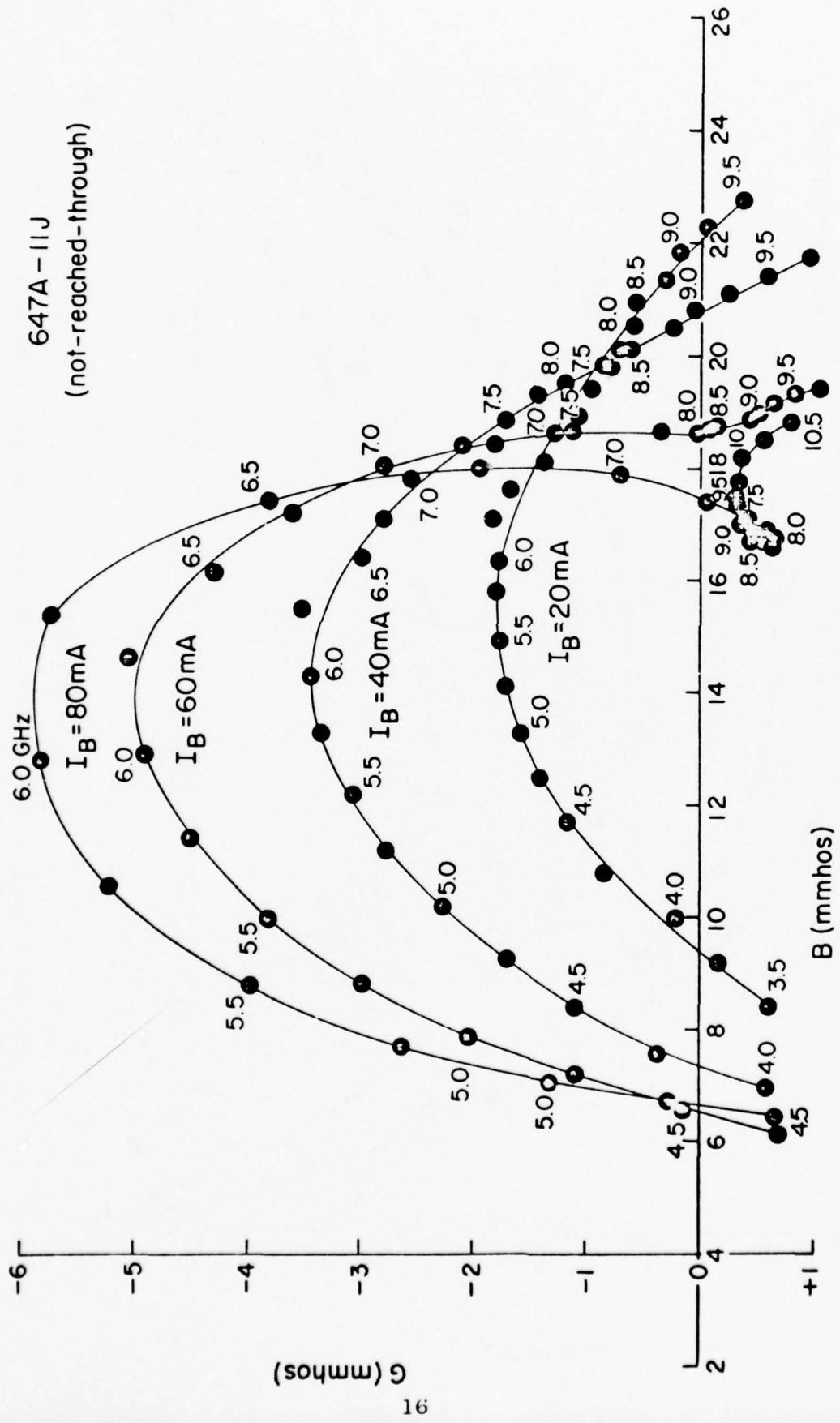Computed from ANA Measurements.

15

Figure 8. Microwave Small-Signal Admittance of Not-Reached-Through GaAs Read Diode 647A-11J Computed from ANA Measurements.

diode's G-B characteristic is the apparent "resonance" at 8.5 GHz. The electronic susceptance of the diode is apparently large enough to affect a decrease in the total susceptance of diode at this frequency. The second peak in negative conductance is associated with a 3π transit angle.

These results clearly show the differences between reach-through and not-reach-through diode types. The simple theory is not capable of describing the not-reach-through results. Therefore, in an attempt to separate the effects of reach-through from those of not-reach-through, modelling of the reach-through G-B characteristics has been pursued.

In order to obtain the diode chip conductance and susceptance, it is necessary to transform the ANA data through a mount and package equivalent circuit. The lumped equivalent circuit used to make this transformation has been modified to include lossy elements, as shown in Figure 9. Typical element values obtained by modelling of an A-921 package shorted by a gold ribbon are given below:

$$CF = 0.07 \text{ pF}$$
$$RC = 0.49 \text{ ohm}$$
$$LC = 0.48 \text{ nH}$$
$$RP = 997. \text{ ohm}$$
$$CP = 0.29 \text{ pF}$$
$$RS = 0.09 \text{ ohm}$$
$$LS = 0.25 \text{ nH}$$

Figure 10 presents the results of numerically fitting the "Quasi-static" impedance equation to the transformed G-B data for 637A-24Q at 80 mA. The diode parameters which are obtained from the theory are listed in Table I. As can be seen, the theoretical fits are very close to the experimental data.

It is useful to compare the experimental and theoretical variations in the electronic quality factor, Q_p, for this diode
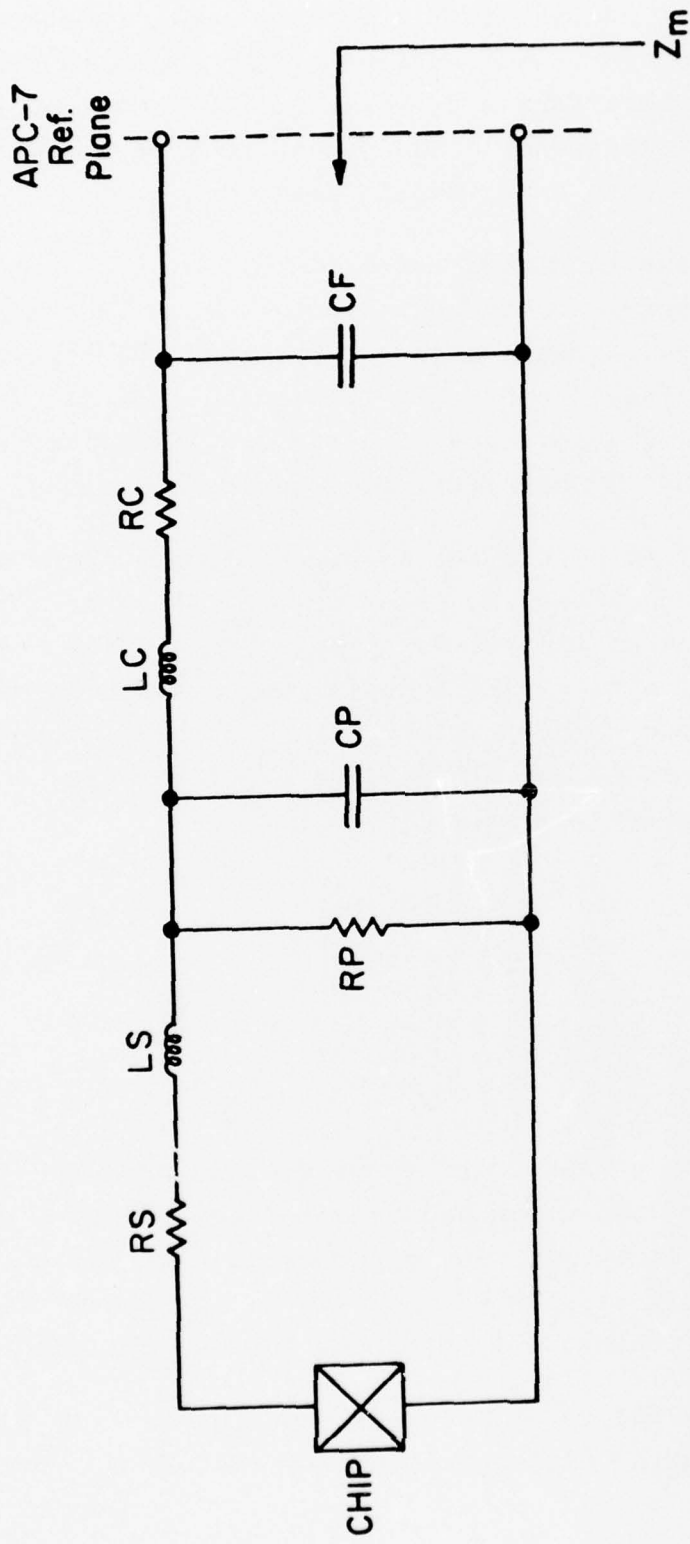
Figure 9. Lumped Equivalent Circuit of Package and Mount Including Lossy Elements.

18
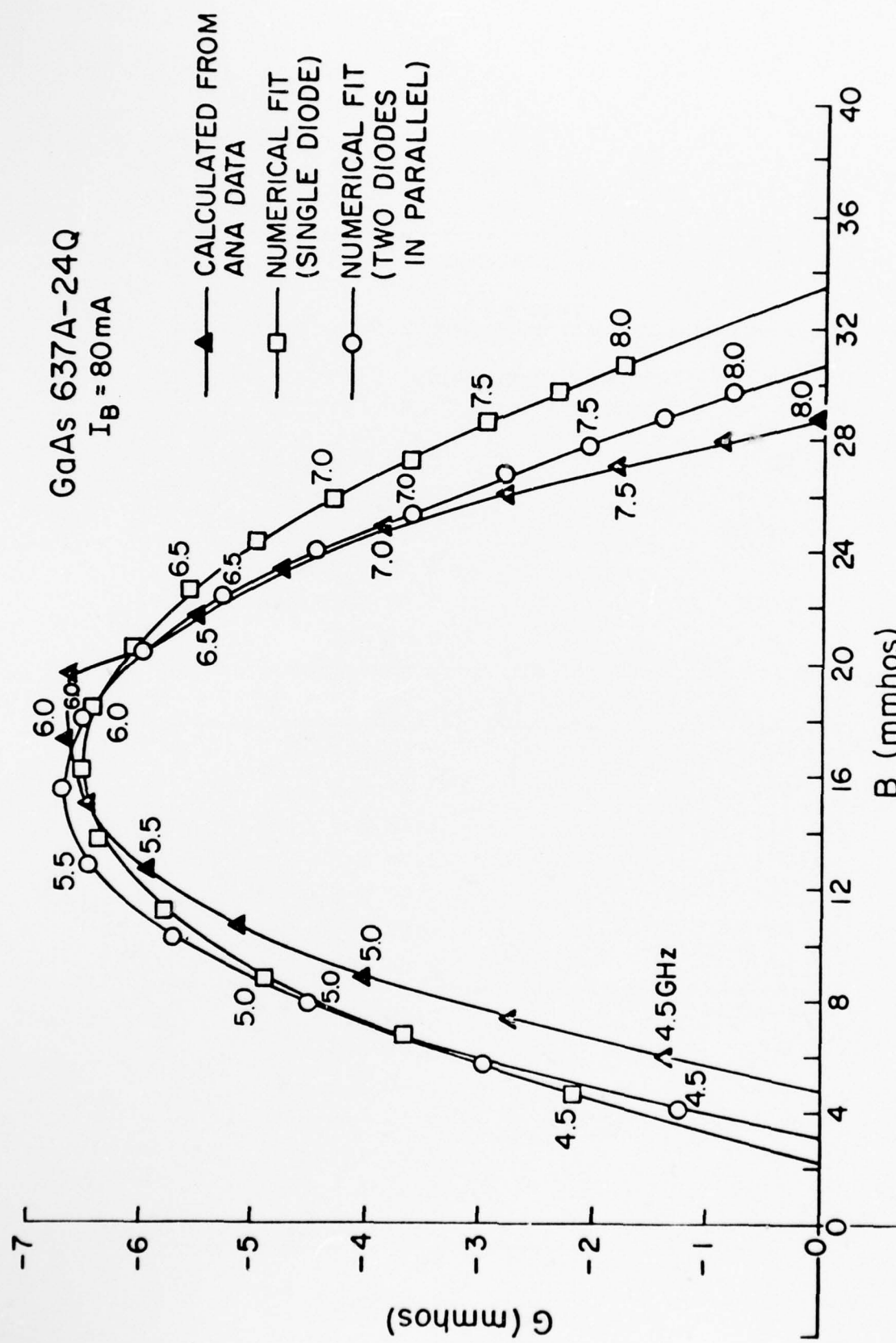
Figure 10. Numerical Fits to G-B Characteristic of GaAs 637A-24Q at $I_B = 80$ mA.

TABLE I

GaAs 637A-24Q
I=80 mA

SINGLE DIODE MODEL

FWA	0.111
WD	5.06 E-4 cm
A	2.75 E-4 cm^2
VS	4.97 E+6 cm/sec
FA	3.99 E+9 Hz
MTAU	3.00 E-10 sec
RS	0.50 ohm

TWO DIODES IN PARALLEL

FWA1	0.253
WD1	5.07 E-4 cm
A1	1.15 E-4 cm^2
VS1	3.75 E+6 cm/sec
FA1	4.50 E+9 Hz
MTAU1	1.92 E-10 sec
RS1	1.30 ohm
FWA2	0.006
WD2	5.00 E-4 cm
A2	1.50 E-4 cm^2
VS2	5.26 E+6 cm/sec
FA2	3.96 E+9 Hz
MTAU2	3.55 E-10 sec
RS2	1.31 ohm

as a function of frequency in order to assess possible errors in the transformed G-B data and to assess the goodness of the theoretical fit. Figure 11 represents the Q_p variation deduced from ANA data. Also plotted are several experimental values obtained by the power perturbation technique.[10] These experimental values predict a zero-crossing of Q_p at 6.65 GHz for I_B = 40 mA, which is in agreement with the ANA data. The question remains, "What does the theory predict on the basis of the numerical fit?" The theoretical variation of Q_p with frequency is presented in Figure 12, for I_B = 80 mA. The theoretical variation using the "ideal-Read" approximation $((x_1/W)$ terms neglected) also predicts a zero-crossing of Q_p. Thus, the theoretical fit appears to be a good approximation to reality, despite a slight skewing of the fit at the higher frequencies.

Further characterization of the reached-through diode has been accomplished using low-frequency noise measurements. Figures 13(a) and (b) present the experimental 30 MHz noise data for this diode, as well as a theoretical fit. The multiplication at the noise peak is much larger for this diode than for the not-reached-through diode 676-10#2. One possible explanation for this is the wider avalanche zone. The electric field is likely to be higher due to the reach-through condition. Thus, there is likely to be more multiplication. The intrinsic response time which is obtained from the 30 MHz noise fit is about 8 picosecs. This is also consistent with a wider avalanche zone.

Recall that in the previous report it was possible to establish a correlation between the numerical fit to microwave small-signal admittance and the 30 MHz noise data. This correlation has also been established for this diode. It is necessary, however, to use a better model for the diode operating at high dc dissipation. This model is consistent
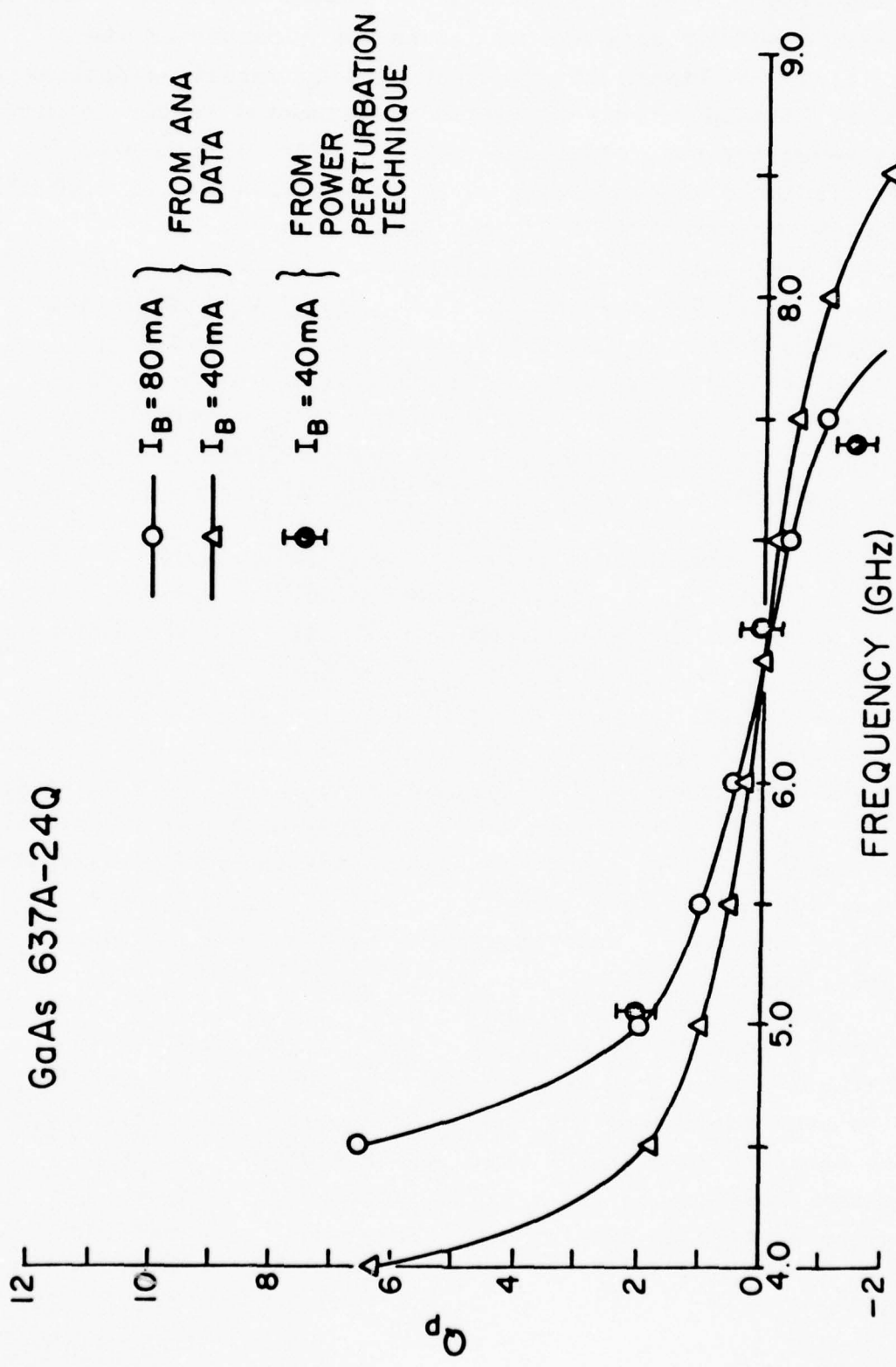
Figure 11. Electronic Quality Factor, Q_p, as a Function of Frequency for GaAs 637A-24Q.

GaAs 637A-24Q

FREQUENCY (GHz)

$I_B = 80\,mA$ $\Big\}$
$I_B = 40\,mA$ $\Big\}$ FROM ANA DATA

$I_B = 40\,mA$ $\Big\}$ FROM POWER PERTURBATION TECHNIQUE

Q_p

22
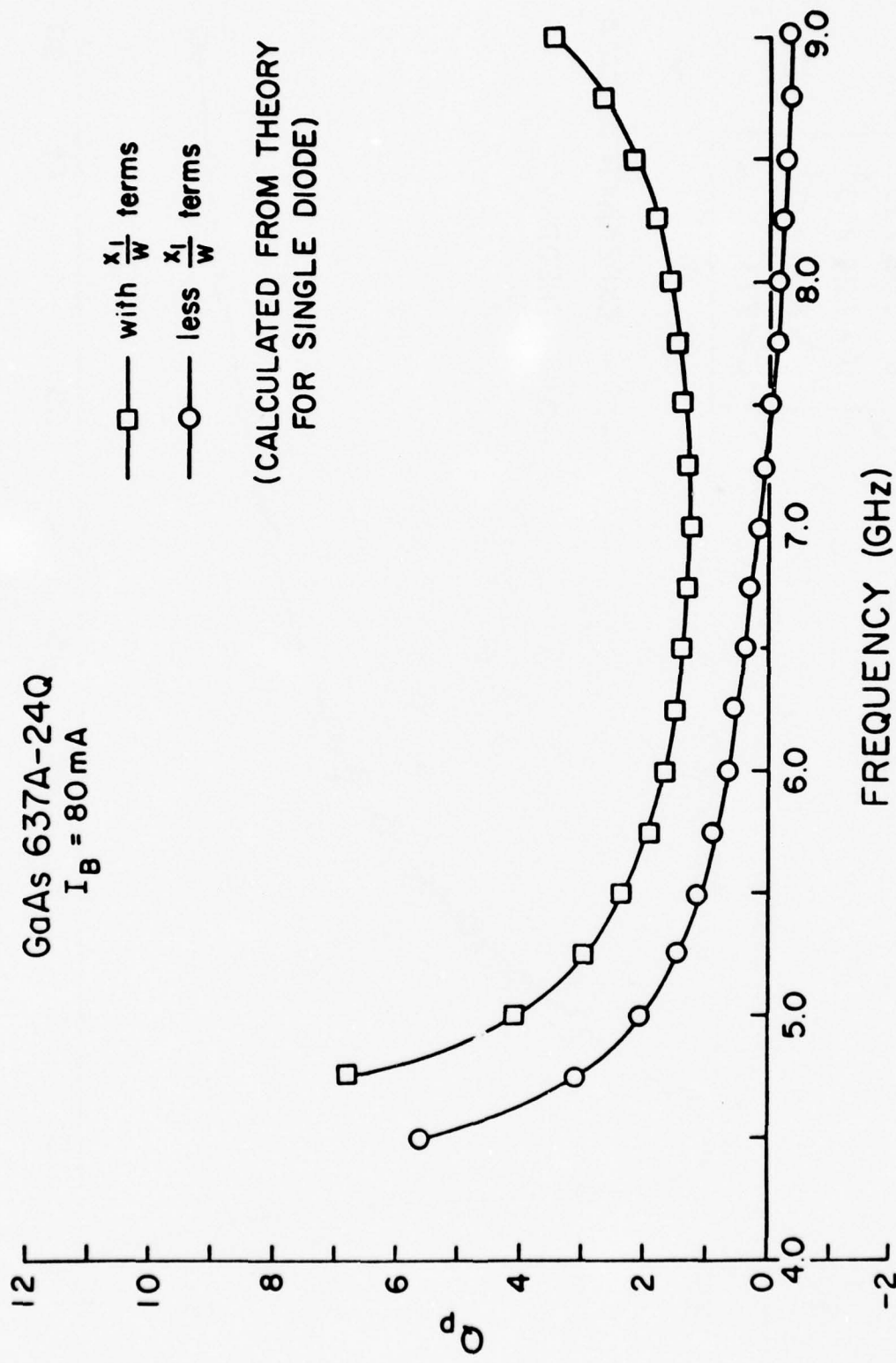
Figure 12. Theoretical Variation of Q_p with Frequency from Numerical Fit.

GaAs 637A–24Q

$M_{pk} = 636$

$I_s = 7.86 \times 10^{-6} A$

$a' = 3.62 \times 10^{-3}$
$b' = 1.24 \times 10^{5}$
$c' = 3.87 \times 10^{4}$
$d' = 7.13$

+ — EXPERIMENTAL DATA

⊙ — THEORY

$\langle i^2 \rangle$ (A²)

I (mA)

Figure 13(a)   30 MHz Short-Circuit Avalanche Noise Current as a Function of Bias
Current for GaAs 637A–24Q.

24
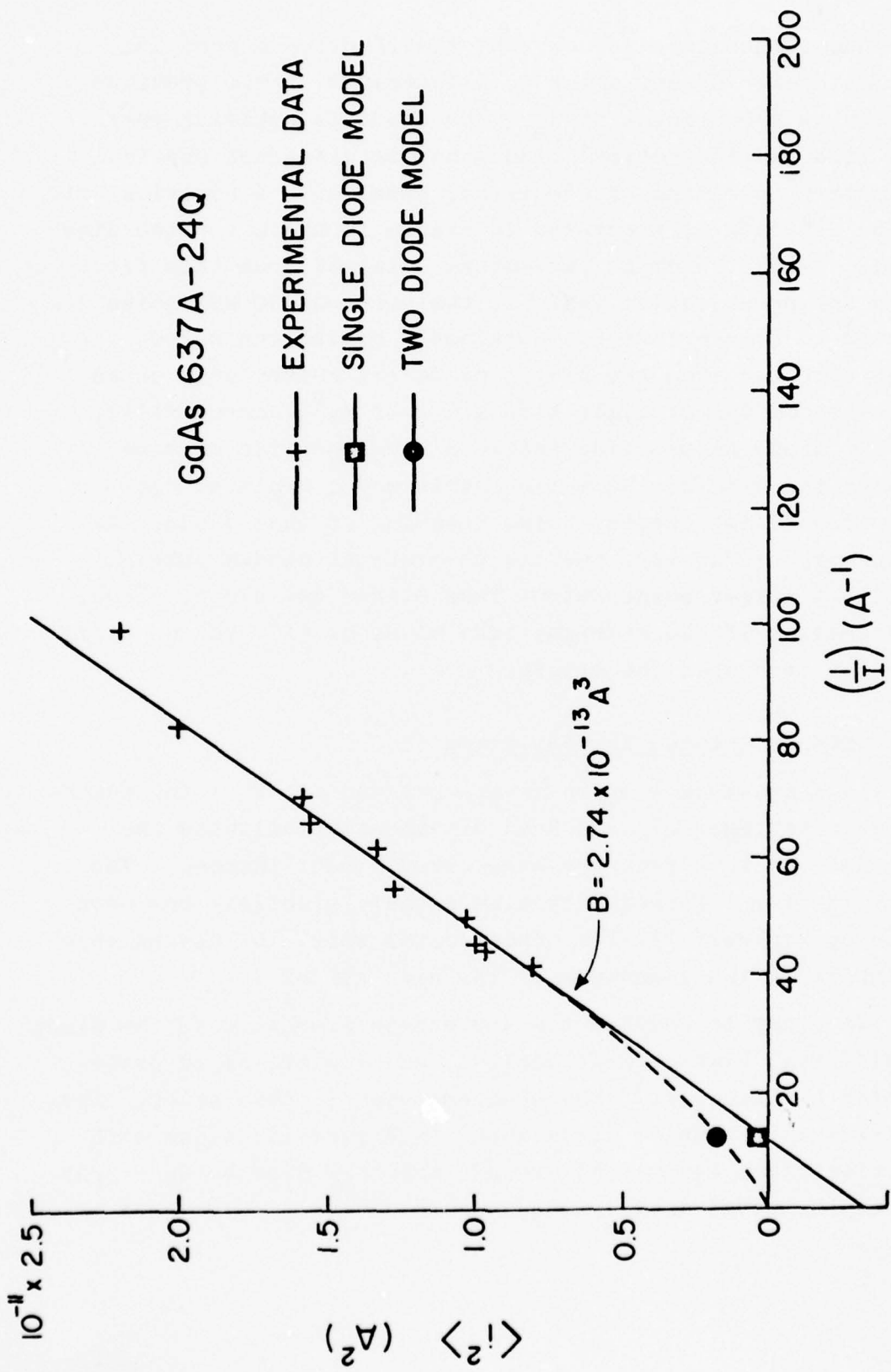
Figure 13(b) 30 MHz Short-Circuit Avalanche Noise Current as a Function of (1/I) for GaAs 637A-24Q.

25

with the temperature and current distribution across the
solid-circular diode, which is illustrated in the previous
section on the origins of I_s. The diode is behaving very
much like two theoretical diodes having different physical
parameters operating in electrical parallel. A numerical fit
to the G-B data is presented in Figure 10 using the two diode
model. Using the diode parameters obtained from this fit
which are presented in Table I, the value of 30 MHz noise
plotted in Figure 13(b) is obtained. Unlike the noise
value computed from the single diode fit which falls on an
extension of the straight line slope of $<i^2>$ versus (1/I),
the two diode noise value falls on a curved line passing
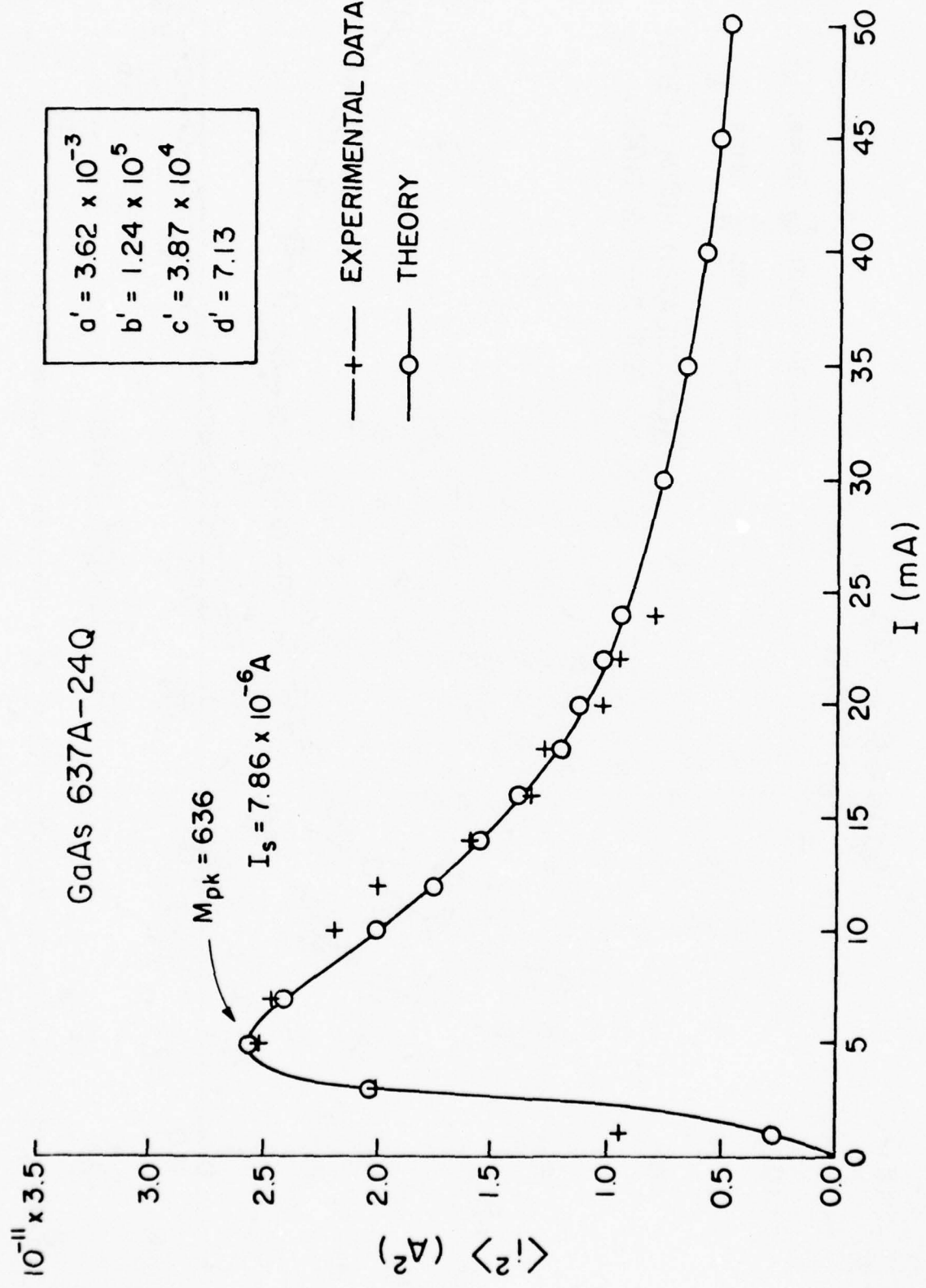through the origin. We believe this model explains the
"anomalous" high current noise behavior of this diode. At
lower current density, the two theoretical diodes combine
to give a larger noise output than either one alone. Thus,
an extension of the straight line slope of $<i^2>$ versus (1/I)
will not intersect the origin.

Bias Circuit Related Instabilities

In a previous section it was pointed out that the space-
charge resistance of GaAs Read diodes will influence the
threshold of low-frequency bias circuit oscillations. The
condition for low-frequency bias circuit stability has been
given by Brackett.[11] The other factor which influences this
threshold is the impedance of the bias circuit.

In order to compare the impedances presented to the diode
by different bias-circuit designs, an electric-field probe
similar to Eisenhart[12] has been employed in this study. The
experimental setup is illustrated in Figure 14, along with
the electrical equivalent circuit which is used to interpret
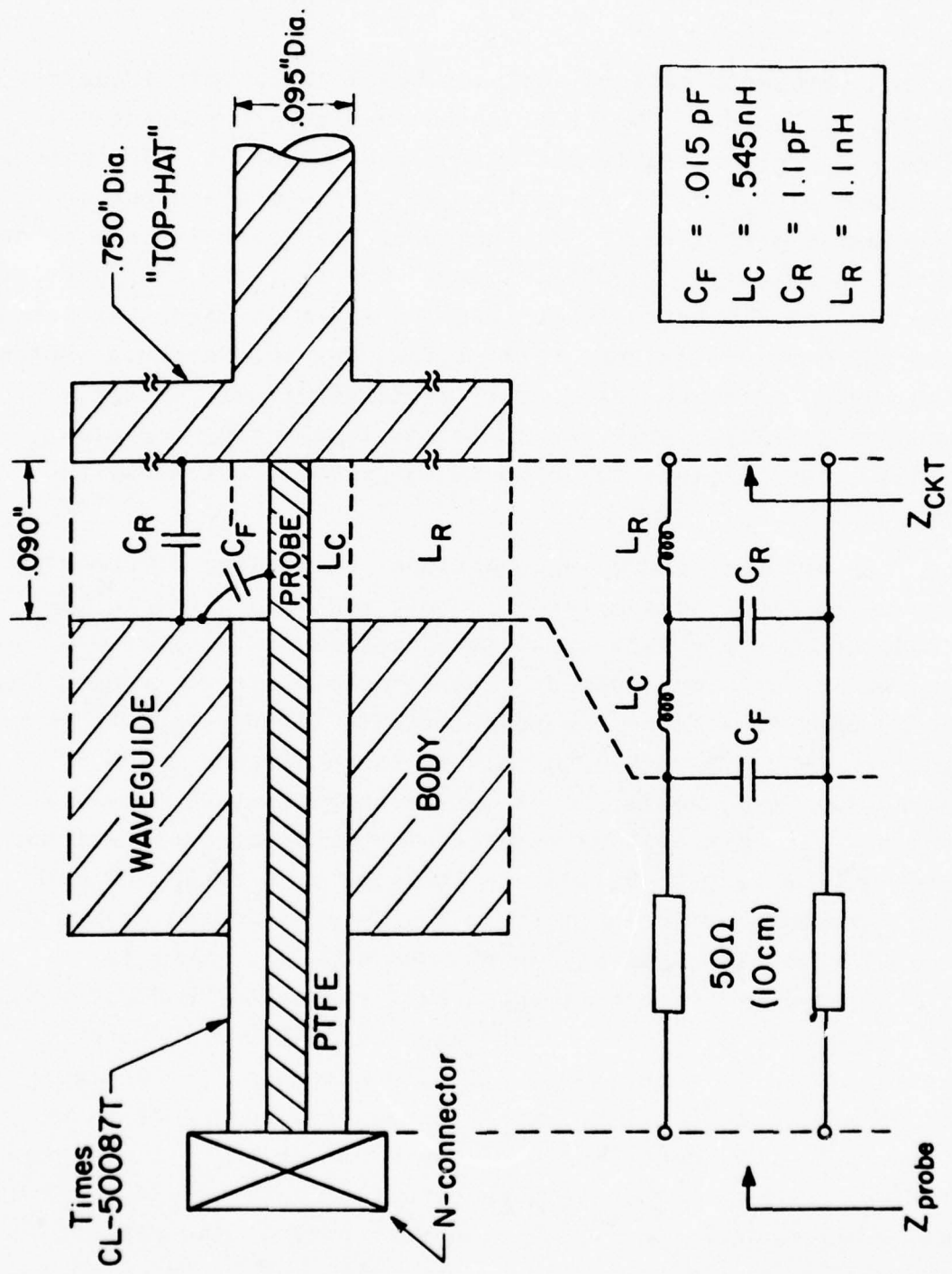the experimental data. Impedance measurements have been taken

26

Figure 14. Schematic Representation of Impedance Probe Measurement Geometry and Electrical Equivalent Circuit.

27

on the automatic network analyzer below the cutoff frequency of the waveguide. The interpreted results are presented in Figure 15 for two different bias circuit designs. The Cornell designed bias circuit is similar to Brackett's and has been previously described.[13] The Raytheon bias circuit is a folded-choke design. The results clearly show that the real part of the circuit impedance is at least an order of magnitude larger for the Cornell designed circuit than for the Raytheon (below 1.5 GHz). Although the Cornell designed circuit is not unconditionally stable, there is little tendency for bias circuit oscillations to occur in comparison to the Raytheon circuit.

In order to insure unconditional stability, it appears necessary to present a large, purely real impedance to the diode at low-frequencies. This contention is supported by our experience with measurement of avalanche noise at frequencies above 30 MHz. The measurement setup is illustrated in Figure 16. It is not possible to measure the avalanche noise of 637A-24Q, for example, above a bias current of 25 mA using the 0.2 ohm load without experiencing coherent oscillations. Even when this 0.2 ohm load is replaced by a 20 dB, 50 ohm pad, there is an enhancement in the noise measured at 220 MHz relative to the noise at 140 MHz and 420 MHz. This is illustrated by the experimental data presented in Figure 17. The impedance presented to the diode at 220 MHz has been measured and is found to be slightly reactive. Since the diode's reactance may be either capacitive or inductive at this frequency, depending upon the bias current, it is possible for the diode to resonate this circuit reactance and to produce an enhancement in noise. If the real part of the circuit impedance is also small, then this noise may build up to a coherent oscillation.
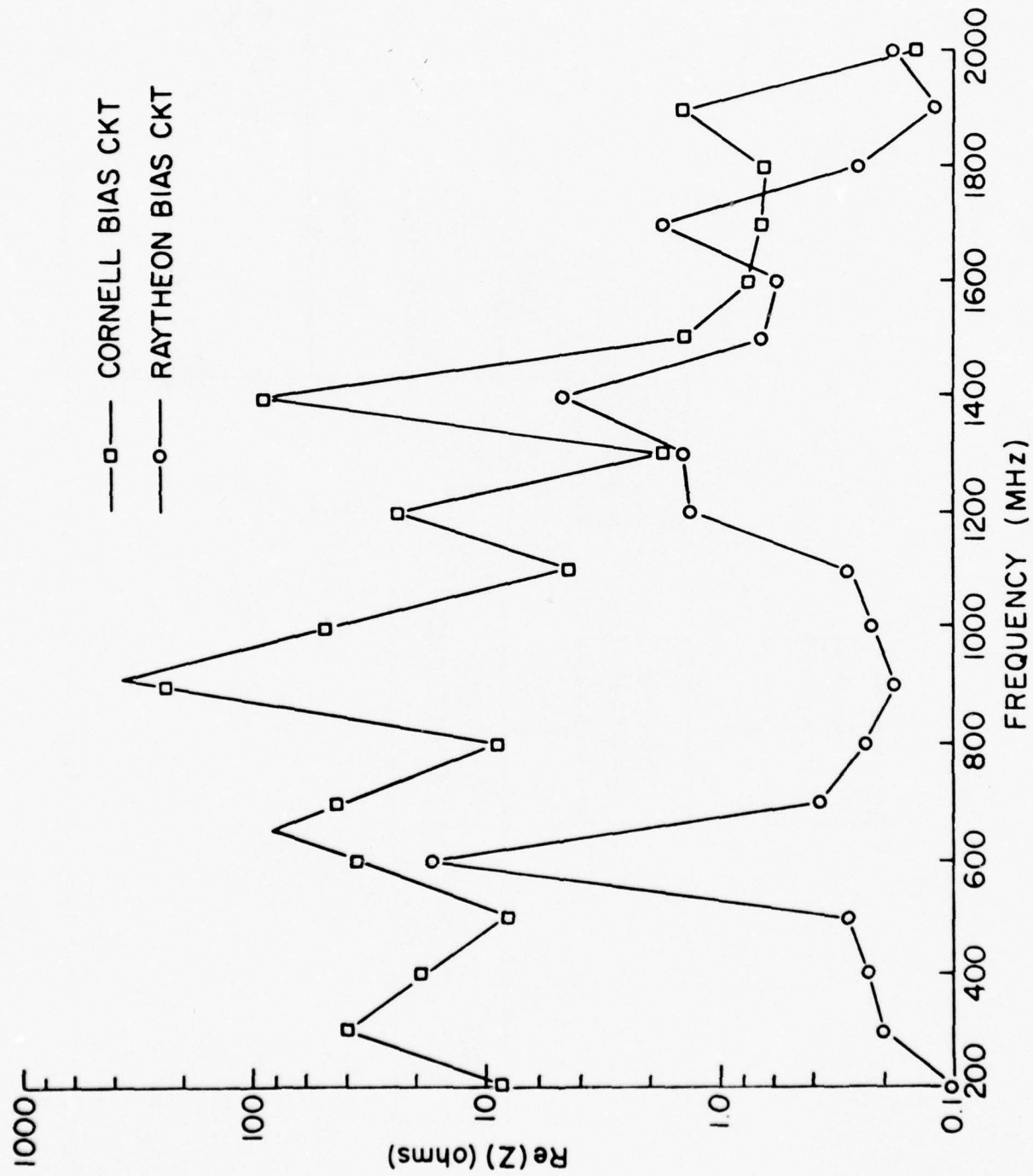
28

Figure 15. Low-Frequency Bias Circuit Impedance Computed from Impedance Probe Measurement.
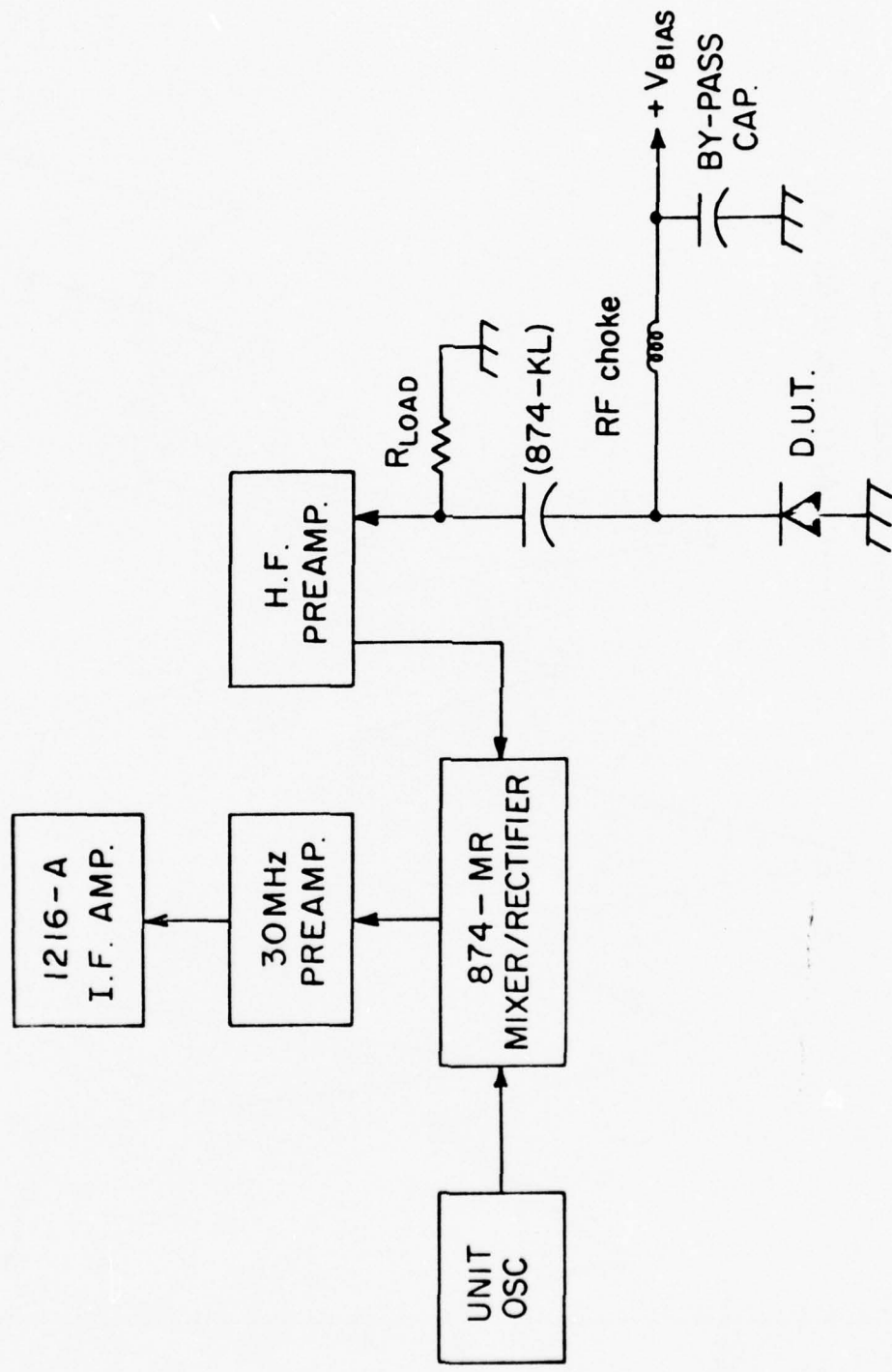
29

Figure 16. Heterodyne Receiver for Low-Frequency Noise Measurements Above 30 MHz.
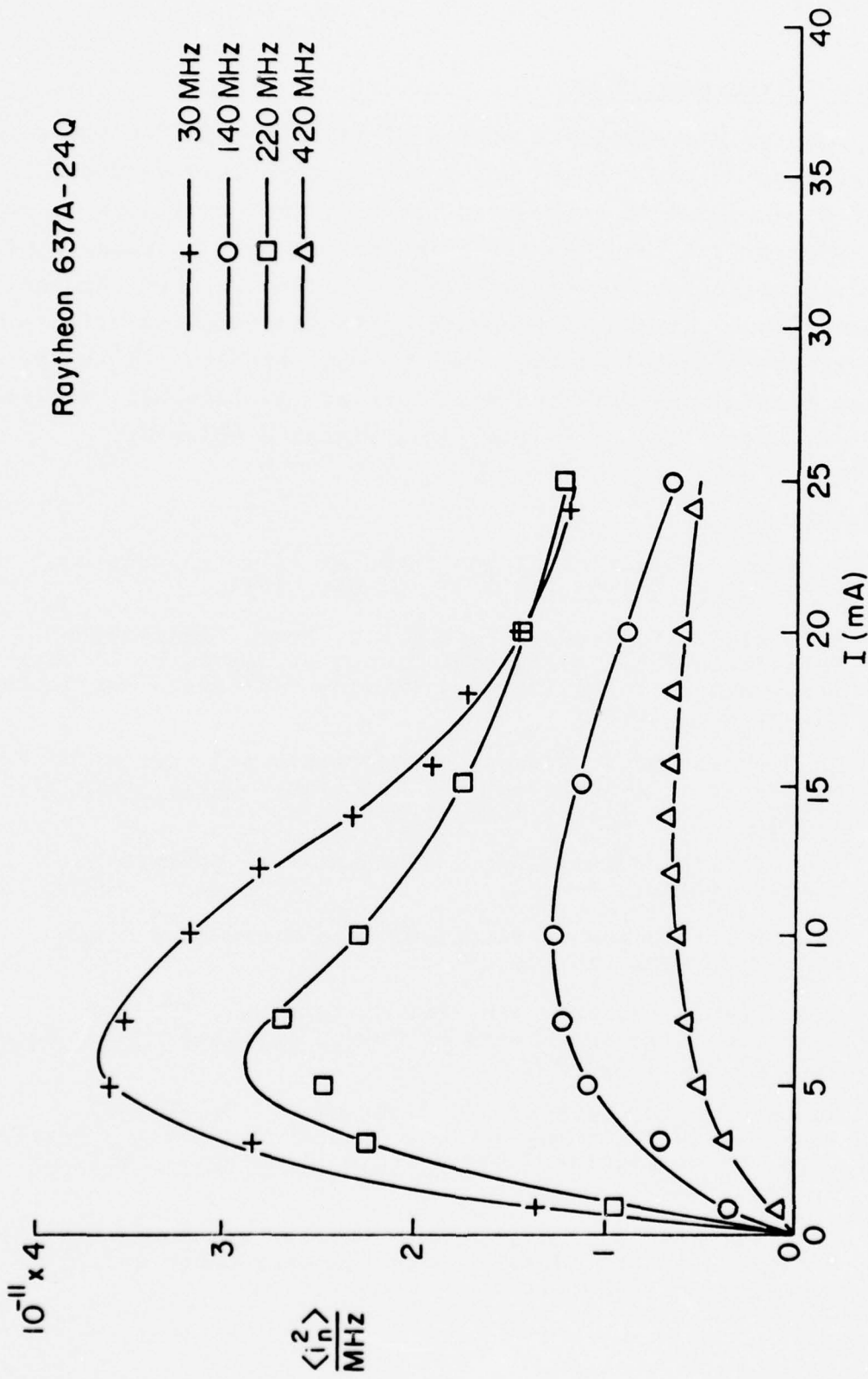
Figure 17. Short-Circuit Avalanche Noise Current as a Function of Frequency for GaAs 637A-24Q.

31

Plans for Further Study

During the remaining months of this program the comparison between reach-through and not-reach-through GaAs Read diodes will be extended to large-signal. From the preliminary results it appears that the "Quasi-static" theory will be capable of describing the experimental behavior of the reached-through diode. Thus, it should be possible to separate the effects of not-reach-through from the reach-through result. It is anticipated that a more detailed modelling of the internal rectification effect will improve the large-signal prediction.

References

1. V. Kumar, "Reaction of Sputtered Pt Films on GaAs," J. Phys. Chem. Solids, Vol. 36, p. 535, 1975.

2. H.B. Kim, G.G. Sweeney, and T.M.S. Heng, "Analysis of Metal/GaAs Schottky Barrier Diodes by Secondary Ion Mass Spectrometry," Institute of Physics Conference Serial No. 24, p. 307, 1975.

3. G. Gibbons and T. Misawa, "Temperature and Current Distribution in an Avalanching P-N Junction," Solid State Electronics, Vol. 11, p. 1007, 1968.

4. G.J. Scilla, Cornell Dept. of Chemistry, private communication.

5. G.H. Morrison and G. Slodzian, "Ion Microscopy," Anal. Chem. 47, 932A (1975).

6. J.H. Fermor, S. Furuseth, and A. Kjekshus, "On the Semiconducting Properties of $PtAs_2$," J. Less, Common Metals, Vol. 11, p. 376, 1966.

7. A. Laugier, M. Gavand, and G. Mesnard, "Propriétés Electriques D'Hétérojonctions Ge-GaAs Preparées A Partir D'Une Phase Liquide," Solid State Electronics, Vol. 13, p. 741, 1970.

8. R.N. Wallace, Raytheon Research Division, "Notes for the Operation of the IMPATT Diodes and Breadboard Circuit," Prepared for RADC, 1975.

9. J.C. Irvin and R.M. Ryder, "High Efficiency IMPATT Diodes," Applied Solid State Science, Vol. 5, p. 1, Academic Press, N.Y., 1975.

10. C.A. Lee and G.C. Dalman, "Amplifier Properties," Second Semi-Annual Report, Rome Air Development Center, Section A.1, p. 1, October 1974.

11. C.A. Brackett, "The Elimination of Tuning-Induced Burnout and Bias-Circuit Oscillations in IMPATT Oscillators," B.S.T.J., Vol. 52, p. 271, 1973.

12. R.L. Eisenhart, "Impedance Characterization of a Waveguide Microwave Circuit," Ph.D. Thesis, The University of Michigan, 1970.

13. A. Gupta, G.C. Dalman and C.A. Lee, "Interaction of Distributed IMPATT Oscillators," Third Semi-Annual Report to RADC, Section A.10, p. 132, April 1975.

Small and Large-Signal Effects on IMPATT Diodes

R. Souza, G. C. Dalman,*C. A. Lee*

This research has been completed and a final report has
been prepared. The following is an Abstract:

For the proper use and design of systems using IMPATT
diodes, a detailed knowledge of the diode admittance (or
impedance) variation with bias, frequency and RF signal level
is required. In this study, the effect of these parameters was
measured for silicon single-drift IMPATT and Read-type structures
operating at X-band, but the approach used applies equally well
to gallium arsenide diodes operating at different frequency
bands.

Initially, the theoretical small-signal behavior of IMPATT
and Read structures was analyzed and universal-type curves are
presented for the chip admittance. These curves are very
useful to estimate the avalanche resonant frequency at the
operating condition without resorting to special low microwave
frequency measurements. On the experimental side, a coaxial
reflection amplifier with a singly-tuned circuit was used as a
starting point. The circuit admittance transformation factor
was measured using a diode perturbation technique and the small
and large-signal diode admittances were determined from the
amplifier characteristics, measured up to drive levels well
into saturation. The large-signal amplitude and phase
distortions due to the non-linear interaction between the diode
and the amplifier circuit were also observed. Computer
programs were developed to simulate the amplitude and phase
performance of single-tuned reflection amplifiers, using
simple analytical expressions for the diode admittance. Good

*Project Supervisor

agreement was obtained between this simple theoretical model and the measured characteristics of single-tuned circuits. The theoretical results for a GaAs Read structure indicate that this diode can be expected to be used in the replacement of TWT amplifiers in many communication systems.

MEASUREMENT OF READ AND IMPATT DIODE AMPLIFIER PARAMETERS

J. W. McClymonds, G. C. Dalman,* C. A. Lee*

Introduction

This report is a summary of further developments made on
a method for measuring the small signal admittances of Read and
IMPATT diodes mounted in a 50 ohm circuit. Included in the
report are a discussion of improvements made in the measurement
system over the past six months, an analysis of the accuracy of
the system, and a conductance versus susceptance plot of one
device. This measurement system has been described in detail
in a previous report,[1] so a brief review of the measurement
system will be presented now.

Two basic items of equipment are used in this measurement
system--a Hewlett Packard network analyzer and a PDP-11/40
minicomputer that can be interfaced to the network analyzer.
A technique for calibrating this equipment has been developed
especially for Read and IMPATT diodes. To calibrate the system,
three calibration standards are measured by the network analyzer
over a frequency band and this data is recorded by the computer.
From this data, the coefficients of an error model for the
network analyzer are computed across the frequency band. The
system is now calibrated and data of the mounted device can be
measured and corrected for network analyzer error. The
calibration technique used in this measurement system has an
advantage over that of a commercially available automatic network
analyzer. In this system the three calibration standards can
be chosen from a large set of calibration standards to insure

---

*Project Supervisor

that the reflection coefficients of the three chosen calibration
standards are close to the reflection coefficient of the mounted
diode over the frequency band being measured. Thus, once the
system is calibrated, when the data for the mounted diode is
measured the reflection coefficient of the mounted diode falls
in a range where the network analyzer errors have been accurately
modeled, and the accuracy of the measurement system is very
good.

Recent Improvements in the Measurement System

Over the past six months, improving the accuracy of the
measurement system has received the greatest emphasis. As
the system has been used, some peculiarities of the network
analyzer have been noted which affect the accuracy of the
system. As would be expected, the factor which is most essential
to system accuracy is repeatability. The error model can fit
the errors of the network analyzer only to the extent that
the network analyzer measurements of the calibration standards
and the mounted diode are repeatable.

A very important factor in the repeatability of network
analyzer measurements is the setting of the "sweep stability"
control of the network analyzer. If the sweep stability
control is set to a position which is too sensitive, the
network analyzer output will exhibit discontinuities as the
frequency sweeps across the band, or the network analyzer will
not yield the same output from one sweep to the next. This
is presumably due to the switching of phase lock from one
harmonic to another of the local oscillator in the network
analyzer harmonic converter. However, no measurements have been
made inside the network analyzer, so this is only a hypothesis.
If the sweep stability control is set to a position which is
too insensitive, the network analyzer may fall out of phase

37

lock altogether. An optimum setting of the sweep stability control has always been found that will avoid both phase locking problems, but only over moderate ranges of frequency. The optimum setting depends on the frequency, so it is best to operate only over a 1 GHz frequency band at a time.

A second source of unrepeatability in the network analyzer is drift. This drift is assumed to be due to temperature changes in the network analyzer, because the problem is significantly smaller after a few hours of operation. Also, it was found that measurements made using the S_{11} function on the S-parameter test set drift the same amount as measurements made using the S_{22} function. This fact suggests a possible method for compensating for drift.

If port 2 is used for measuring the calibration standards and the mounted diode, and if a reference device, such as a coaxial short, is connected to port 1, then by switching between the S_{11} and S_{22} test functions, the amount of drift present in the S_{22} data can be determined. That is, if a measurement of the short on port 1 is measured once at some frequency, and then at a later time the measurement is repeated, then any difference between the two measurements should be due to drift. Since S_{11} and S_{22} measurements drift by equal amounts, the drift which has occurred in S_{22} measurements over this time interval is also known.

An attempt was made to incorporate automatic drift correction into the measurement system. To measure the reference short once for every S_{22} measurement would require far too many switching operations of the microwave switches in the S-parameter test set. Instead, the reference short was measured only at the beginning and end of each sweep through the frequency band. Between these two measurements of the reference short, the measurement system would measure the

calibration standard or mounted diode connected to port 2 in the normal manner. From the measurements of the reference short at the beginning and end of each sweep, drift between sweeps can be compensated, and drift during each sweep can be compensated approximately by linear interpolation.

It was found, however, that this method of drift compensation did not increase the over-all accuracy of the measurement system. It is presumed that in switching between the S_{11} and S_{22} test functions, the network analyzer requires a few seconds to settle to a final value. The time delay in the software could not be increased without requiring a major change in software, so this automatic approach to drift correction was abandoned.

As an alternative to automatic drift correction, the user can do two things to minimize the problem. First, "warming up" the network analyzer for a few hours before use greatly reduces the drift problem. Second, before each sweep the user can check for drift by manually switching to the S_{11} test function and checking to see if the reflection coefficient magnitude and phase of the reference short have drifted from some initial values. If the network analyzer has drifted, the user can adjust the vernier magnitude and phase controls to again obtain the initial readings for the reference short. The network analyzer is then switched back to the S_{22} test function and the measurement sweep is done in the usual way.

In addition to improving the measurement system to increase accuracy, the software of the system has been revised to make the system less cumbersome to use. The software has been divided into two independent computer programs. The first program controls the network analyzer, measures the three calibration standards, and measures the mounted diode five times. Having five measurement runs taken of the mounted diode is very advantageous, because the mounted diode can be measured for different values of

39

bias current without needing to recalibrate the system each time. The first program also corrects for the network analyzer error in the five measurement runs of the mounted diode and then stores this corrected data in a disk file. The second program reads the data stored in the disk file and is provided with diode package and mount equivalent circuit parameters by the user through the keyboard. This program corrects the mounted diode data for the effects of the diode package and mount and prints out the five sets of diode data "referred to the chip."

There are two advantages to the user by having the software divided into two programs. The user need only set up the network analyzer when the first program is used, and thus the network analyzer is not sitting idle while results are being printed. Another advantage is that the data which is stored in the disk file by the first program can be transferred to magnetic tape for permanent storage.

Analysis of the Accuracy of the Measurement System

The accuracy of the calibration standards is very good. The length of a calibration standard can be measured electrically with very good accuracy by noting the frequency at which the reflection coefficient phase of the calibration standard equals -180 degrees. This is done by using an X-Y recorder connected to the network analyzer (the computer is not necessary) to determine the frequency at which the reflection coefficient phase of the calibration standard intersects the reflection coefficient phase of a coaxial short connected in place of the calibration standard. A wave meter is used to measure the frequency of intersection precisely. Using this frequency, the equivalent electrical length of the calibration standard can be measured to about 0.2% accuracy. The calibration

40

standards are assumed to be lossless. Empirically, this is
a very good assumption if care is taken to clean the calibration
standards and snugly attach them to the network analyzer port.

The chief sources of error in the measurement system are
calibration standard accuracy, network analyzer drift, and network
analyzer noise. From experience, a tolerance of ±0.05 dB and
±1.0 degrees would be reasonable values for the accuracy of any
reflection coefficient measurements. Under worst case condi-
tions, the measurements of the three calibration standards may
all be in error in one direction while the measurements of the
mounted diode may be in error in the opposite direction. Thus,
the maximum error in the corrected data would be twice the error
in the uncorrected measurements, or ±0.1 dB and ±2.0 degrees.
The ± 0.1 dB figure translates into a 1% accuracy figure for
the magnitude of the reflection coefficient.

What these predictions for accuracy at the reference plane
of the network analyzer indicate in terms of chip conductance
and susceptance accuracy depend on the equivalent circuit for
the diode package and mount. For the diode data shown in
the next section, the chip conductance accuracy is about ±0.6 milli-
mhos and the chip susceptance accuracy is about ±3 millimhos.

An Example of Data Obtained with the Measurement System

Figure 1 is a plot of the chip conductance versus chip
susceptance of a complementary p-type IMPATT diode supplied by
Raytheon Research. Data was taken from 7 to 11 GHz with bias
currents of 150 and 200 milliamperes. Because this diode has
very little gain, due to its experimental nature, it is a good
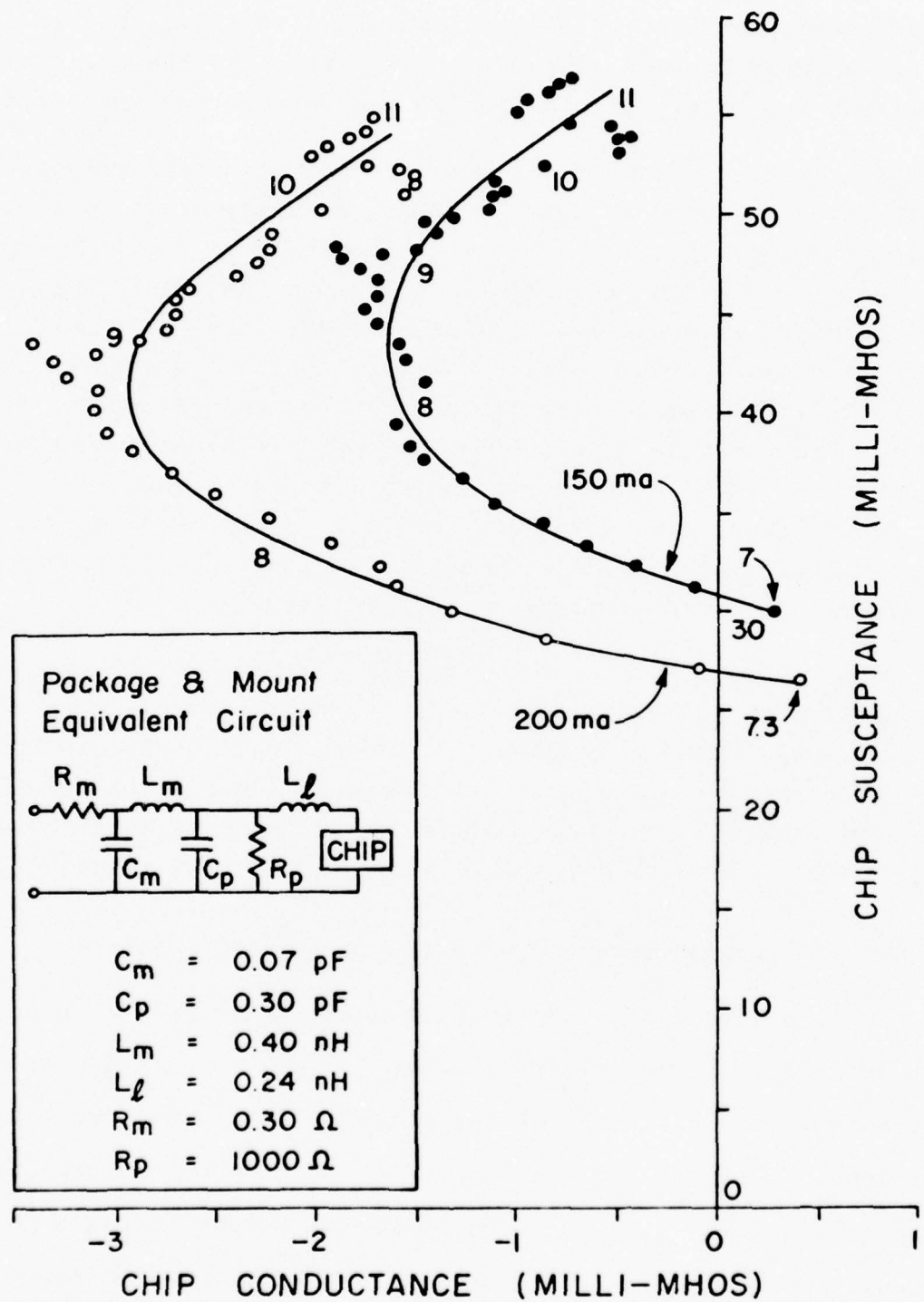choice for an example to demonstrate the advantages of this

Figure 1. Chip Conductance versus Chip Susceptance of a p-type IMPATT Diode.

method of measurement. Data taken of this device using a
commercial automatic network analyzer is unreliable because
the gain of the device is comparable to the inaccuracy of the
system.

Plans for Future Research

It would be very interesting to apply the techniques and
expertise gained in developing this small signal measurement
system to large signal measurements. A large signal measurement
system was set up temporarily to determine if the idea were
feasible. Discrete components were used to build a reflecto-
meter, and this reflectometer was connected to the harmonic
converter of the network analyzer instead of the S-parameter
test set. A diode in a one-slug slotted line cavity was used
as the device under test. Qualitatively, the system performed
very well and it seems to be a good approach toward simplifying
large signal measurements. Work should begin on this project
in June.

Reference

1. J. W. McClymonds, G. C. Dalman, C. A. Lee, "Measurement
    of IMPATT Diode Amplifier Parameters, Rome Air Development
    Center, Semi-Annual Report, October 1975.

Computer Simulation of TRAPATT Device-Circuit
Interactions
Z. Bogan, Jeffrey Frey*

This research has been completed and a final report has
been prepared. The following is an Abstract:

This work presents a computer simulation of device-circuit
interactions in coaxial TEM-mode Time-Delay-Triggered TRAPATT
circuits, as well as simulations of related problems such as
relaxation oscillations and a comparison of DC to RF con-
version efficiencies of complementary TRAPATT devices.

The computer simulation program combines a detailed
description of the device physics with a time domain analysis
of the coaxial circuit in which the device is embedded. The
device physics are described in terms of a hyperbolic partial
differential equation in the displacement vector, which is
solved by means of a modified method of characteristics. This
equation, along with its initial and boundary conditions,
contains all the information about the device dynamics. The
external waveforms on the device terminals are calculated
iteratively from both circuit constraints and from the internal
dynamics of the diode.

A comparison of the conversion efficiencies of two
complementary TRAPATT structures was carried on under the
constraint of a square wave external current. This analysis
confirmed experimental reports that stated that in some
circumstances the N^+P structure is more efficient than its
complementary P^+N.

*Project Supervisor

44

Special emphasis was put on the analysis of the turn-on transient in a coaxial TRAPATT circuit. Ways of reducing the turn-on time in practical circuits are suggested here on the basis of this analysis.

High Power, High Efficiency CW TEO's

G. Herlihy, L. F. Eastman*

This report summarizes work done on the high power and efficiency TEO's from November 1975 to May 1976. Maximum power and efficiency remain at the 1.35 watt CW and 8.4% efficiency at 3.0 GHz that was reported during the last period.

In this period efforts have been made to determine the load on the diode that is presented by the stripline circuit, described later, and the MARC type circuit at both the fundamental frequency and the second harmonic.

Stripline Circuit

Very good results were obtained and reported during the last period. A maximum output power of 1.35 watts CW at 3.077 GHz with an efficiency of 8.4% was obtained with diode number 2237-271. Other diodes were also operated with output powers in excess of 1 watt CW and efficiencies above 7%. All but one result was obtained with the heatsink positive. The reasons that we believe that this polarity will result in better efficiency was reported last time and will be included in the final report.

The circuit consists of a 50 ohm stripline with the device placed on a pedestal near one end of a rectangular cavity and the output goes to a slotted line which comes off of the stripline near the side opposite that of the device. Bias is brought in through a wavetrap to help minimize bias circuit oscillations. These physical characteristics of the circuit can be seen in Figure 1.

The circuit with slotted line attached is shown in Figure 2. There are 5 slugs in the output circuit. In order, from the circuit there are nominally 20Ω slugs that
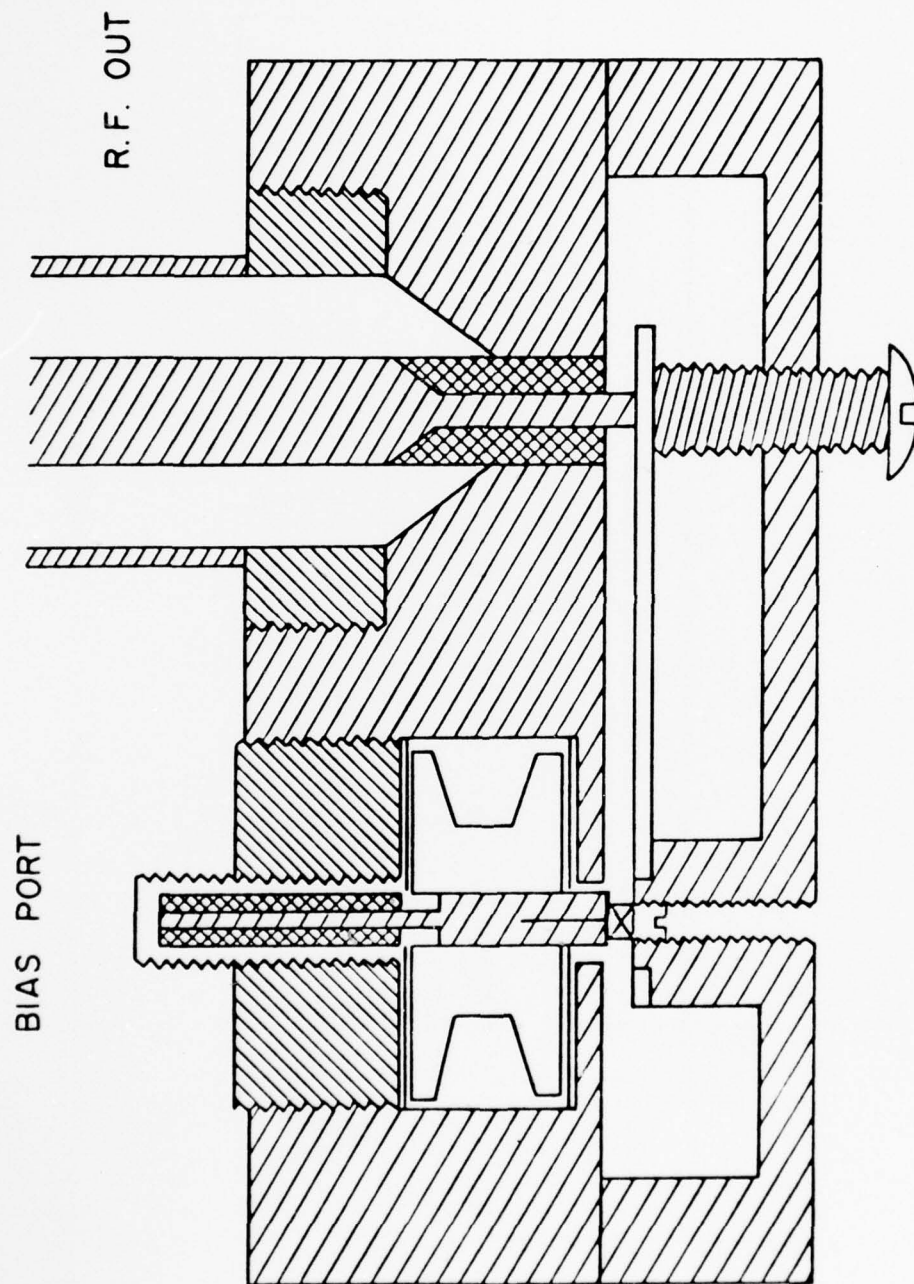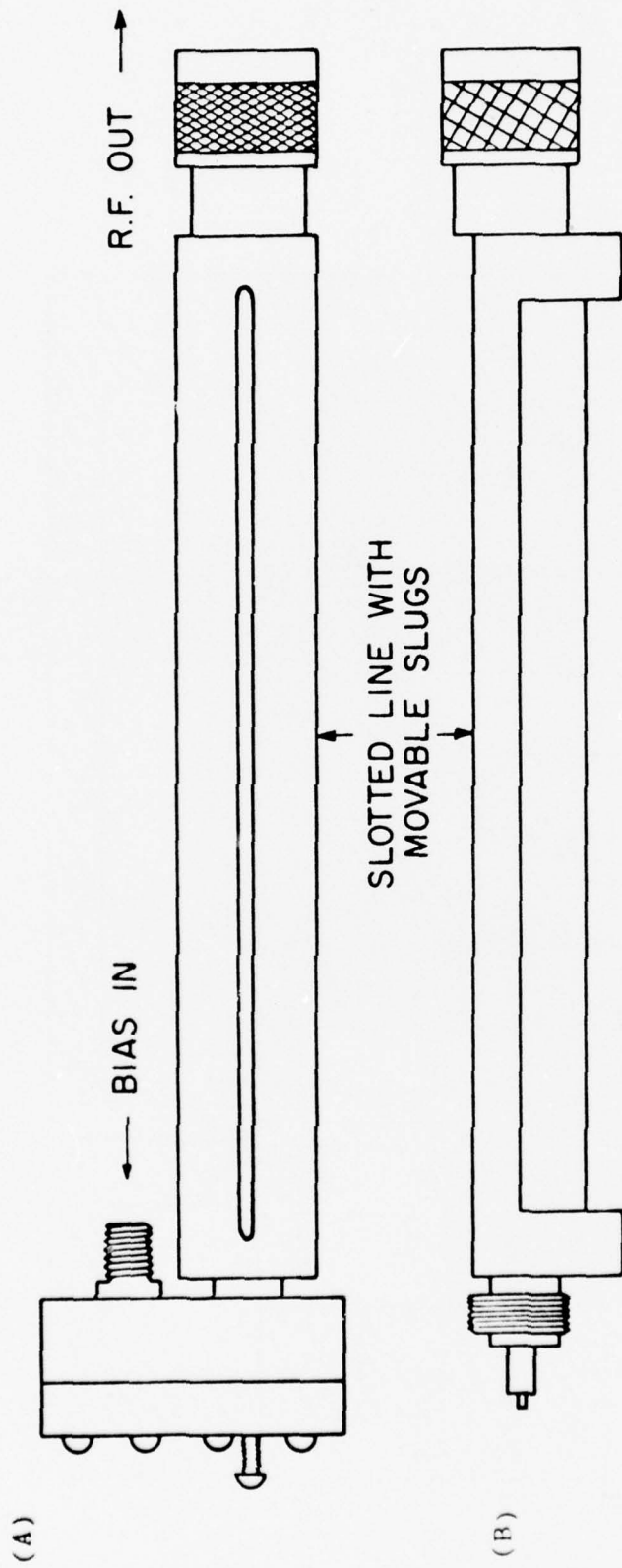
*Project Supervisor

R.F. OUT

BIAS PORT

Figure 1. Cut Away View of the Stripline Circuit with Oxide Diode in Place.

47

Figure 2. (A) Stripline Circuit with the Slotted Line Attached

(B) Side view of the Slotted Line.

48

are $1/8\lambda$, $1/8\lambda$, $1/4\lambda$, $1/4\lambda$, and then a nominally 32 ohm slug again of $1/8\lambda$. After the slotted line there are calibrated broadband attenuators, a wavemeter and finally a power meter.

Calculation of the Load on the Diode

To accurately calculate the load on the diode it is first necessary to accurately determine the lengths of the different sections involved as well as the characteristic impedance of those sections.

Two means were used to determine the characteristic impedance of the slugs. The first way was to measure the relevant diameters and lengths and calculate the Z_O where

$$Z_O = \frac{1}{2\pi} \sqrt{\frac{\mu_O}{\varepsilon \varepsilon_O}} \ell n \left(\frac{R_O}{R_i}\right)$$

where

$$\sqrt{\frac{\mu_O}{\varepsilon_O}} = 377\Omega$$

$R_O \equiv$ inside diameter of the outer conductor

$R_i \equiv$ diameter of the inner conductor

$\varepsilon \equiv$ the relative dielectric constant of the dielectric material (for teflon $\varepsilon = 2.1$).

The second method makes use of a property of the slug when a frequency, such that the length is $\lambda/4$ is applied.

When $\ell = \lambda/4$, $Z_{slug} = (1-e/1+e)^{1/2}$. Z_O of the line the test was made in (50Ω). These measurements were done using the network analyzer and are tabulated in Table 1.

The next step is to determine the characteristic impedances and lengths of the various sections of the two circuits that are internal.

49

TABLE 1

Nominal $Z_O (\Omega)$	Nominal f for $\ell=\lambda/4$(GHz)	Actual ℓ (cm)	$Z_O (\Omega)$ from Dimension	$Z_O (\Omega)$ Measured
20	4	1.277	20.88	22.30
20	8	.6426	20.88	22.29
32	8	.6947	34.69	37.7

When the characteristic impedances and lengths are all known, a computer program was developed which, when the slug position and characteristics were given, would give the impedance at the plane of the diode. It is also possible to calculate the input impedance that should be seen when known load is placed at the plane of the diode.

To test the results, two known loads, the first an empty package which represents a .32 pf capacitor at the diode plane, and the second, a short-circuited package, were inserted in place of the Gunn diode. The results of the test and the calculated results are presented in Table 2.

TABLE 2

Load	Load Impedance	Z_{in} Meas.	Zin Calc.
.32 pf	$-j164$	$.955/167.5^O$	$1.0/-51.4^O$
short	$0+j0$	$.942/-102^O$	$1.0/-173.4^O$

using the dimensional Z_O's

.32 pf	$0-j164$	$.955/167.5^O$	$1.0/-44.3$
short	$0+j0$	$.942/-102^O$	$1.0/-169.7$

using the measured Z_O's.

As can be seen, the calculated results are less than adequate. When the program was used to find the load at the diode plane the results were:

using the dimensional Z_O's

$$Z_L = 40.52 - j11.61$$

using the measured Z_O's

$$Z_L = 41.39 - j10.27$$

for the slugs placed in position for maximum output power and efficiency for diode #2237-271.

A New Probe for Measurement of the Impedance

As the test had shown that this method of calculation was questionable, an attempt at characterizing the circuit by changing the capacitance at the diode plane by means of a varactor diode, this method also developed problems.

It was then felt that the only way to accurately determine the load on the diode was to actually go in and measure it with a probe. There appears to be three good ways to insert a probe at the plane of the diode. The first way would be to insert it through the heatsink side of the diode. This type of probe would have to be very small in diameter and might also be hard to determine whether or not it was positioned correctly. Another problem with this type of probe is that it cannot be used on all cavities specifically it cannot be used on the MARC circuit as the RF port flange partially covers the hole to the outside.

The second and third types of probes would be inserted through the wavetrap of the circuit. The second type would consist of a simple wire probe into the cavity. The third type would involve placing a diode package on the probe which would then be screwed into place exactly like the real diode package.

We decided to try to make the probe with the package attached as it would also obviate the need to transform the impedance through the ceramic of the package so it would give a more realistic reading of the impedance seen by the actual device. This probe, as seen in Figure 3, was constructed by Paul Lumbard and after initial problems with keeping the package attached were solved, performed very well.

Figure 4 shows the probe in place in the stripline circuit. It is also possible to insert the probe in the MARC circuit and several other circuits as long as the probe can be force-fitted into the wavetrap.

In order to find the position of the diode plane in relation to the network analyzer, it is necessary to short circuit the package and then finding the position of the short circuit. This plane is very close to that of the actual diode.

Results from the Use of the Probe

1. Diode #2237-271 was able to achieve 1.08 watts with 7.2% efficiency at 3.5 GHz in the MARC cavity with four external slugs. Measurements of the impedance were made for both the fundamental and 2nd harmonic frequencies. The results were:

fundamental: $Z = 12.4 + j19.95 = .649/\underline{134}^O$ into 50Ω

or a resistance of 45Ω in parallel with an inductive reactance of 28.

Second Harmonic: $Z = 2.89 + j28.8\Omega \equiv .910/\underline{129}^O$ into 50Ω

or a resistance of 200 in parallel with an inductive reactance of 24 .

2. Diode #2237-271 was able to produce 1.35 watts at 8.4% efficiency at 3.077 GHz in the stripline circuit with 5 slugs in the output circuit. The result of the probe measurements were:
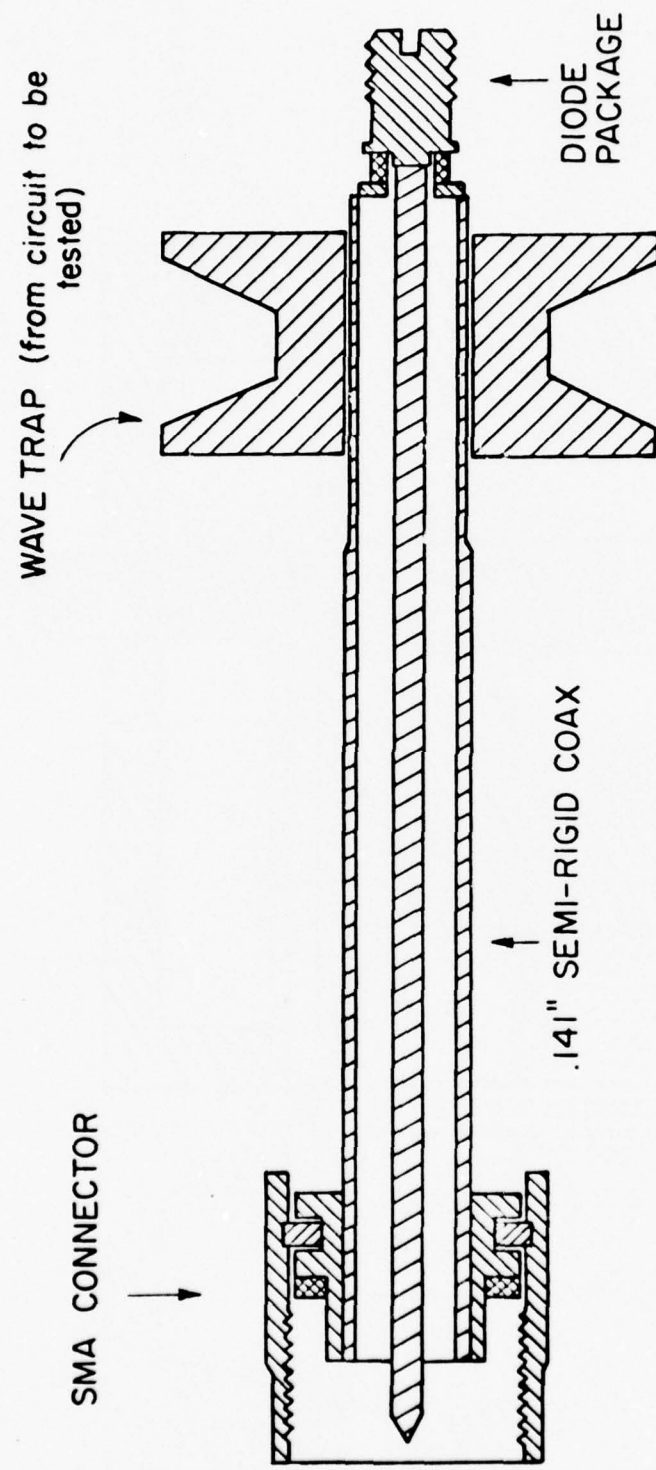
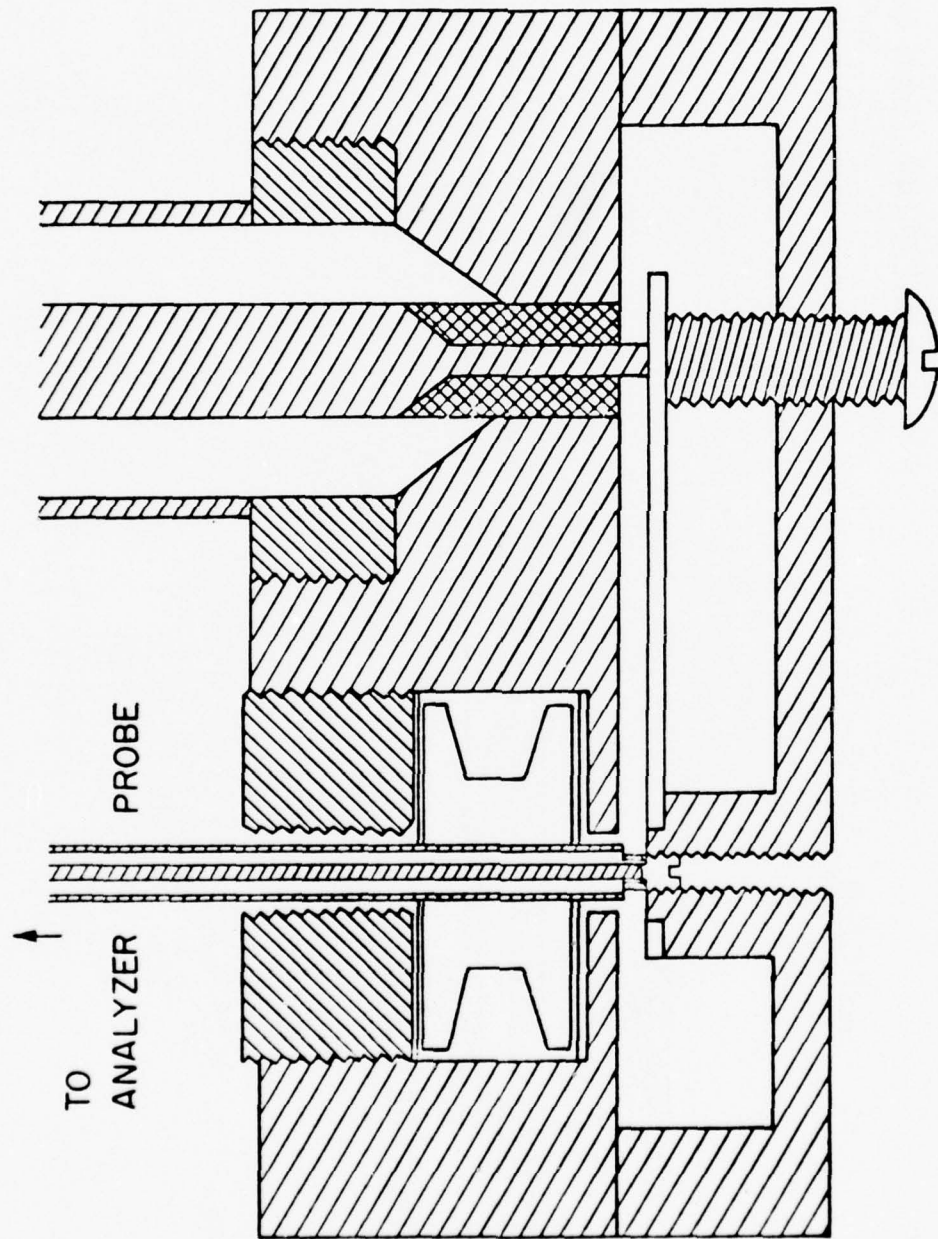Figure 3. Cutaway View of the Network Analyzer Probe Shown inserted in a Wavetrap.

PROBE

TO
ANALYZER

Figure 4. Network Analyzer Probe in the Stripline Circuit.

54

fundamental: $Z = 22.7 + j22.1\Omega \equiv .462\underline{/124}^O$ into 50Ω

or a resistance of 43.5Ω in parallel with an inductive reactance of 45Ω

Second Harmonic: $Z = 7.15 + j9.8\Omega \equiv .758\underline{/157.4}^O$ into 50Ω

or a resistance of 20Ω in parallel with an inductive reactance of 15Ω.

3.   The same diode produced 1.32 W at 8.3% efficiency at 3.029 GHz in the same circuit with the slugs in a different position.   The result of the probe measurements were:

fundamental: $Z = 22.4 + j22.25\Omega \equiv .468\underline{/124}^O$ into 50Ω.

or a resistance of 45.5Ω in prallel with an inductive reactance of 45.5Ω.

Second Harmonic: $Z = 8.65 + j5.45\Omega \equiv .708\underline{/167}^O$ into 50Ω

or a resistance of 12Ω in parallel with an inductive reactance of 19Ω.

4.   Diode #2237-259 was able to produce 1.03 watts at 7.86% efficiency at 3.820 GHz in the stripline circuit.   The results of the probe measurements were:

fundamental: $Z = 19.85 + j28.4\Omega \equiv .549\underline{/114.6}^O$ into 50Ω

or a resistance of 62.5Ω in parallel with an inductive reactance of 41.6Ω

Second Harmonic: $Z = 2.4 - j10.15\Omega \equiv .912\underline{/-157}^O$ into 50Ω

or a resistance of 45.4Ω in parallel with an inductive reactance of 10.7Ω.

These results are in Table 3.

It seems apparent that for a given diode the load for maximum efficiency can be determined in a circuit such as the stripline circuit and then load it correctly into another one

TABLE 3

Test #	Freq. (GHz)	Z(Ω)	Z (into 50Ω)	$R_p(\Omega)$	$X_p(\Omega)$
1	3.50	12.4 + j19.95	$.649/\underline{134}^{O}$	45	28
	7.00	2.89+ j28.8	$.910/\underline{129}^{O}$	200	24
2	3.077	22.7 + j22.1	$.462/\underline{124}^{O}$	43.5	45
	6.154	7.15+ j 9.8	$.758/\underline{157.4}^{O}$	20	15
3	3.029	22.4 + j22.25	$.468/\underline{124}^{O}$	45.5	45.5
	6.058	8.65+ j 5.45	$.708/\underline{167}^{O}$	12	19
4	3.820	19.85+ j28.4	$.549/\underline{114.6}^{O}$	62.5	41.6
	7.640	2.4 - j10.15	$.912/\underline{-157}^{O}$	45.4	-10.7

where R_p is the resistance in parallel
and X_p is the reactance in parallel.

however one cannot predict what the best power and efficiency
output might be as they depend on many other factors such as
the thermal resistance, polarity of the heatsink, the NL
product, etc.

AUTOMATED NETWORK ANALYZER

J. Sutherland, Jeffrey Frey*

Introduction

The physical sources of error inherent in the HP 8746B
S-parameter test set are described. The error model[1] employed
in the automated analyzer correction scheme is evaluated in
light of each of the sources of error, and justification of a
number of simplifying assumptions is made.

When the device under test is a transistor, the corrected
S-parameters, obtained using the aforementioned model, include
contributions from both the transistor and the test fixture.
We have earlier described a method[2] to decouple the transistor
S-parameters from the combined data. A simple fixture model was
assumed, and model parameters were determined by measurements
taken on the fixture alone. This model is further improved by
including the two APC7/OSM adaptors as part of the fixture,
eliminating one calibration run.

A remote entry TV typewriter has been added to the automated
system, allowing the user a greater degree of interaction with
the program software as measurements are being taken.

S-Parameter Test Set Error Model

In the June 1975 RADC Semi-Annual Report, a simple error
model was presented, to account for the rf mismatches inherent
in the S-parameter test set. A detailed discussion of the
sources of the mismatches present, and of how the model accounted
for each of these errors, are given here.

---

*Project Supervisor

A diagram[3] of the internal components of the HP 8746B is shown in Figures 1 and 2. In both the S_{11} and S_{21} modes, a portion of the rf input is coupled, through C_1, to the reference channel of the harmonic frequency converter, the remainder being presented to port 1 of the device under test (D.U.T.) through C_2. When S_{11} is measured, the reflected signal from port 1 of the D.U.T. passes through a 10 dB attenuator, switches S_4 and S_5 to the test channel of the frequency converter (the attenuator is present to reduce the apparent VSWR of the test channel from 2 to 1.07, causing port 2 to be more effectively matched). The other attenuators serve a similar purpose. Several sources of error are readily apparent. The coupling coefficients of both C_1 and C_2 are frequency dependent, varying the power presented to the reference channel compared to that actually reaching port 1 of the D.U.T. In addition the couplers have a finite directivity, causing leakage effects. Some mismatch will occur down the main rf line, referred to as source mismatch, due to small reflections from S_2 and S_3, C_1 and C_2, as well as from the APC-7 connector on port 1 of the test set. Port 2 of the test set is not terminated in a perfect match (for S_{11} and S_{21} modes), but by a load with a reflection coefficient of less than .13.[4] This return mismatch is further degraded when the D.U.T. is connected to port 2 of the test set through the flexible arm, whose VSWR can be as high as 1.25.[5]

When S_{21} is measured, the same port 1 errors are present. Now, however, the test channel signal is the transmitted power from port 2 of the D.U.T. As before, this network is not terminated in a perfect match, due to reflections from the flexible arm, S_5 and S_6, and the test channel input impedance. Thus, the ratio of the transmitted signal reaching the network analyzer to the input signal is not a true indication of S_{21}.

In the error model employed, directivity errors are assumed negligible, since specs indicate directivity to be greater than
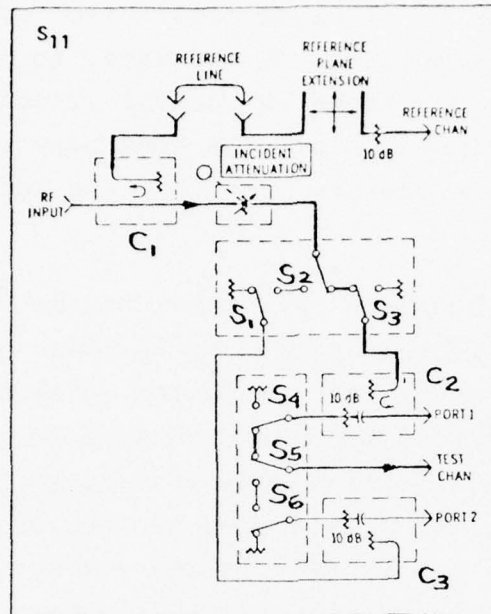
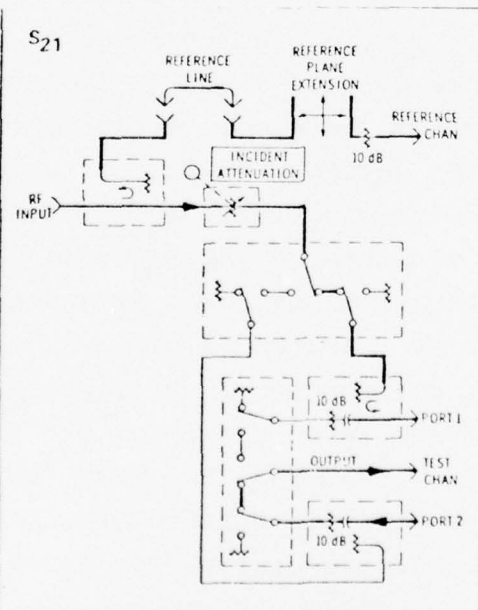Figure 1. Internal Components of HP 8746B S-parameter Test Set, S_{11} Mode.

Figure 2. HP 8746B in S_{21} Mode.

59

30 dB from 1-4 GHz, and greater than 26 dB from 4-12 GHz. To correct for the change in coupling coefficient of C_1 and C_2, each S-parameter is normalized, by software, to the short at that frequency. This procedure is equivalent to making measurements on a point by point basis. The remaining sources of error are the source mismatch, return mismatch, and reflections from the flexible arm.

In the original Hackborn correction scheme,[6] the imperfect S-parameter test set is represented by an ideal instrument, with an error-network representation connected to each port. The networks are characterized by four S-parameters, which are determined by eight calibration runs with known terminations. In an attempt to simplify this procedure, while still maintaining a good degree of accuracy in the corrections, the magnitude of the source and return mismatch were measured. The results (obtained using the suggested method of the manufacturer) are presented in Table 1, over the 2-12 GHz range.

The return mismatch is seen to be a much larger source of error than the source mismatch. At frequencies where the magnitudes are comparable (5, 7, 10 and 12 GHz), a rigorous correction of these errors would only have a marked effect on a low loss network. The return mismatch is further degraded by reflections from the flexible arm, not included in Table 1. Therefore, the source mismatch is neglected in comparison with the return and flexible arm mismatches, when the reflection coefficient of the arm is measured in the calibration procedure. This is not a strictly correct procedure at some frequencies, as noted earlier. However, when the total error is most troublesome (for example, from 8-9 GHz, when $|\rho|$ of return match is .13), the results are valid. Furthermore, since the reflection coefficients of transistors are on the order of .5, a higher order correction would not improve the accuracy

f(GHz)	$|\rho|$ source match	$|\rho|$ return match
2	.006	.030
3	.025	.080
4	.019	.060
5	.019	.020
6	.006	.040
7	.032	.040
8	.019	.130
9	.019	.130
10	.006	.006
11	.019	.082
12	.032	.040

TABLE 1.   Source match of port 2 of 8746B,
return match of port 1.

61

significantly.

The third calibration, determining the transmission co-
efficient of the flexible arm, includes any frequency dependent
losses due to S_5 and S_6 (Figure 2), and reflections from the
test channel of the frequency converter.

Transistor Test Fixture Model

We have previously described a procedure to measure the
S-parameters of a microwave transistor embedded in a test
fixture.[7] The procedure consisted of first determining the
parameters of the fixture plus transistor, corrected for rf
errors inherent in the HP S-parameter test set. Next, the
corrected properties of the fixture alone were measured, with
the transistor replaced by a section of 50Ω line. Then, using
a simple model for the fixture, the S-matrix of the transistor
alone could be deduced from the measured data.

An additional refinement is added to eliminate the effect
of the APC-7/OSM male adapters used to couple between the
network analyzer and the OSM/microstrip launchers on the test
fixture. The APC-7/OSM adaptors can be considered to be part
of the transistor test fixture, resulting in the model of Figures
3 and 4. In this representation it is assumed that the adapter
mismatches are negligible compared to those of the launchers
(VSWR of adaptors[9] <1.05 for f<12 GHz) so that the adaptors
can be modeled as known lengths of coaxial line. The APC-7
connector of the flexible arm can now be attached directly to
port 1 of the analyzer for the calibration run, with the
phase shift of the extra adaptors taken care of in the software.

These two extra sections of line alter the equations[10]
for determining the inductance and capacitance of the
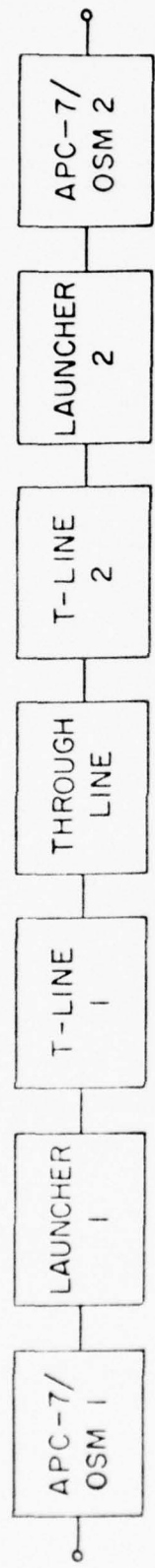OSM/microstrip launchers to the following:

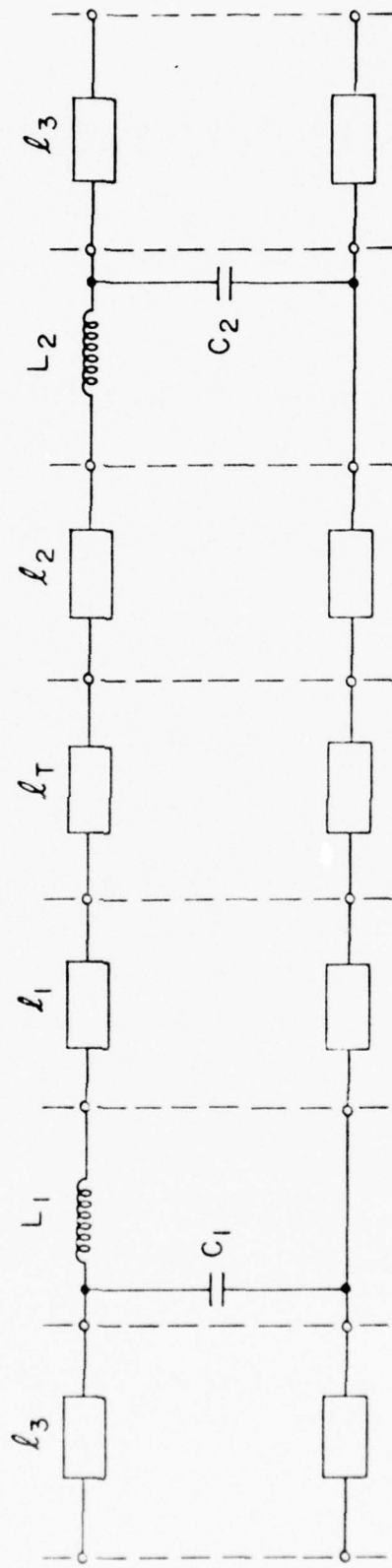Figure 3. Block Diagram of Expanded Transistor Test Fixture.

Figure 4. Circuit Representation of Test Fixture.

63

$$R_e[T_{11}] = M_A\cos\theta_1 - M_B\sin\theta_1 - M_C\cos\theta_2 - M_D\sin\theta_2$$

$$\text{Im}[T_{11}] = M_A\sin\theta_1 + M_B\cos\theta_1 + M_C\sin\theta_2 - M_D\cos\theta_2$$

$$f_1(L,C) = M_A\cos\theta_1 - M_B\sin\theta_1 - M_C\cos\theta_2 - M_D\sin\theta_2 - \text{Re}[T_{11}]_{\text{MEAS.}} = 0$$

$$f_2(L,C) = M_A\sin\theta_1 + M_B\cos\theta_1 + M_C\sin\theta_2 - M_D\cos\theta_2 - \text{Im}[T_{11}]_{\text{MEAS.}} = 0$$

where:

$$\theta_1 = \frac{\omega}{v}(\ell_1 + \ell_T + \ell_2 + 2\ell_3)$$

$$\theta_2 = \frac{\omega}{v}(\ell_1 + \ell_T + \ell_2 - 2\ell_3)$$

ℓ_3 = physical length of APC-7/OSM adaptor. The partial derivatives resulting by applying Equation 25 of reference (10) are correspondingly modified to account for the additional line lengths. Finally, when the T-parameters of the transistor alone are derived from the measured data, one obtains:

$$[T]_{\text{TRANS}} = [T]_{\ell_1}^{-1}[T]_L^{-1}[T]_C^{-1}[T]_{\ell_3}^{-1}[T]_{\text{MEAS}}^{-1}[T]_{\ell_3}^{-1}[T]_C^{-1}[T]_L^{-1}[T]_{\ell_2}^{-1}$$

where $[T]_{\ell_3}^{-1}$ is the inverse of the transmission matrix for the

APC-7/OSM adaptor,

$$[T]^{-1}_{\ell_3} = \begin{bmatrix} e^{j\frac{\omega}{v}\ell_3} & 0 \\ 0 & e^{-j\frac{\omega}{v}\ell_3} \end{bmatrix}^{-1}$$

This improved holder model is currently being evaluated in conjunction with the automated system.

Hardware Expansion

A T.V. typewriter has been assembled to serve as a remote-entry data terminal for the automated system. Purchased in kit form, the unit is similar to that described in the February-April 1975 issues of Radio Electronics. The memory capability, however, has been expanded to provide for two pages of video data, 16 lines of 32 characters per page. The character generator converts from an ASC-II representation to the correct dot pattern of the character being displayed, each character consisting of an array of 35 dots arranged in a 5x7 matrix. A standard nine-inch video monitor is used as the display device.

To the basic character generator has been added a manual/computer-controlled cursor board, giving the user complete control of the cursor position either manually or by software (the next character is entered at the present cursor position, so that the ability to position the cursor is an important one for a versatile terminal). To make the typewriter fully functional as a computer terminal, a UART (Universal Asynchronous Receiver-Transmitter) serial interface board has been added. This unit transmits and receives serial data, the data format being adjusted to match the computer interface employed. The baud rate has been set at 110, so that the terminal operates at the same speed as an ASR-33 teletype. The I/O connections to

65

the UART board are RS-232 compatible; thus, in order to connect the terminal directly to the teletype port of the PDP-11/40 DL11 asynchronous line interface, an RS-232/20 mil current loop converter was built. The latter employs optical isolators on both the send and receive lines to minimize common mode noise and ground loop currents. All the electronics are housed in a Riker-Maxson hotel reservation terminal chassis, in the space occupied previously by a line printer.

To more fully automate the measurement procedure, the remote switch programming capability of the S-parameter test set is employed. By alternately opening and closing two contacts at the rear of the HP 8746B, all four microwave switches can be controlled. Two transistor switches are utilized to provide the low impedance to ground paths, the base of each device being controlled by a D/A channel of the analogic D/A converter. In this manner, test set switching is effected completely by software, further reducing the element of human error in a calibration run.

Conclusions

The validity of the error model employed in the automated network analyzer system is discussed in terms of the physical sources of mismatch in the HP 8746-B. An improved model for a transistor test fixture is given, expanding the fixture representation to include the APC7/OSM adaptors, in order to eliminate one extra calibration in the measurement procedure.

To expand system I/O capabilities, a remote entry T.V. terminal has been added.

References

1. J. Sutherland and Jeffrey Frey, "An Automated Network Analyzer System," RADC Semi-Annual Report, June 1975.

2. J. Sutherland and Jeffrey Frey, "Automated Measurement of FET S-Parameters," RADC Semi-Annual Report, December 1975.

3. Hewlett Packard, S-Parameter Test Set Operating and Service Manual, 8746B, p. 3-6, 1971.

4. Ibid, p. 4-5.

5. Hewlett Packard, Coaxial Waveguide Catalog, p. 76, 1975.

6. Richard A. Hackborn, "An Automated Network Analyzer System," Microwave Journal, May 1968.

7. J. Sutherland and Jeffrey Frey, "Automated Measurement of FET S-Parameters," RADC Semi-Annual Report, December 1975.

8. J. Sutherland and Jeffrey Frey, "Automated Network Analyzer System," RADC Semi-Annual Report, June 1975.

9. Omni Spectra, Inc., OSM Microwave Components, p. 47, 1974.

10. J. Sutherland and Jeffrey Frey, "Automated Measurement of FET S-Parameters," RADC Semi-Annual Report, December 1975.

MICROWAVE FET FABRICATION STUDIES

R. Gurney, Jeffrey Frey*

During this reporting period several GaAs wafers with epitaxial layers were processed into working FET devices, using the 5 μm gate FET pattern discussed in the previous semi-annual report. DC characterization has shown fairly good agreement with theoretical estimates.

The processing procedure described in earlier reports was generally followed, with certain modifications to improve yield and performance. The wafer is thoroughly cleaned and the mesa pattern defined in AZ-1350B photoresist. Approximately 1 μm of GaAs is etched away in 8:1:1 $H_2SO_4:H_2O_2:H_2O$, being careful not to agitate the solution (doing so causes surface irregularities). The source and drain contacts are also defined in AZ-1350B resist. To clean the surface prior to evaporation, after solvent cleaning the wafer is soaked for 5 minutes in 1:1 HCl: methanol to remove any oxide, and plasma discharge cleaning is performed for 2-4 minutes at about 4×10^{-2} T pressure of argon. The following metals are evaporated: 50Å Ni, 700Å AuGe (88:12) and 300Å Ni. We have found it to be very important that the proper composition of Au and Ge be deposited on the wafer. Since the two materials have different vapor pressures, they evaporate at different rates. To insure that the desired ratio is deposited, the source material should be evaporated completely away. Preventing pinholes in the thin film by keeping the substrate surface dust-free is also necessary. Alloying is performed on a strip heater in H_2 atmosphere by raising the temperature for about 65 seconds, holding it at 450°C for 20 seconds, and finally rapidly lowering the temperature. Under these conditions only slight balling up is observed and

---

*Project Supervisor

the contact resistance is reasonable.

Since the last report, changes have been made in the way
the gate metal is deposited. Pure Al in the narrow gate stripe
was often found to have peeled away from the GaAs despite careful
solvent cleaning. One step dropped was the heating of the
substrate to about $100^{O}C$ in the evaporator. Although the heating
cleans the surface better, it also causes plastic flow of the
AZ-1350J photoresist, so that sharp edges become rounded, making
the metal liftoff much more difficult. Plasma discharge cleaning,
next used, definitely improved the Al adhesion, but at the ex-
pense of very high reverse Schottky leakage current. Removing
the Al, etching away 0.6 µm of GaAs, and replacing the Al gate
without using discharge cleaning greatly reduced the leakage
(less than 1 µA). The final change was the addition of a thin
(about $100\overset{O}{A}$) layer of Cr beneath the Al. The Cr significantly
improved adhesion and changed the Schottky characteristics very
little. Typical reverse current was below 1 µA. Reverse break-
down voltage was lower than that predicted by one-sided abrupt
junction avalanche theory, generally by a factor of 1/3 - 1/2.
Some of this reduction is believed caused by high fields
around the edge of the metal. Some researchers have reported
improvement in the Schottky characteristics by annealing the
diode at high temperature, typically $400-450^{O}C$, for a few
minutes.[1] We tried this step on two wafers, but saw no
improvement: breakdown voltage was reduced, and reverse current
was slightly larger. Possibly some other effect on the ohmic
contacts was masking the diode results, however.

After processing a few of the wafers, a fourth mask was
added to the set so a Au overlayer, visible in Figure 1, could
be deposited over the ohmic contacts. This layer spreads the
current evenly across the pad and lowers the resistivity. By
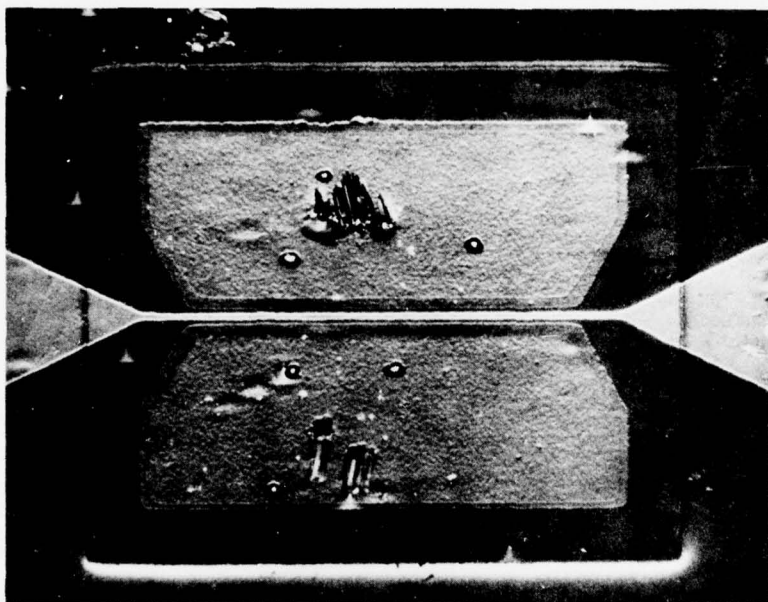using the Au it was easier to achieve reasonable source

Figure 1.   Photograph of FET showing gold layer on
top of ohmic contacts.   Some AuGe balling-
up is visible.

resistances; for example, two comparison FET's had their total source-drain resistance lowered from about 25 down to 17 ohms, a 32% reduction. FETs without the gold sometimes burned out under probe test because high current was confined to a small area of the pad. With the overlayer, this form of burnout has been eliminated, and higher drain currents can be passed.

Comparison of the measured transconductance with that predicted by the theory of Hower and Bechtel[2] was made. The correlation of the observed values with the estimated ones as corrected for source resistance was fairly good (generally within 20%), but because of high source resistance the early FETs did not approach the intrinsic $g_{m\ sat}$ values closely. With improved processing of the ohmic contact material and the use of the gold overlay, the best FETs on the last two wafers have performed much better (about 60% of maximum $g_{m\ sat}$ as compared to less than 10%). Typical values obtained for $g_{m\ sat}$ were 15-20 mS, with source resistance below 15 ohms.

Illumination of the FET with a microscope lamp made a substantial change in the characteristic. The extra carriers generated by the light lowered the channel resistance, thus permitting the drain current to rise to saturation more sharply. Figures 2 and 3 show the I-V characteristics for the same FET with and without light.

Several of the FETs behaved as though surface or epi-substrate interface traps were affecting their behavior. A number of devices exhibited large loops at high values of V_D and V_G, along with a rise in I_{DS}, as illustrated in Figure 4. The phenomenon is believed caused by the release of electrons from traps at the epilayer-substrate interface. A few FETs displayed noise or oscillation at high V_D and low V_G, as shown in Figure 5. The effect, not understood completely, may arise from the bulk
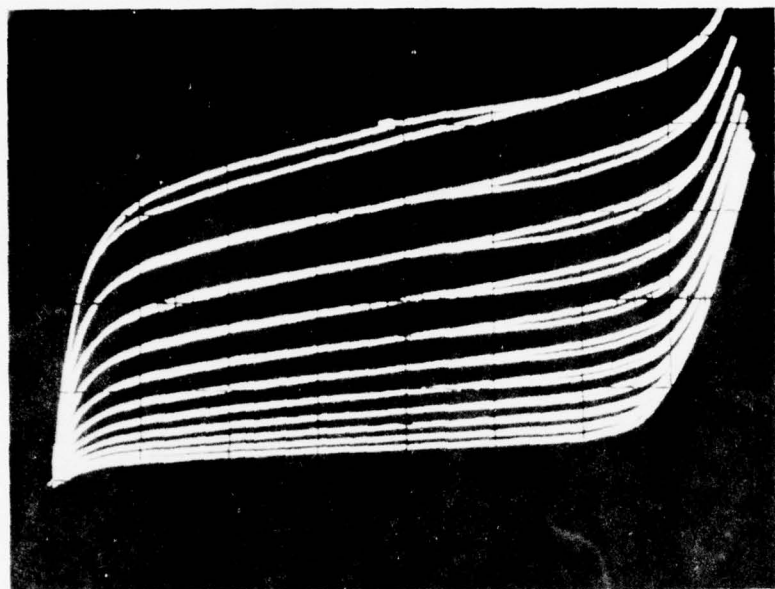
71

Figure 2.   I-V characteristic, with light off.   (LD073502
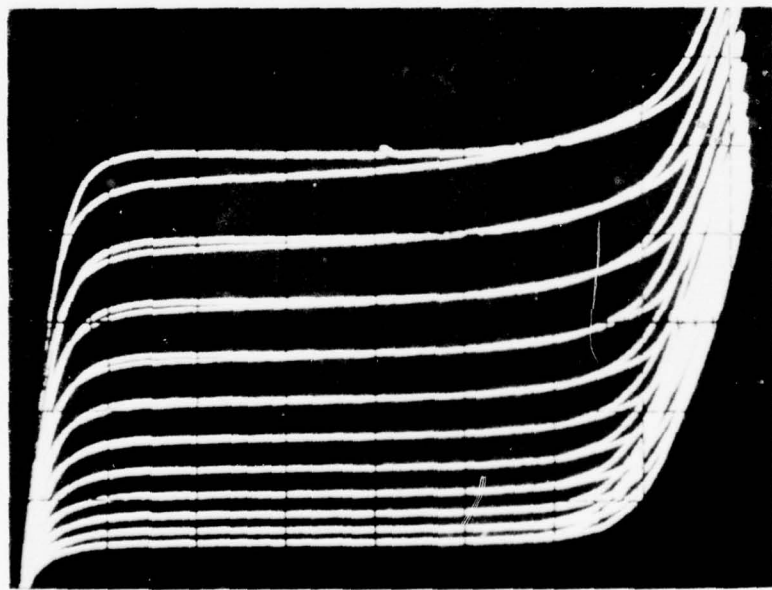#2)   2V, 2mA/div; -0.1 V/gate step.

Figure 3.   I-V characteristic, with light on, for same
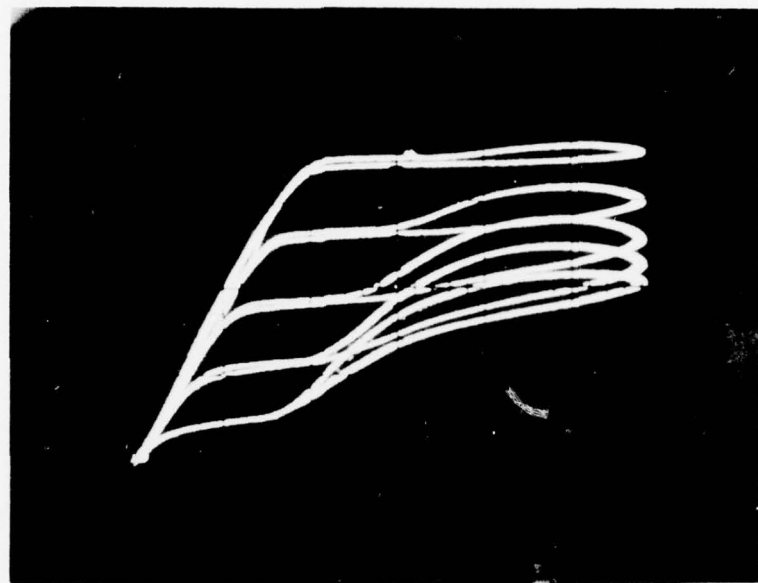FET as in Figure 3.   Same scale.

72

Figure 4.   I-V characteristic showing looping and elevated I_{DS}.   (LD073504 #6)   5V, 10 mA/div; -1 V/gate step.
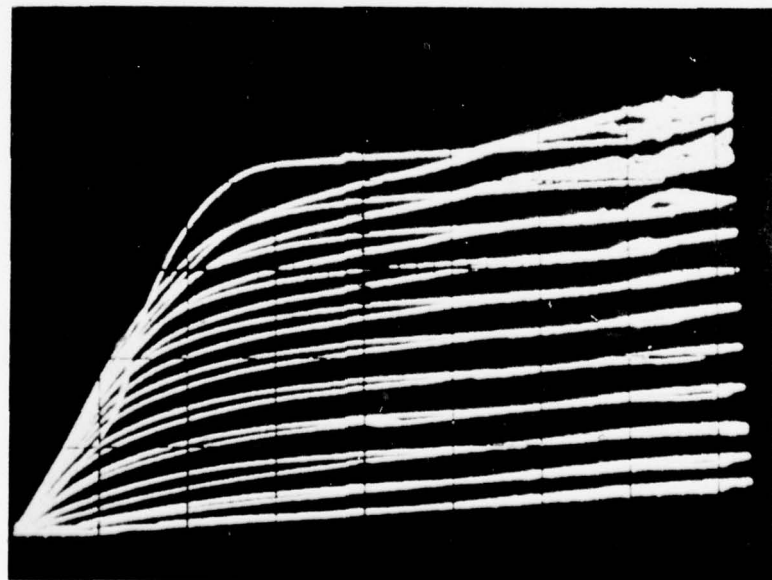

Figure 5.   I-V characteristic illustrating noise at high V_D.   (LD063402   #8) 5V, 1 mA/div; -1 V/gate step.

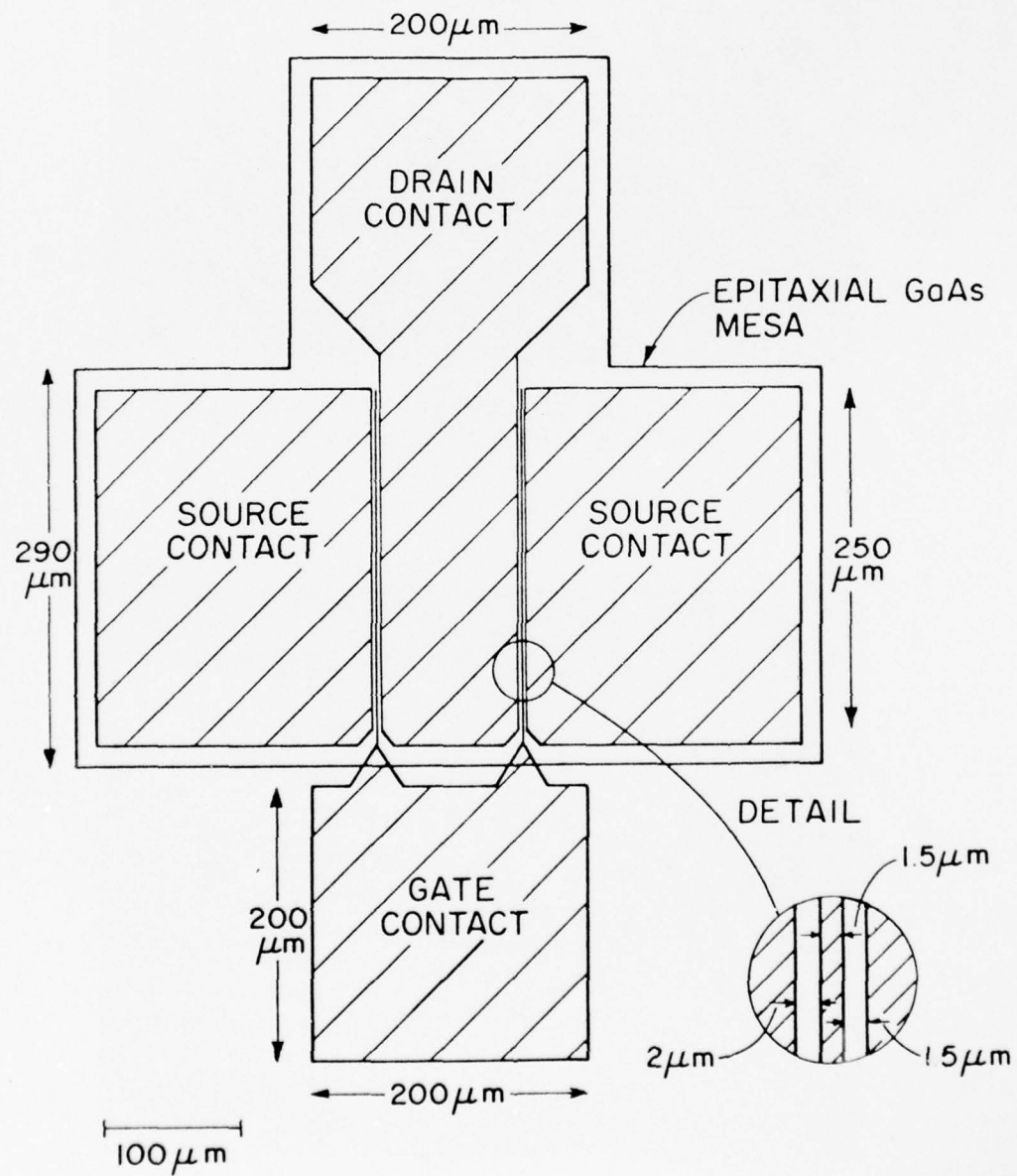# HIGH FREQUENCY SPLIT GATE FET
STRUCTURE

Figure 6. Schematic Layout of 8-10 GHz FET Pattern.

74

negative conductivity in the channel at high field values.

Toward the end of the reporting period a new FET pattern was designed, as shown in Figure 6. Since the mask-making facilities here could not reliably resolve such small dimensions, a commercial firm made the photomasks from our Rubylith artwork. The mask set has been received and will be tested during the next reporting interval.

References

1. O. Wada, S. Yanagisawa, and H. Takanashi, "The Effect of Heat Treatment on Al-GaAs Schottky Barriers," Japan J. Appl. Phys., 12, 1973, p. 1814.

2. P. L. Hower and N. G. Bechtel, "Current Saturation and Small-Signal Characteristics of GaAs Field-Effect Transistors," IEEE Trans. Elec. Dev., ED-20, 1973, p. 213.

Investigation of Ion-Implanted Silicon Read IMPATT
Diodes
Aditya K. Gupta, G. C. Dalman[*], C. A. Lee[*]

This study was initiated to investigate the dc and rf
characteristics of p-type, Silicon Read IMPATT diodes. We
propose to compare and evaluate the performance of diodes
with different doping profiles. This should help us in arriving
at an optimum doping profile for such diodes. Silicon was
chosen as the semiconductor because high quality wafers are
readily available and the fabrication technology is relatively
well established. Ion implantation will be used to dope the
semiconductor instead of conventional diffusion methods because
arbitrary doping profiles are easily obtainable by using multi-
ple implantations. In addition, it is possible to get hyper-
abrupt uniform junctions in thin epilayers. Thus, higher
frequency, better thermal conduction, cooler operation and higher
output powers can be achieved.

We have so far made three practice runs on wafers which
had been implanted earlier at IBM's Thomas Watson Research
Center. Two of the runs were made with wafer #P5 and one
with wafer #P4. The particulars of these wafers are given
below:

1) Wafer #P4: p epilayer on p+ substrate; epilayer is
    9μ thick and its resistivity is 6.8 Ωcm; substrate
    is 10 mils thick. The epilayer was predamaged by a
    silicon implant. This was done to make it amorphous
    and thus prevent channeling of the other implants.
    The wafer was then implanted with boron and with
    phosphorous to produce a n+p+pp+ structure.

*Project Supervisor

76

2) Wafer #P5: p epilayer on p+ substrate; epilayer is
    8μ thick and its resistivity is 7Ωcm; substrate is
    10 mils thick. The epilayer was predamaged by a silicon
    implant as before. It was then implanted with boron
    and arsenic to form a n+p+pp+ structure.

The wafers were cleaned and then annealed at 950°C for
30 minutes in an atmosphere of pure hydrogen. Next, chromium
and gold were sputtered on the implanted side to make an
ohmic contact. The substrate was mechanically and chemically
polished to reduce its thickness from 10 mils to 3 mils. This
was done to reduce the parasitic resistance of the diode and to
ease the dicing of the wafer. Chromium and gold were then
sputtered on the substrate side to form the second ohmic contact.
The wafer was scribed and diced into 5 mil by 5 mil diodes. A
few of these diodes were bonded on gold ribbons and their dc
characteristics were tested. So far, all the diodes have been
found to be excessively 'leaky'. They do not have any
well defined breakdown voltage even after they have been etched,
to remove surface damage. We suspect that the heavily damaged
region produced by predamaging the epilayer does not get
properly annealed at 950°C and results in a poor junction. One
solution is to anneal the implanted wafer at still higher
temperatures so that diffusion will push the p+n+ junction
beyond the damaged region.

The furnace used to anneal these wafers cannot be heated to
more than 1000°C. We have now set up a facility for vacuum
annealing at temperatures greater than 1000°C. This will be
used to fabricate more diodes from wafers P4 and P5. We are
also trying to implant new wafers at the ion-implantation facility
of Cornell University. At present we are having problems in
getting a sufficiently strong ion current of boron. We hope
to overcome this difficulty by changing the source gas.

BROADBAND GaAs FET AMPLIFIER STUDY

Wendell C. Petersen, Walter H. Ku[*]

Introduction

Analytical and computer-aided design techniques for
broadband GaAs FET amplifiers are presented. Based on distri-
buted models of the FET, optimum gain-bandwidth limitations
have been derived. These results are similar to those publish-
ed previously which are based on lumped equivalent circuit
models of the transistor[1]. The distributed case was also
studied by Tucker and he had derived some explicit results for
a class of different ideal gain functions[2]. The effect of
altering the commensurate line length of the models has also
been studied.

A closed form expression is derived for lumped tapered
gain matching networks with maximally flat error and an
algorithm is presented which can be used to obtain both lumped
and distributed tapered gain matching networks with an exact
equiripple error. In both cases, the matching networks can
have an arbitrary number of transmission zeros at 0 and ∞,
provided that the order of the matching network is even.
These matching networks are a distinct improvement over those
previously derived by Pitzalis[3], Ku and Petersen[1], Mellor[4],
and Tucker[5]. An extensive set of tables of explicit element
values for lumped and distributed matching networks with
octave and 3:1 bandwidths have been derived. These results
have been applied to the design of 1μ-gate GaAs FET amplifiers.

Broadband Transistor Amplifiers

The basic single-stage broadband transistor amplifier
configuration is shown in Figure 1. The input and output
matching networks are assumed to be lossless but can be
either lumped or distributed. In the latter case, the trans-
mission line elements are assumed to be commensurate although
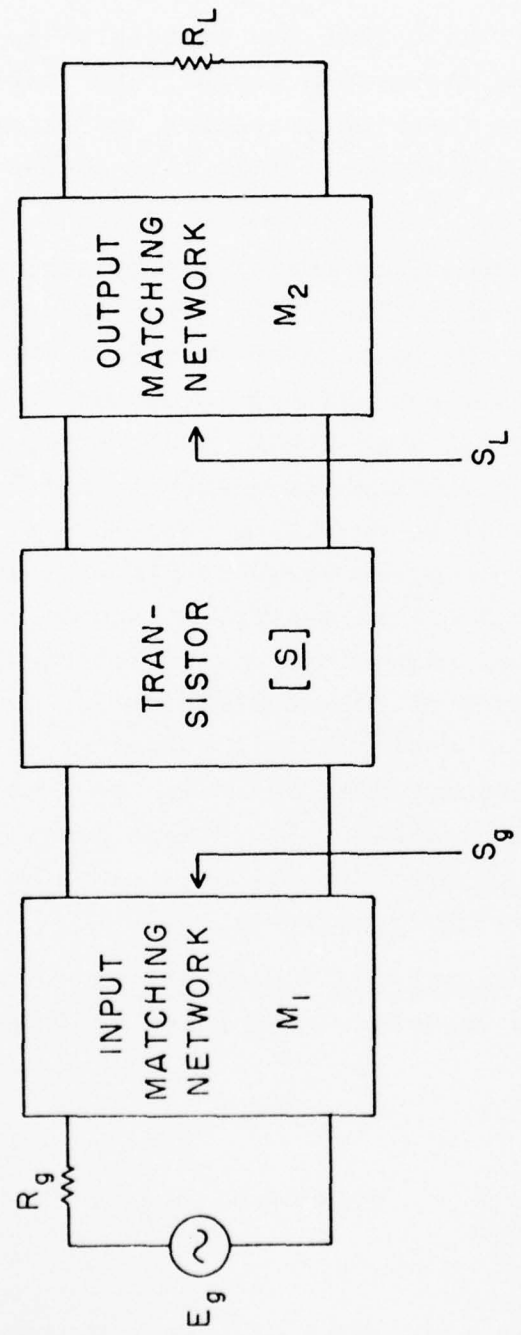
Figure 1. Basic Single-Stage Broadband Transistor Amplifier Configuration.

the line length of the input and output matching networks
need not be equal.

It is assumed initially that the transistor is uni-
lateral, $s_{12} = 0$. This assumption can be taken care of sub-
sequently either by the final optimization and/or remodeling
of the equivalent circuit model to take into account the non-
zero s_{12}.

The maximum available gain (MAG) of a typical high-freq-
uency transistor is shown in Figure 2. This is defined to be
the gain obtained from the transistor when both the input and
output are simultaneously conjugate matched and is undefined
when the transistor is not absolutely stable (from ω_a to ω_b
in Figure 2). In a typical high-frequency transistor ampli-
fier, the transistor will be operating over some prescribed
frequency band from ω_ℓ to ω_h as shown in Figure 2 and the
intrinsic gain will roll-off at a slope of approximately
6 dB/octave. The actual gain slope can be between 3 dB/octave
and 8 dB/octave depending on the specific device. To obtain
an amplifier with a flat over-all gain response, either the
input or the output matching network must have a compensating
gain taper as shown in Figure 3. It is also possible and
sometimes necessary to distribute the gain taper between the
input and the output matching networks.

Optimum Distributed Gain-Bandwidth Limitations

The ideal tapered magnitude gain function is given by

$$
G_I(\omega) = \left\{
\begin{array}{lll}
K(\frac{\omega}{\omega_h})^{\alpha} & ; & \omega_\ell \leq \omega \leq \omega_h \\
\\
0 & ; & \text{elsewhere}
\end{array}
\right\} , \tag{1}
$$

where

$$
\alpha = \frac{S}{10 \, \log 2} , \tag{2}
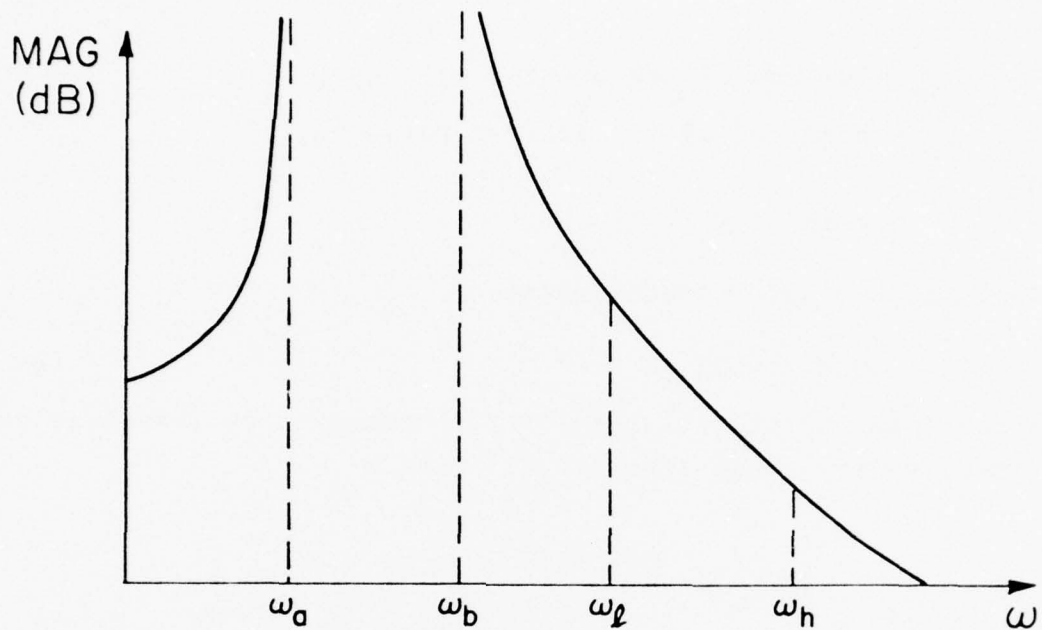$$

S = gain slope in dB/octave,

80

Figure 2. Typical Maximum Available Gain versus Frequency of a High-Frequency Transistor.
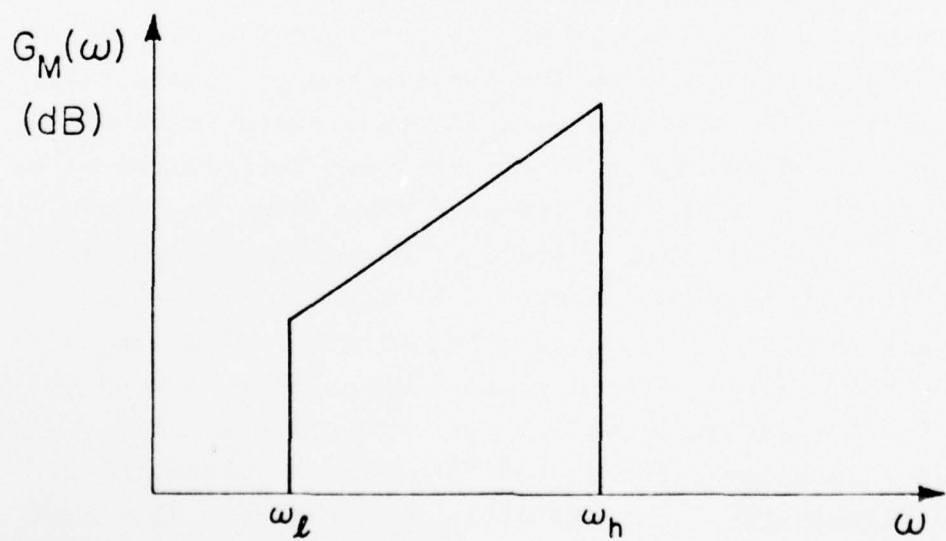

Figure 3. Ideal Gain Function of the Broadband Matching Network.

ω_ℓ = low end of the desired passband,

ω_h = high end of the desired passband,

and

K = gain at ω_h.

Applying Richards' transformation[6]

$$\Omega = \tan \omega T \quad , \tag{3}$$

where T is the delay length of the commensurate transmission lines, so the ideal taper of (1) yields

$$G_I(\Omega) = \begin{cases} \dfrac{K}{(T\omega_h)^\alpha} \left[\tan^{-1}\Omega\right]^\alpha ; & \Omega_\ell \leq \Omega \leq \Omega_h \\ 0 & ; \quad \text{elsewhere} \end{cases} \quad , \tag{4}$$

where

$$\Omega_\ell = \tan \omega_\ell T, \tag{5}$$

and

$$\Omega_h = \tan \omega_h T. \tag{6}$$

The ideal gain-bandwidth limitations for distributed element matching networks can now be obtained for the ideal tapered gain function (4) by the application of Bode's integral restrictions[7]. The distributed load constraints to be considered are shown in Figure 4. Tucker[2] has derived the gain-bandwidth limitation for the low-pass case shown in Figure 4(a) (or its dual in Figure 4(b)) with a different ideal gain function, consisting of the ideal taper presented in (4) with Ω_ℓ set equal to zero for $\Omega \leq \Omega_h$ and its reflection around Ω_h for $\Omega \geq \Omega_h$. Tucker's ideal gain function does not account for changes in bandwidth, which are important for low values of gain slope S and is too pessimistic for matching networks with a sharp roll-off above Ω_h. Although it should not be considered an ideal limit, Tucker's gain function is useful in estimating gain-bandwidth restrictions especially
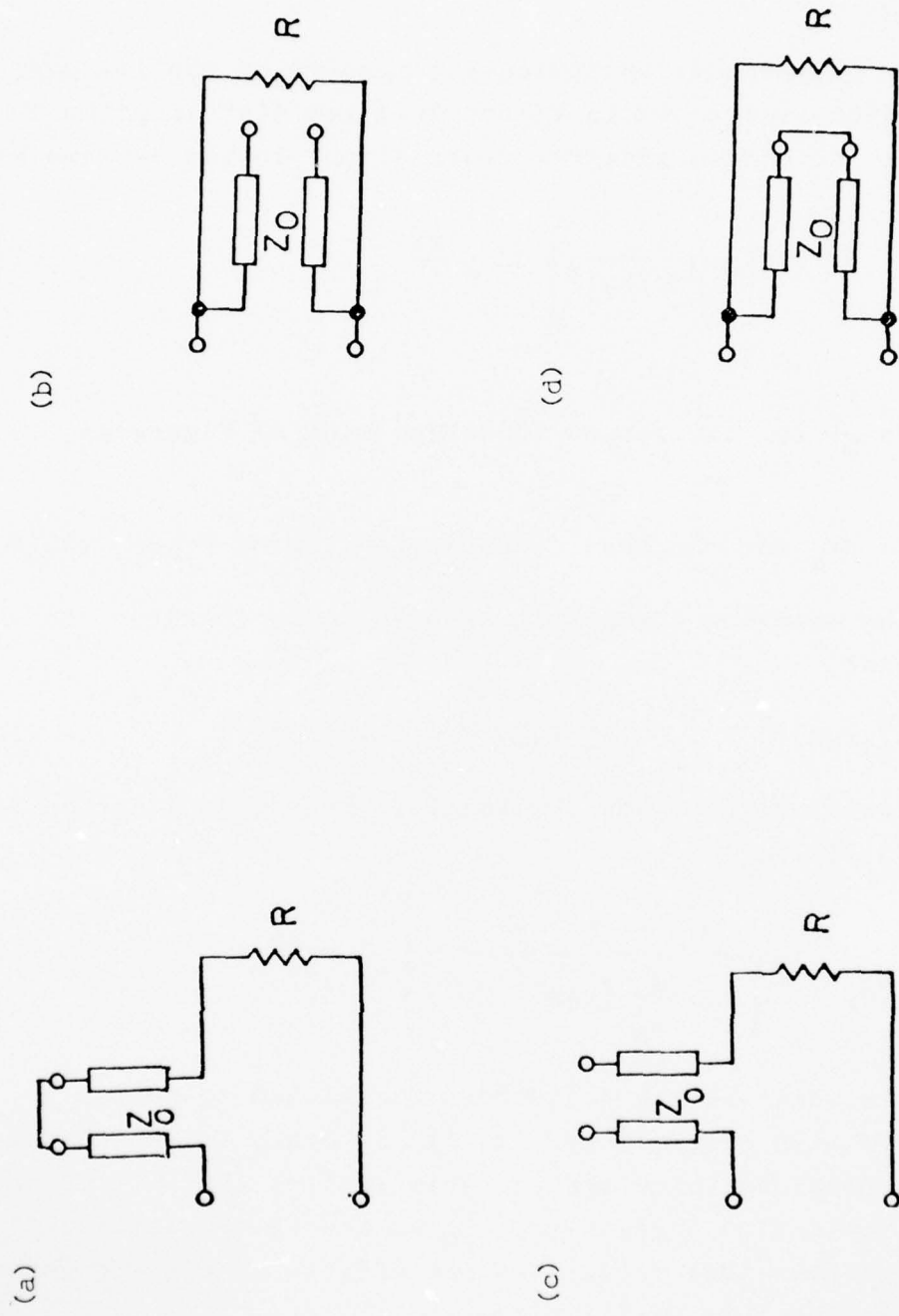
82

Figure 4. Distributed Equivalent Circuits for Transistor Input and Output Models.

83

if matching networks with symmetric gain functions are employed.

The gain-bandwidth limitation imposed by the low-pass distributed load shown in Figure 4(a) and 4(b) is given in terms of the Bode's integral restriction[7] in the λ-plane as

$$\int_0^\infty \ln\left[\frac{1}{\left[s_{22}^M(j\Omega)\right]^2}\right] d\Omega \leq \frac{2\pi}{\tau} \quad , \tag{7}$$

where

$$\tau = \frac{Z_O}{R} \text{ for the series inductive stub of Figure 4a,} \tag{8}$$

and

$$\tau = RY_O \text{ for the shunt capacitive stub of Figure 4b.} \tag{9}$$

Since the matching network is assumed to be lossless and reciprocal,

$$|s_{22}^M(j\Omega)|^2 = 1 - |s_{21}^M(j\Omega)|^2 = 1 - G_I(\Omega) \ . \tag{10}$$

Substitution of (10) and the ideal tapered gain function (4) into (7) yields

$$\int_{\Omega_\ell}^{\Omega_h} \ln\left\{\frac{1}{1 - \frac{K}{\omega_h^\alpha}\left[\tan^{-1}\Omega\right]^\alpha}\right\} d\Omega = \frac{2\pi}{\tau} \ , \tag{11}$$

where the delay length T has been normalized to unity. The equal sign was selected in (11) in order to obtain the largest possible value for τ. This implies that all zeros of the reflection coefficient $s_{22}^M(\lambda)$ are in the left-half λ-plane. Fano[8] has calculated the effects of placing zeros of s_{22}^M in the left half λ-plane as

$$\hat{\tau} = \frac{\tau}{1 + \tau \sum\limits_{i} z_i} \quad , \tag{12}$$

where τ is the time constant in (11), $\hat{\tau}$ is the new time constant and z_i are the zeros of s_{22}^{M} in the right-half λ-plane.

For the high-pass distributed loads of Figure 4(c) and 4(d), the gain-bandwidth limitation is given in terms of the integral restriction as

$$\int_{0}^{\infty} \frac{1}{\Omega^2} \ln \left[\frac{1}{\left| s_{22}^{M}(j\Omega) \right|^2} \right] d\Omega \leq 2\pi\tau \quad , \tag{13}$$

where

$\tau = RY_O$ for the series capacitive stub of Figure 4(c),

and

$\tau = \dfrac{Z_O}{R}$ for the shunt inductive stub of Figure 4(d).

Substitution of (10) and the ideal tapered gain function (4) into (13) yields

$$\int_{\Omega_\ell}^{\Omega_h} \frac{1}{\Omega^2} \ln \left\{ \frac{1}{1 - \dfrac{K}{\omega_h^\alpha} \left[\tan^{-1}\Omega \right]^\alpha} \right\} d\Omega = 2\pi\tau \quad . \tag{14}$$

The equality was selected to obtain the optimum gain-bandwidth corresponding to selecting all zeros of $s_{11}^{M}(\lambda)$ in the left-half λ-plane. Fano's relationship for placing the zeros of the reflection coefficient in the right-half λ-plane for the high-pass case is given by

$$\hat{\tau} = \tau + \sum\limits_{i} \left(\frac{1}{z_i} \right) \quad , \tag{15}$$

where τ is the time constant in (14) and $\hat{\tau}$ and z_i are the same as defined in (12). Note that (15) can also be obtained from (12) by using a low-pass to high-pass transformation.

Due to the periodicity of Richards' transformation given in (3), the actual frequency response of the commensurate-line matching networks designed to approximate the ideal gain of (1) will repeat around $\omega_R = \pi/2$ (assuming the normalization $T = 1$) as shown in Figure 5. The relationship between ω_h and ω_R will determine the commensurate line length ℓ; i.e.,

$$\ell = \lambda/M \text{ at } \omega_h , \tag{16}$$

where

$$4. < M = \frac{4\omega_R}{\omega_h} = \frac{2\pi}{\omega_h} = \frac{1}{F_h} \quad \text{for} \quad T = 1 . \tag{17}$$

The gain-bandwidth integral restrictions of (11) and (14) have been integrated numerically for line lengths of $\ell = \lambda/8$ and $\lambda/6$ at ω_h and the results are plotted in Figures 6 and 7. Figure 6 shows the low-pass constraint of (11) for a gain slope S of 3 dB/octave and 6 dB/octave and a gain K of 0, -0.5 dB, and -1.0 dB. Figure 6(a) is for $\ell = \lambda/8$ at ω_h and Figure 6(b) is for $\ell = \lambda/6$ at ω_h. Figure 8 is a similar set of curves for the high-pass constraint of (14). In both Figures 7 and 8, the percent bandwidth is defined as

$$\text{Percent Bandwidth} = 200 \left(\frac{\omega_h - \omega_\ell}{\omega_h + \omega_\ell}\right) . \tag{18}$$

Effect of Commensurate Line Length on Gain-Bandwidth Limitations

In designing the broadband distributed matching networks, the commensurate line length is an additional design para-meter which can be used to trade gain bandwidth as well as practical realization considerations. Care should be taken in comparing the gain-bandwidth limitations for different values of the commensurate line length ℓ since two loads will not have the same reactances over a band of frequencies if they have the same time constant τ but different commensurate line
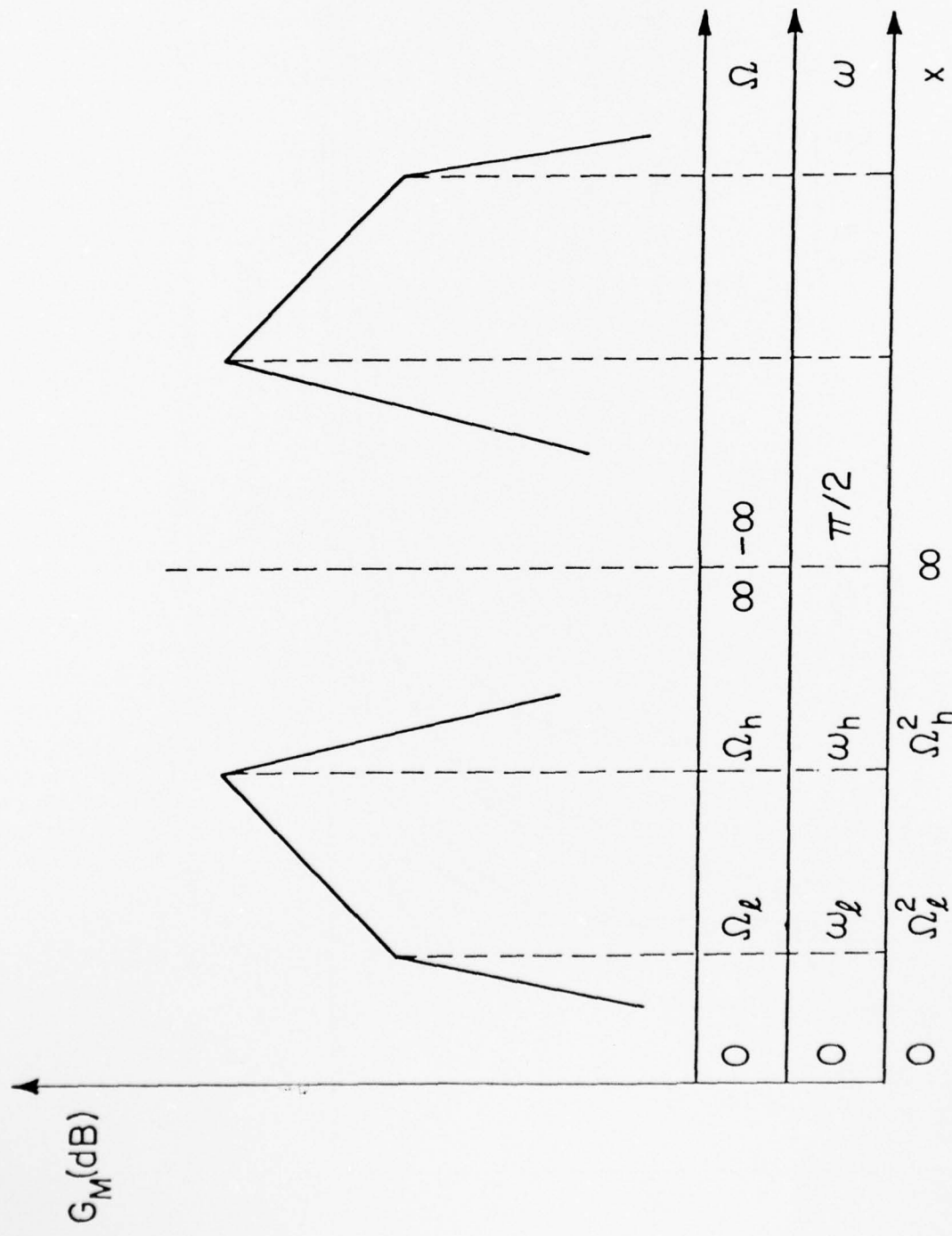
86

Figure 5. Ideal Tapered Gain Characteristic and Frequency Variables for Distributed Commensurate-Line Matching Networks.
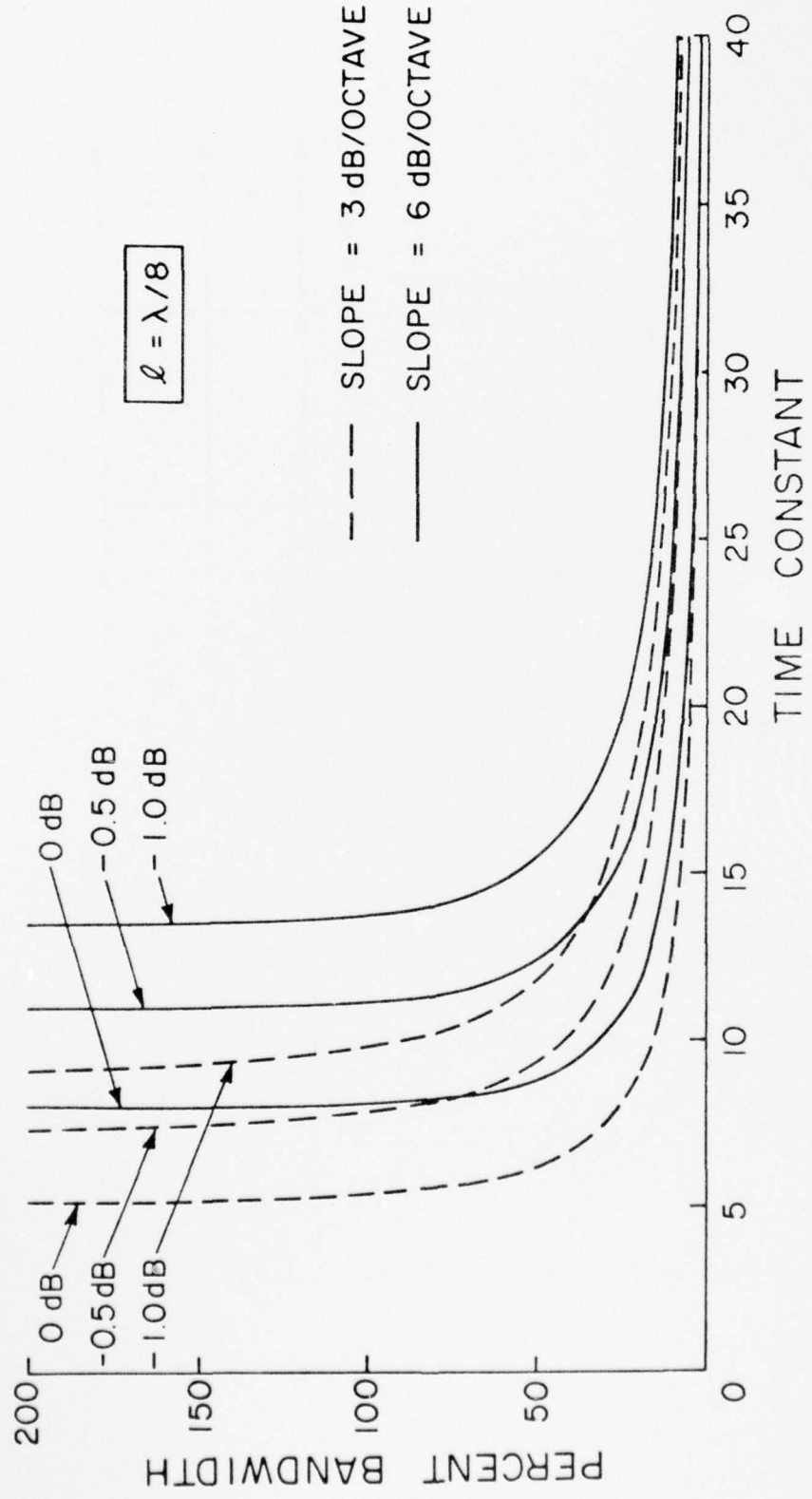
87

Figure 6a. Optimum Distributed Low-Pass Gain-Bandwidth Limitation for $\ell = \lambda/8$.
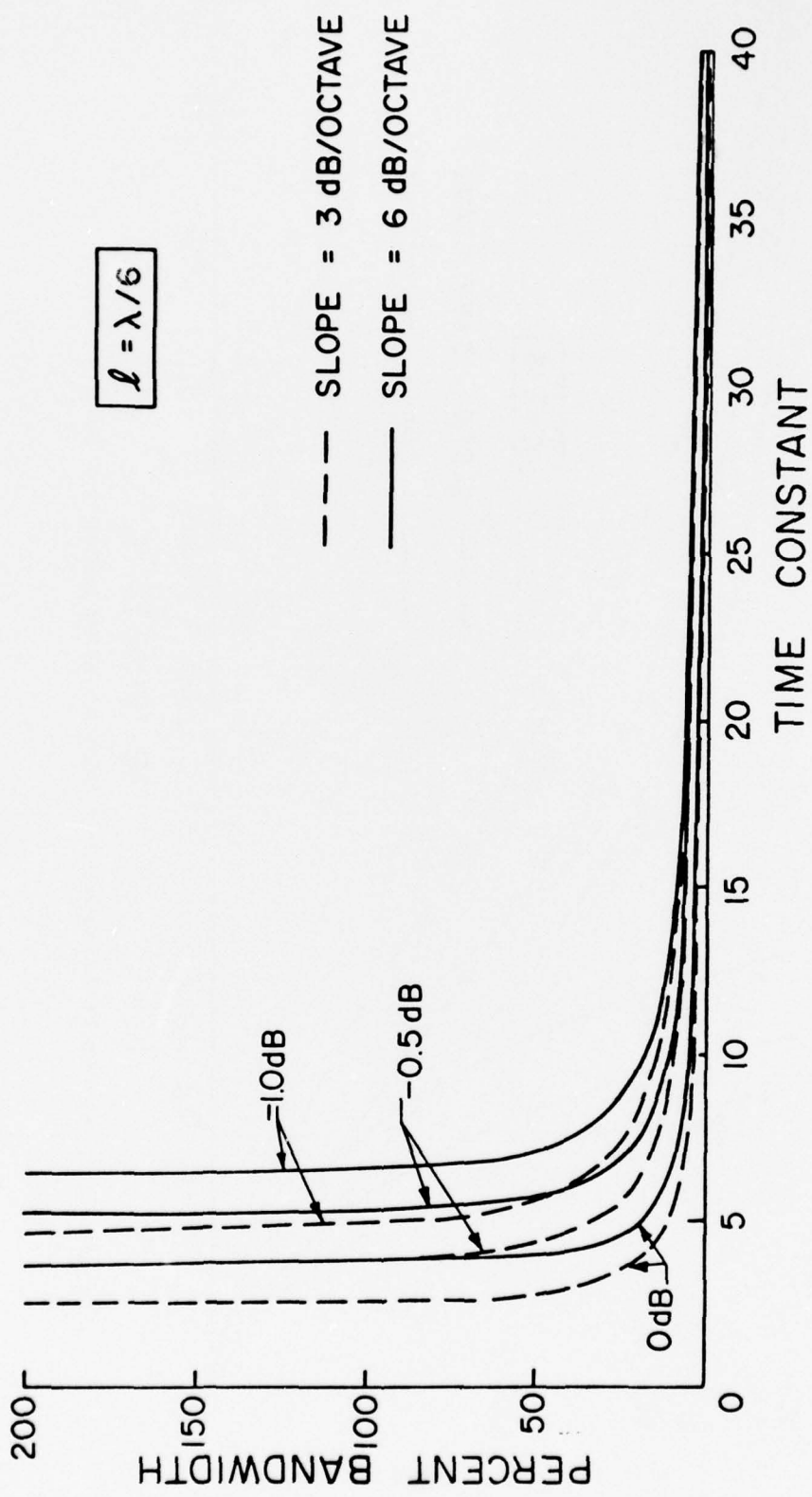
END

DATE
FILMED
4-77

Figure 6b. Optimum Distributed Low-Pass Gain-Bandwidth Limitation for $\ell = \lambda/6$.
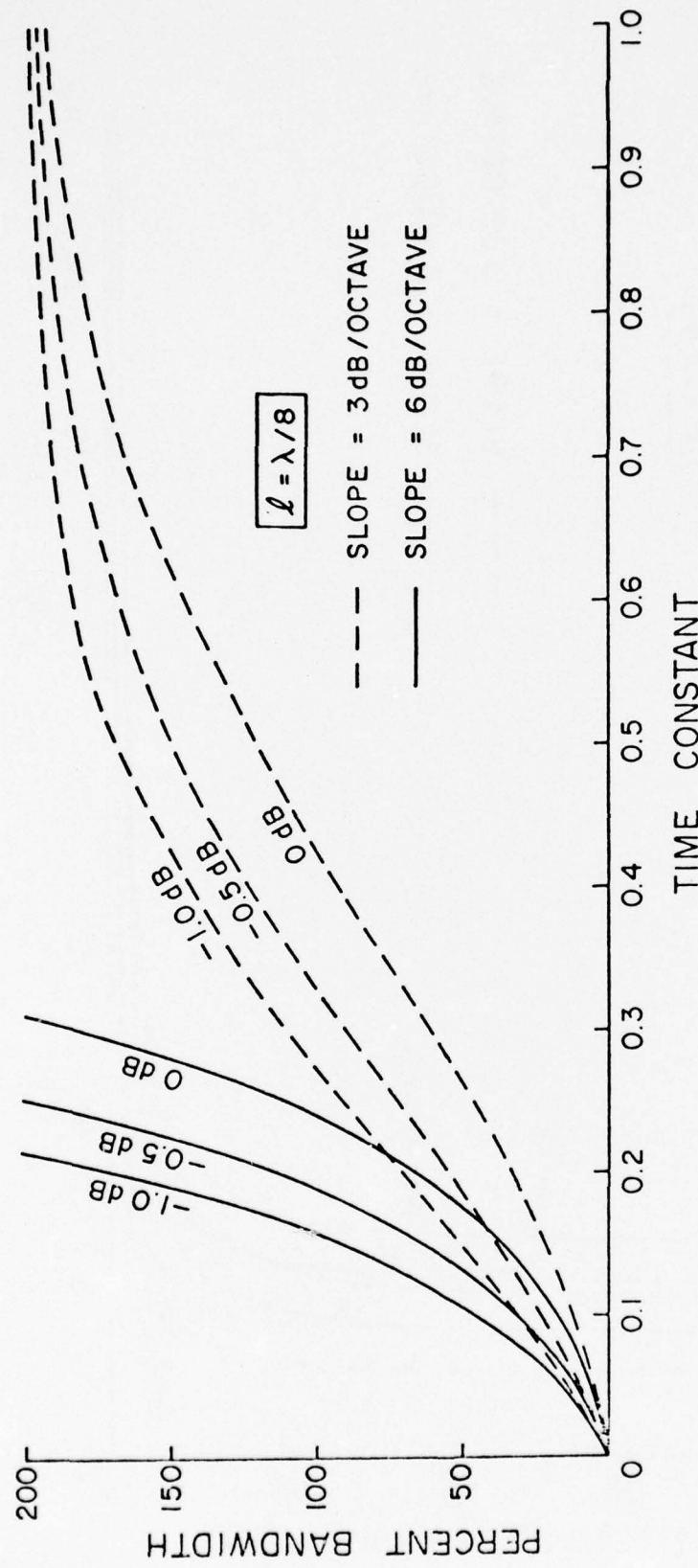
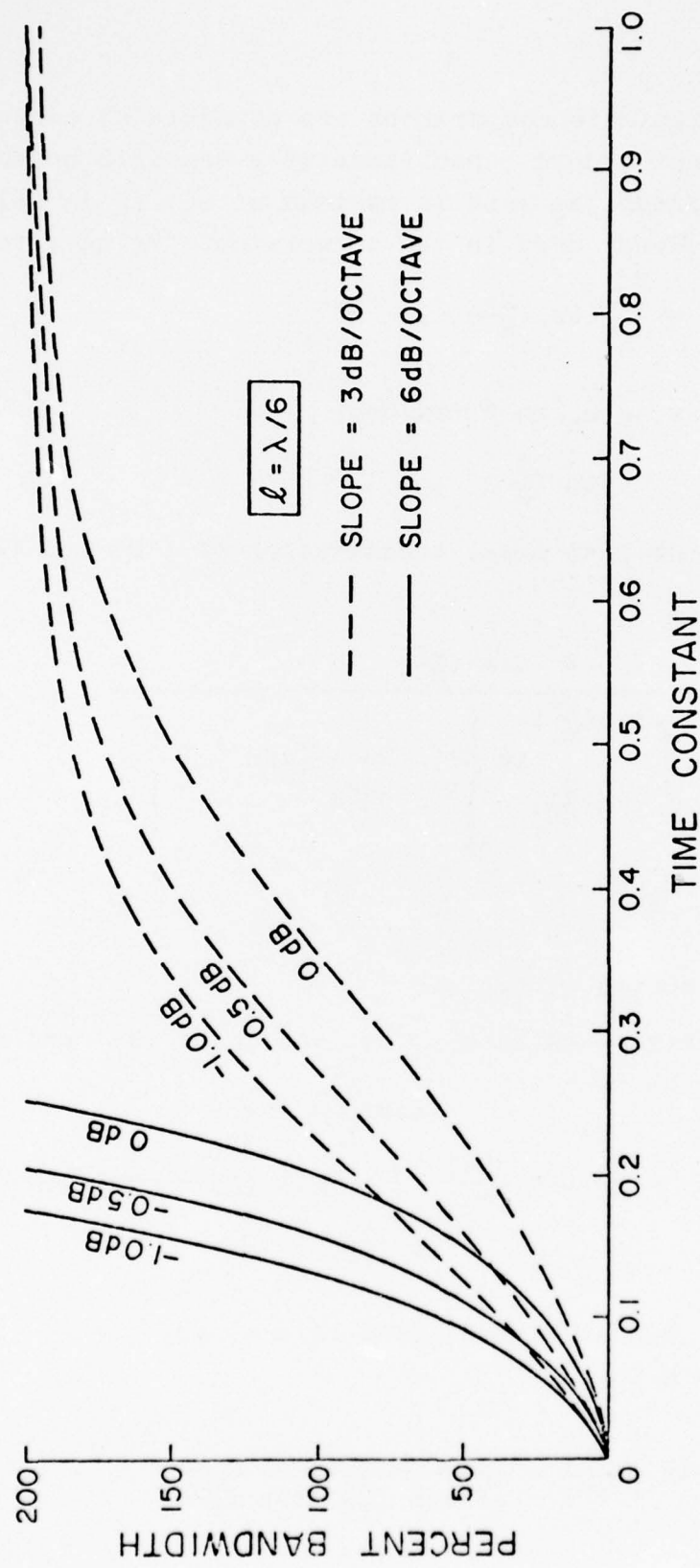Figure 7a. Optimum Distributed high_pass Gain-Bandwidth for ℓ=λ/8.

Figure 7b. Optimum Distributed High-Pass Gain-Bandwidth Limitation for $\ell = \lambda/6$.

lengths. Approximate comparisons are possible by converting
to an equivalent lumped capacitance at a specific prescribed
frequency[5]. Since the gain is maximum at ω_h, ω_h is selected
to be the frequency used in the conversion. We have that

$$C_{eq} = \frac{\tau}{\omega_h} \tan \left(\frac{2\pi}{M}\right) \quad , \tag{19}$$

or, by normalizing ω_h to 1 rad/sec,

$$C_{eq} = \tau \, \tan \left(\frac{2}{M}\right) \quad . \tag{20}$$

For the low-pass case, substitution of (12) and (17) into
(20) yields

$$C_{eq}(LP) = \frac{-2\pi \, \tan \left(\frac{2\pi}{M}\right)}{\int_{\tan\left(\frac{2\pi}{\beta M}\right)}^{\tan\left(\frac{2\pi}{M}\right)} \ell n \left\{ 1 - \frac{K}{\left(\frac{2\pi}{M}\right)^\alpha} \left[\tan^{-1}\Omega\right]^\alpha \right\} d\Omega} \quad , \tag{21}$$

where

$$\beta = \frac{\omega_h}{\omega_\ell} \quad , \tag{22}$$

and M is defined in (17).

For the high-pass case, substitution of (14) and (17)
into (20) yields

$$C_{eq}(HP) = - \frac{1}{2\pi} \, \tan \left(\frac{2\pi}{M}\right) \int_{\tan\left(\frac{2\pi}{\beta M}\right)}^{\tan\left(\frac{2\pi}{M}\right)} \frac{1}{\Omega^2} \ell n \left\{ 1 - \frac{K}{\left(\frac{2\pi}{M}\right)^\alpha} \left[\tan^{-1}\Omega\right]^\alpha \right\} d\Omega . \tag{23}$$

For the special case of zero gain slope, $\alpha = 0$, (21)
and (23) reduce to

$$C_{eq}(LP) \, \ell n \left[\frac{1}{1-K}\right] = \frac{2\pi}{\left[1 - \tan \left(\frac{2\pi}{\beta M}\right) / \tan \left(\frac{2\pi}{M}\right)\right]} \quad , \tag{24}$$

and

$$\frac{\ell n \left[\frac{1}{1-K}\right]}{C_{eq}(HP)} = \frac{2\pi}{\left[\tan(\frac{2\pi}{M})/\tan(\frac{2\pi}{\beta M}) - 1\right]} \quad . \tag{25}$$

Figure 8 is a plot of (24) and (25) for $\beta = (\omega_h/\omega_\ell) = 2, 3, 10,$ and ∞. Note that a single plot is needed for both (24) and (25) since

$$\left[C_{eq}(LP) - \frac{1}{C_{eq}(HP)}\right] \ell n\left[\frac{1}{1-K}\right] = 2\pi \quad . \tag{26}$$

From the results presented in Figure 8, it is clear that the gain-bandwidth restrictions become more severe for the zero-slope case, as the line length is increased, i.e., as M is decreased. This effect is most pronounced for small bandwidths, i.e., small values of β. At the limit of 200% bandwidth, when $\beta = \infty$, C_{eq} is not a function of line length for the special case of zero gain slope.

To obtain similar results for cases with specific gain slopes, (11) and (14) are integrated numerically. The results are presented in Figures 9 and 10 for gain slopes of 3 dB/ octave and 6 dB/octave and bandwidths of 2:1(octave), 3:1, and 10:1. Figure 9 is for the low-pass case corresponding to (11) and Figure 10 is for the high-pass case corresponding to (14). The general trend of the effect of line length is the same as in the zero slope case, but the effect is less pronounced.

## Realizable Approximations to the Ideal Tapered Gain Function

The ideal tapered gain function needed to compensate for the intrinsic transistor gain roll-off characteristic is given in (1). This ideal gain function $G_I(\omega)$ must be approximated by a realizable transfer function to design the required broadband matching network. For lumped matching networks, (1) may be approximated directly, but for distributed

93

Figure 8.   Effect of Line Length on the Gain-Bandwidth
Limitation for the Ideal Zero Gain-Slope
Case with Bandwidth as a Parameter.

Figure 8

Effect of Line Length in the Ideal Zero-Slope Case
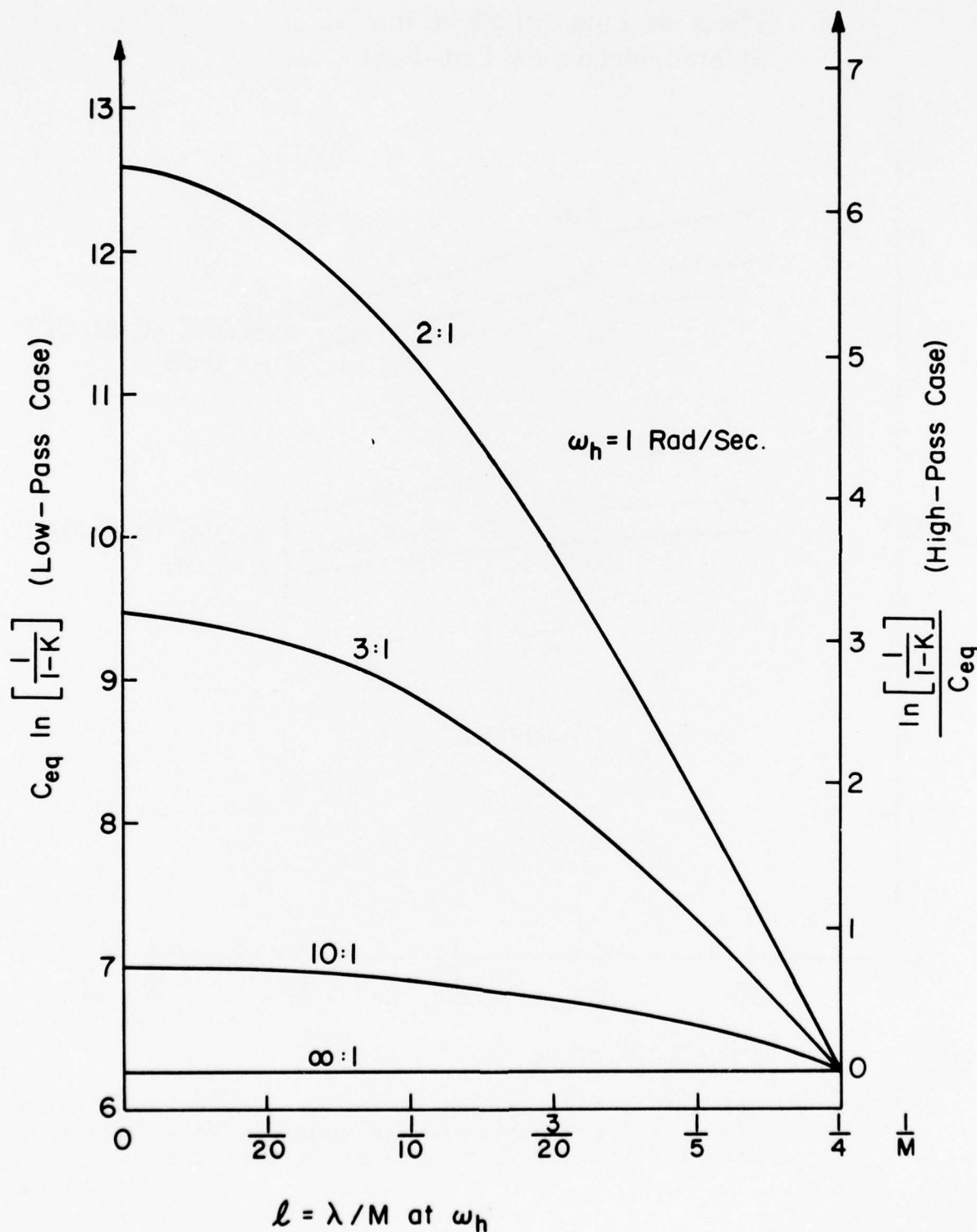
Effect of Line Length in the Ideal Tapered-Magnitude Low-Pass Case

Figure 9. Effect of Line Length on the Gain-Bandwidth Limitation for the Ideal Tapered-Magnitude Low-Pass Case with Bandwidth and Gain Slopes as Parameters.

96

Effect of Line Length in the Ideal Tapered-Magnitude High-Pass Case
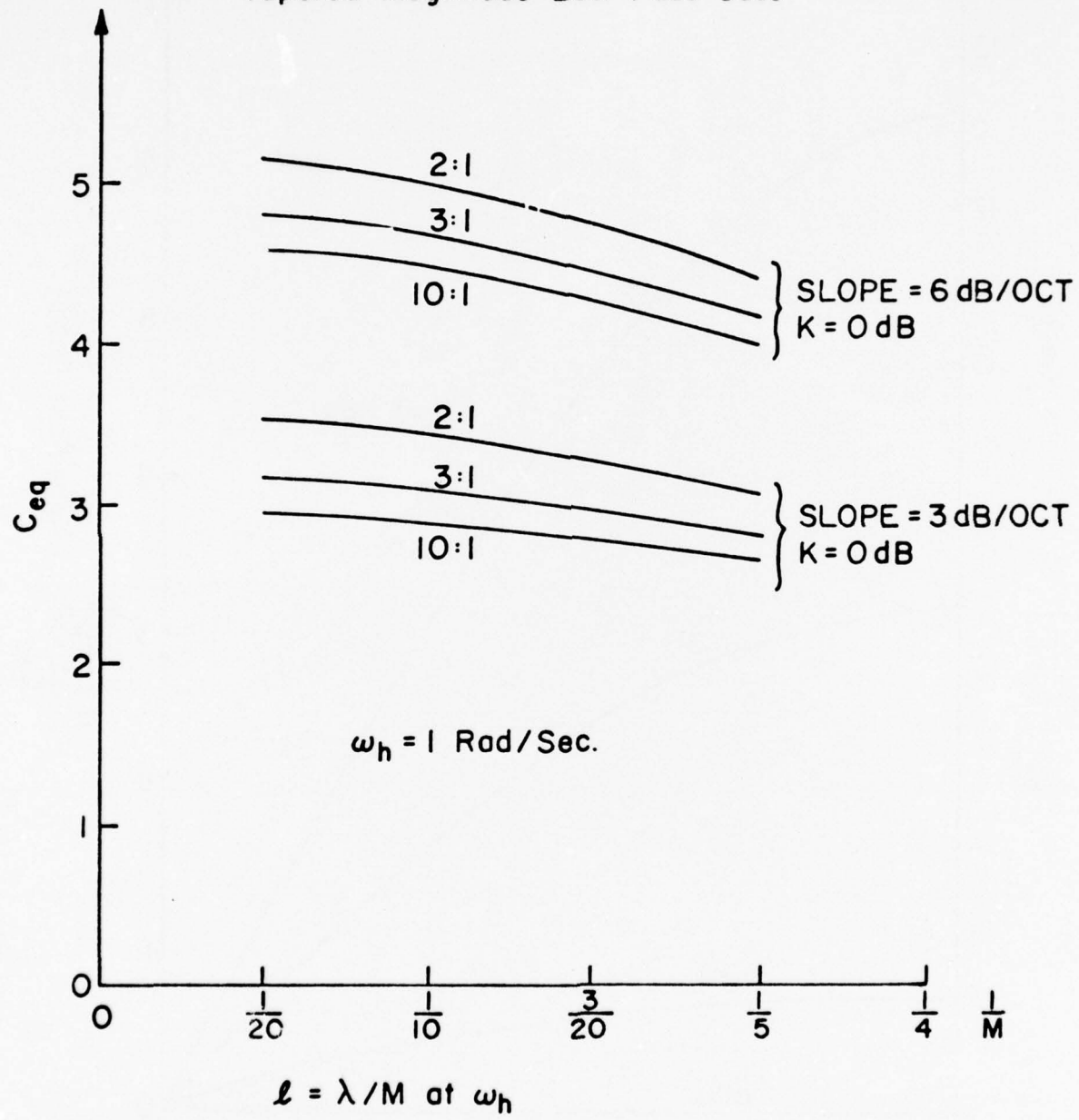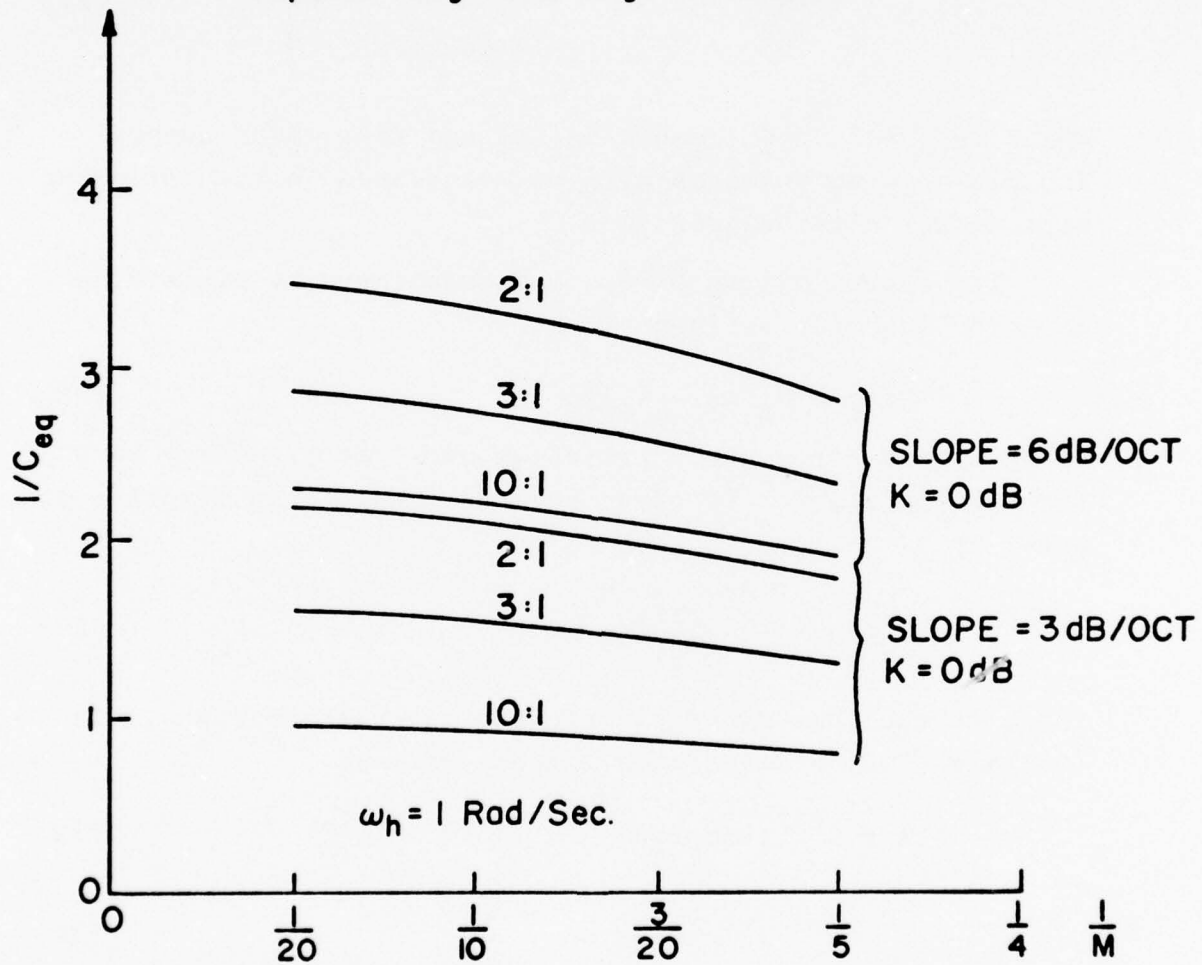

Figure 10. Effect of Line Length on the Gain-Bandwidth Limitation for the Ideal Tapered-Magnitude High-Pass Case with Bandwidth and Gain Slopes as Parameters.

97

matching networks the approximation and the synthesis are most easily carried out in the Richards' transform domain as defined in (3).

In the Richards' transform domain, the ideal tapered gain function is given by

$$
G_I(\Omega) = \left\{ \begin{array}{ll} K\left(\dfrac{\tan^{-1}\Omega}{\tan^{-1}\Omega_h}\right)^{\alpha} & ; \quad \Omega_\ell \leq \Omega \leq \Omega_h \\ \\ 0 & ; \quad \text{elsewhere} \end{array} \right\} , \qquad (27)
$$

which is obtained by combining (1) and (3). Both lumped and distributed networks will be considered in the following approximation techniques.

The approximation of G_I is accomplished by minimizing an error function defined by

$$
E(x) = G_M(x) - G_I(x) \cdot \qquad (28)
$$

using some desired error criterion over the frequency band of interest $[\omega_\ell, \omega_h]$. In (28), the realizable gain function is given by

$$
G_M(x) = \frac{x^{n_h}(1+x)^{n_c}}{P_n(x)} , \qquad (29)
$$

for both the lumped and distributed matching networks. In (28) and (29), x is defined respectively as

$$
x = \omega^2 \quad \text{(Lumped)}, \qquad (30)
$$

or

$$
x = \Omega^2 \quad \text{(Distributed)}. \qquad (31)
$$

The constants in (29) are defined by

$n_\ell \simeq$ number of "low-pass" elements in the matching' network (i.e., the number of transmission zeros at ∞), $\qquad (32)$

98

n_h = number of "high-pass" elements in the matching network (i.e., the number of transmission zeros at the origin), (33)

n_c = number of unit elements (cascaded lines) in the matching network (n_c = 0 for the lumped case), (34)

$n = n_\ell + n_h + n_c,$ (35)

and

$$P_n(x) = b_o + b_1 x + \ldots + b_n x^n. \qquad (36)$$

The change of variable defined in (30) and (31) insures that G_M is an even rational function of ω or Ω. G_M is realizable as a passive network consisting of low-pass, high-pass, and cascaded unit elements provided that $P_n(x)$ is selected such that

$$0 \le G_M(x) \le 1, \qquad \text{for all } x \ge 0. \qquad (37)$$

Maximally-Flat Tapered Gain Functions

To obtain a maximally-flat error function, the coefficients of $P_n(x)$ must be selected such that $E(x)$ and its first $(n-1)$ derivatives are equal to zero at the bandcenter frequency ω_o of the passband. Therefore,

$$\left. \frac{\partial^j E(x)}{\partial x^j} \right|_{x=x_o} = 0, \qquad j = 0, 1, 2, \ldots, (n-1). \qquad (38)$$

This set of conditions will leave one undetermined co-efficient which can be used to adjust the bandwidth of the matching network. Combining (28), (29), and (38), we obtain

$$\left. \frac{\partial^j P_n(x)}{\partial x^j} \right|_{x=x_o} = \left. \frac{\partial^j}{\partial x^j} \left[\frac{x^{n_h}(1+x)^{n_c}}{G_I(x)} \right] \right|_{x=x_o}, \qquad j = 0,1,2,\ldots,(n-1),$$

(39)

99

assuming that $x_o \neq 0$, $x_o \neq 1$, and $P_n(x_o) \neq 0$. Next we define

$$y = x - x_o \ , \tag{40}$$

$$f(y) = \left[\frac{x^{n_h}(1+x)^{n_c}}{G_I(x)}\right]\Bigg|_{x=y+x_o} \ , \tag{41}$$

and

$$Q_n(y) = P_n(y)\Bigg|_{x=y+x_o} = a_o + a_1 y + \ldots + a_n y^n \ . \tag{42}$$

Using (40)-(42), the conditions (39) becomes

$$\frac{\partial^j Q_n(y)}{\partial y^j}\Bigg|_{y=0} = \frac{\partial^j f(y)}{\partial y^j}\Bigg|_{y=0} \ , \quad j = 0,1,2,\ldots,(n-1). \tag{43}$$

The conditions contained in (43) are equivalent to stating that the coefficients of $Q_n(y)$, a_i, are the first n Taylor series coefficients of $f(y)$ except for a_n which is used to control the bandwidth.

The evaluation of the Taylor series of $f(y)$ given by (41) is straight-forward but time consuming especially for the distributed case where $n_c \neq 0$ and the ideal gain function (27) must be used. The results for the general distributed case will not be presented here except to mention that a symbolic differentiation and algebraic manipulation computer program can be used to carry out the required calculations.

For the general lumped case in which $n_c = 0$ and the ideal tapered gain function is given by (1), a general formula for G_M can be derived. Substituting (1), (30), and (40) into (41) with $n_c = 0$, we obtain

$$f(y) = \frac{\omega_h^\alpha}{K}(y + x_o)^{\hat{\alpha}} = (\frac{y}{x_o} + 1)^{\hat{\alpha}}(\frac{\omega_h^\alpha x_o^{\hat{\alpha}}}{K}) \tag{44}$$

100

where

$$\hat{\alpha} = n_h - \frac{\alpha}{2} \quad . \tag{45}$$

From the binomial theorem, the Taylor series of $f(y)$ in (44) is given by

$$f(y) = (\frac{\omega_h^\alpha x_o^{\hat{\alpha}}}{K}) \left[1 + \frac{\hat{\alpha}}{x_o} y + \frac{\hat{\alpha}(\hat{\alpha}-1)}{2! \, x_o^2} y^2 + \frac{\hat{\alpha}(\hat{\alpha}-1)(\hat{\alpha}-2)}{3! \, x_o^3} y_3 \right.$$

$$\left. + \dots \right] \quad . \tag{46}$$

Therefore, $Q_n(y)$ is obtained by truncating (46) after the y^{n-1} term and adding the term $a_n y^n$. From (46), the co-efficients a_i of $Q_n(y)$ are given by the recursion relationship

$$a_o = \frac{\omega_h^\alpha x_o^{\hat{\alpha}}}{K} \quad , \tag{47}$$

$$a_1 = \frac{\hat{\alpha}-i+1}{i \, x_o} a_{i-1}, \quad \text{for} \quad 0 < i < n \quad . \tag{48}$$

The last coefficient a_n is a free parameter to control the bandwidth.

Using (30) and (42) and substituting (47) and (48) into (29) with $n_c = 0$, we obtain the explicit gain function with maximally-flat error for the general tapered lumped matching networks as

$$G_M(\omega) = \frac{(\dfrac{K}{\omega_h^\alpha x_o^{\hat{\alpha}}}) \, x^{n_h}}{\sum\limits_{i=o}^{n-1} \left\{ \dfrac{1}{i!} \left[\prod\limits_{k=1}^{i} (\hat{\alpha}-k+1) \right] (\dfrac{x}{x_o} -1)^i \right\} + a_n (\dfrac{x}{x_o} -1)^n} \quad . \tag{49}$$

This gain function is physically realizable provided (37) is satisfied.

To illustrate the general result for a lumped tapered gain matching network presented in (49), consider a n=4 network with n_h = 2 and a prescribed gain slope of 3.01 dB/octave. From (49), the gain function is given by

$$G_M(\omega^2) = \frac{K \, \omega^4}{1 + 1.5(\omega^2-1) + 0.375(\omega^2-1)^2 - 0.0625(\omega^2-1)^3 + a_4(\omega^2-1)^4} \, ,$$

$$(50)$$

where x_o has been normalized to 1. A plot of (50) is shown in Figure 11 for K = 1 and a_4 = 0.003, 0.1, and 0.2. Note that (50) is realizable (provided that K is properly selected) for $a_4 \geq 0.0625$. When a_4 = 0.0625, the denominator of (50) has a second-order pole at ω = 0 which can be cancelled resulting in a third-order gain function which can also be obtained directly from (49) by setting n = 3, n_h = 1, and a_3 = 0.0625.

The general gain function (49) reduces to a number of special cases which are known. Set S = 0 dB/octave, n = $2n_h$, and x_o = 1, (49) reduces to

$$G_M(\omega^2) = \frac{K \, \omega^n}{\left[(\omega^2-1) + 1\right]^{n/2} + a_n(\omega^2-1)^n} = \frac{K}{1 + (\frac{\omega^2-1}{\omega\omega_c})^n}, (51)$$

where

$$a_n = \frac{1}{(\omega_c)^n} \, . \qquad\qquad (52)$$

The special flat gain function (51) can also be obtained by applying the standard low-pass to band-pass transformation to a maximally-flat low-pass Butterworth gain function. By proper parameter selection, (49) will reduce to all the known maximally-flat gain functions with zero gain slope[9], as well as to all gain functions obtained by multiplying a flat gain function by an integer powers of ω^2 presented by Mellor[4].

TYPICAL GAIN CURVES WITH MAXIMALLY–FLAT ERROR CHARACTERISTIC

FREQUENCY (RAD/SEC)

GAIN

A=0.003

A=0.003

A=0.003

A=0.1

A=0.2

103

Figure 11.
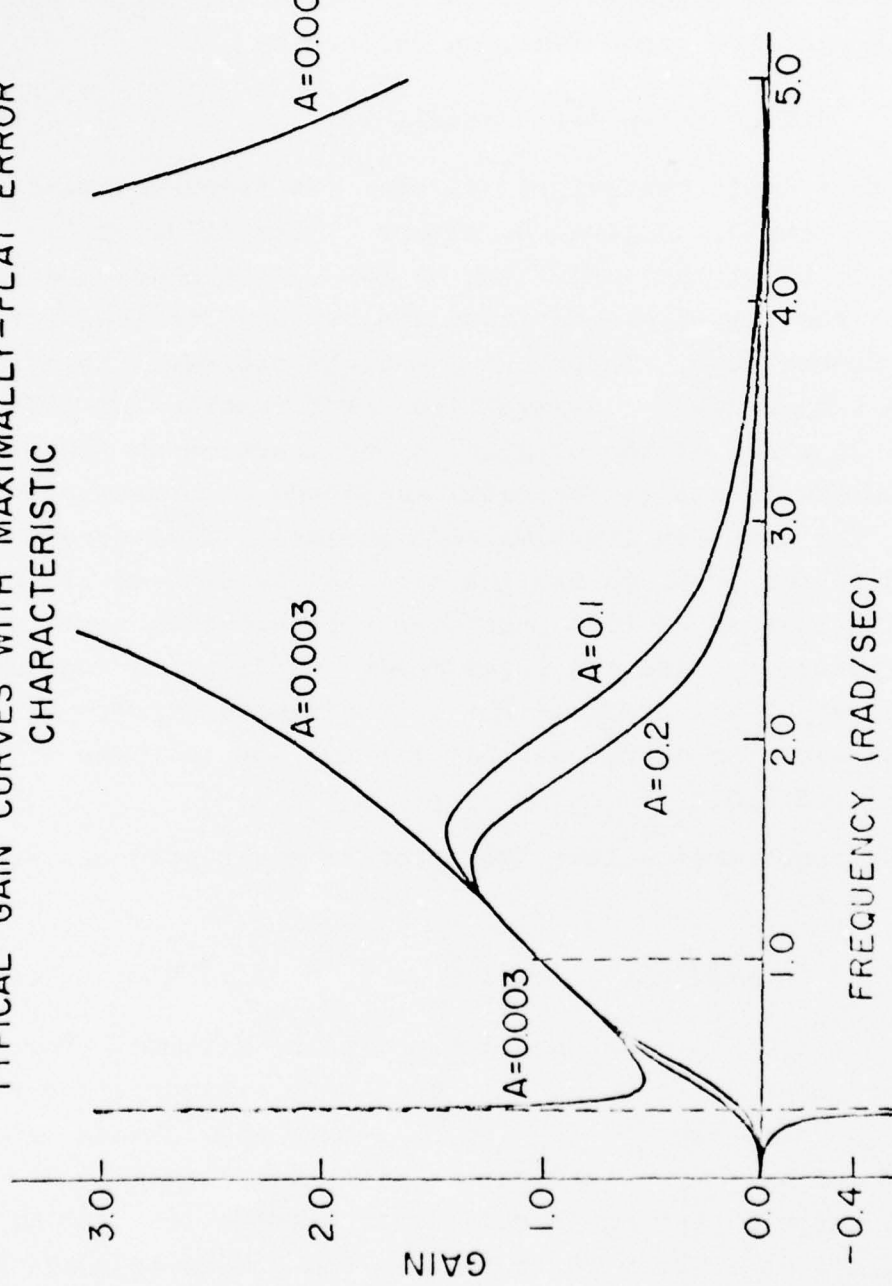
Equiripple Tapered Gain Functions

For an equiripple approximation to the ideal tapered gain function, we approximate G_I of (1) or (27) by a realizable gain function which has an equiripple error characteristic. A numerical algorithm will be derived to obtain $G_M(x)$ such that the modified error function defined by

$$\hat{E}(x) = \ln\left[G_M(x)\right] - \ln\left[G_I(x)\right] \tag{53}$$

has an equiripple characteristic over the frequency band of interest, with $G_I(x)$ given by either (1) or (27). $G_M(x)$ will still be of the form given by (29), with x defined by (30) for the lumped element case and by (31) for the distributed element case. In (29), n_c must be set equal to zero for the lumped case. The modified error function of (53) is used in place of the original error function of (28) in order to obtain ripples of equal magnitude on a decibel scale. The transfer function with maximally-flat error derived in the previous section will not be altered if (53) were used instead of (28) since the approximation is at a single point, x_o, and the logarithmic function has continuous derivatives of all orders. For an equiripple error, (28) and (53) would be identical only for the special case of flat gain, S = 0.

The requirements that the error be equiripple can be expressed as

$$\hat{E}(x_i) = -(-1)^i \epsilon , \quad \text{for } i = 0, 1, 2, \ldots, n , \tag{54}$$

where $x_o < x_1 < \ldots < x_n$ are the points of maximum error. The band edges are forced to be points of maximum error by setting $x_o = \omega_\ell^2$ and $x_n = \omega_h^2$ in the lumped element case and $x_o = \Omega_\ell^2$ and $x_n = \Omega_h^2$ in the distributed element case. In order to insure that G_M is decreasing outside the band of interest, n is restricted to be even and ϵ must be positive. In addition, since the points x_i are the points of maximum

104

error,

$$\frac{d\hat{E}(x)}{dx}\bigg|_{x=x_i} = 0, \quad \text{for } i = 1, 2, \ldots, (n-1). \quad (55)$$

Equations (54) and (55) constitute a set of 2n equations in 2n unknowns x_1, x_2, $\ldots$, x_{n-1} and b_o, b_1, $\ldots$, b_n, which are the coefficients of the denominator of G_M. Once the constants n , n_h, n_c, x_o, x_n, S, and   are specified, these equations must be solved to obtain the transfer function $G_M(x)$.

The solution to (54) is given by

$$\underset{\sim}{b} = \underline{X}^{-1} \underset{\sim}{R}(x) , \quad (56)$$

where

$$\underline{X} = \begin{bmatrix} 1 & x_o & x_o^2 & \cdots & x_o^n \\ 1 & x_1 & x_1^2 & \cdots & x_1^n \\ \cdot & \cdot & \cdot & & \cdot \\ \cdot & \cdot & \cdot & & \cdot \\ \cdot & \cdot & \cdot & & \cdot \\ 1 & x_n & x_n^2 & & x_n^n \end{bmatrix} , \quad (57)$$

$$\underset{\sim}{x} = \begin{bmatrix} x_o & x_1 & x_2 & \cdots & x_n \end{bmatrix}^T , \quad (58)$$

$$\underset{\sim}{b} = \begin{bmatrix} b_o & b_1 & b_2 & \cdots & b_n \end{bmatrix}^T , \quad (59)$$

$$\underset{\sim}{R}(\underset{\sim}{x}) = \left[\frac{x_o^{n_h}(1+x_o)^{n_c}e^\varepsilon}{G_I(x_o)} \quad \frac{x_1^{n_h}(1+x_1)^{n_c}e^{-\varepsilon}}{G_I(x_1)} \right.$$

$$\left. \cdots \quad \frac{x_n^{n_h}(1+x_n)^{n_c}e^\varepsilon}{G_I(x_n)} \right]^T . \quad (60)$$

and the superscript T denotes matrix transpose. Note that $\underline{X}^{-1}$ is well defined since the points x_i are distinct. Substituting (53) and (29) into (55) and cancelling the

105

denominator, we obtain

$$F(x_i) = \{n_c x_i \, P_n(x_i) + [n_h P_n(x_i) - x_i P_n{}'(x_i)](1+x_i)\}\frac{1}{G_I(x_i)}$$

$$+ \, x_i(1+x_i)P_n(x_i) \, \frac{\partial}{\partial x}\left[\frac{1}{G_I(x)}\right]\Bigg|_{x=x_i} = 0, \text{ for } i=1,2,\ldots,(n-1),$$

$$(61)$$

where $F(x_i)$ is the numerator of $\partial\hat{E}(x)/\partial x\big|_{x=x_i}$ and the prime denotes differentiation with respect to x. In (61), $P_n(x)$ is given by (36), (56), and (59).

Newton's method[10] is now used to solve (61) numerically with each iteration given by

$$\hat{x}(k+1) = \hat{x}(k) - \beta \underline{J}^{-1}(\hat{x}(k)) \, \underline{F}(\hat{x}(k)) \quad , \tag{62}$$

where

$$\hat{x} = \begin{bmatrix} x_1 & x_2 & \cdots & x_{n-1} \end{bmatrix}^T \quad , \tag{63}$$

$$\underline{F}(\hat{x}(k)) = \begin{bmatrix} F(x_1^{(k)}) & F(x_2^{(k)}) & \cdots & F(x_{n-1}^{(k)}) \end{bmatrix}^T \quad , \tag{64}$$

and the Jacobian matrix is given by

$$\underline{J}(\hat{x}(k)) = \frac{\partial E(\hat{x})}{\partial \hat{x}}\Bigg|_{\hat{x}=\hat{x}(k)} = \begin{bmatrix} \dfrac{\partial F(x_1)}{\partial x_1} & \dfrac{\partial F(x_1)}{\partial x_2} & \cdots & \dfrac{\partial F(x_1)}{\partial x_{n-1}} \\ \cdot & \cdot & & \cdot \\ \cdot & \cdot & & \cdot \\ \cdot & \cdot & & \cdot \\ \dfrac{\partial F(x_{n-1})}{\partial x_1} & \dfrac{\partial F(x_{n-1})}{\partial x_2} & \cdots & \dfrac{\partial F(x_{n-1})}{\partial x_{n-1}} \end{bmatrix} \tag{65}$$

In (62), the parameter β is usually set equal to unity but may have to be reduced for the first few iterations to improve the convergence properties of (62). Elements of the

106

Jacobian matrix are computed by differentiating (61) to
obtain

$$
\begin{aligned}
\frac{\partial F(x_i)}{\partial x_\ell} = &\Bigg[P_n(x_i)\Bigg\{ (n_c+n_h)\frac{1}{G_I(x_i)} + \Big[(n_c+n_h+2)x_i+n_h+1\Big]\frac{\partial}{\partial x}\Bigg[\frac{1}{G_I(x)}\Bigg]\Bigg|_{x=x_i} \\
&+x_i(1+x_i)\frac{\partial^2}{\partial x^2}\Bigg[\frac{1}{G_I(x)}\Bigg]\Bigg|_{x=x_i}\Bigg\} + P_n'(x_i)\Big[(n_h+n_c-2)x_i+n_h-1\Big]\Bigg[\frac{1}{G_I(x_i)}\Bigg] \\
&- x_i(1+x_i)P_n''(x_i)\Bigg[\frac{1}{G_I(x_i)}\Bigg]\Bigg]\delta_{i\ell} + \Bigg\{\Big[(n_h+n_c)x_i+n_h\Big]\Bigg[\frac{1}{G_I(x_i)}\Bigg] \\
&+ x_i(1+x_i)\frac{\partial}{\partial x}\Bigg[\frac{1}{G_I(x)}\Bigg]\Bigg|_{x=x_i}\Bigg\}\sum_{j=0}^{n} x_i^j\frac{\partial b_j}{\partial x_\ell} \\
&- x_i(1+x_i)\Bigg[\frac{1}{G_I(x_i)}\Bigg]\sum_{j=1}^{n} x_i^{j-1}\frac{\partial b_j}{\partial x_\ell} \quad , \hspace{2cm} (66)
\end{aligned}
$$

where

$$
\delta_{i\ell} = \begin{cases} 0, & i \neq \ell \\ 1, & i = \ell \end{cases} \qquad , \hspace{3cm} (67)
$$

and $\underset{\sim}{b}$ is given by (56). Finally, the terms $\partial b_j/\partial x_\ell$ in (66)
are derived by implicitly differentiating (56) to obtain

$$
\frac{\partial \underset{\sim}{b}}{\partial \underset{\sim}{x}} = \begin{bmatrix} \dfrac{\partial b_0}{\partial x_0} & \dfrac{\partial b_0}{\partial x_1} & \cdots & \dfrac{\partial b_0}{\partial x_n} \\ \vdots & \vdots & & \vdots \\ \dfrac{\partial b_n}{\partial x_0} & \dfrac{\partial b_n}{\partial x_1} & \cdots & \dfrac{\partial b_n}{\partial x_n} \end{bmatrix} = \underline{X}^{-1}\ \text{diag}\Big[\underset{\sim}{R}'(\underset{\sim}{x})-P_n'(\underset{\sim}{b},\underset{\sim}{x})\Big] , \quad (68)
$$

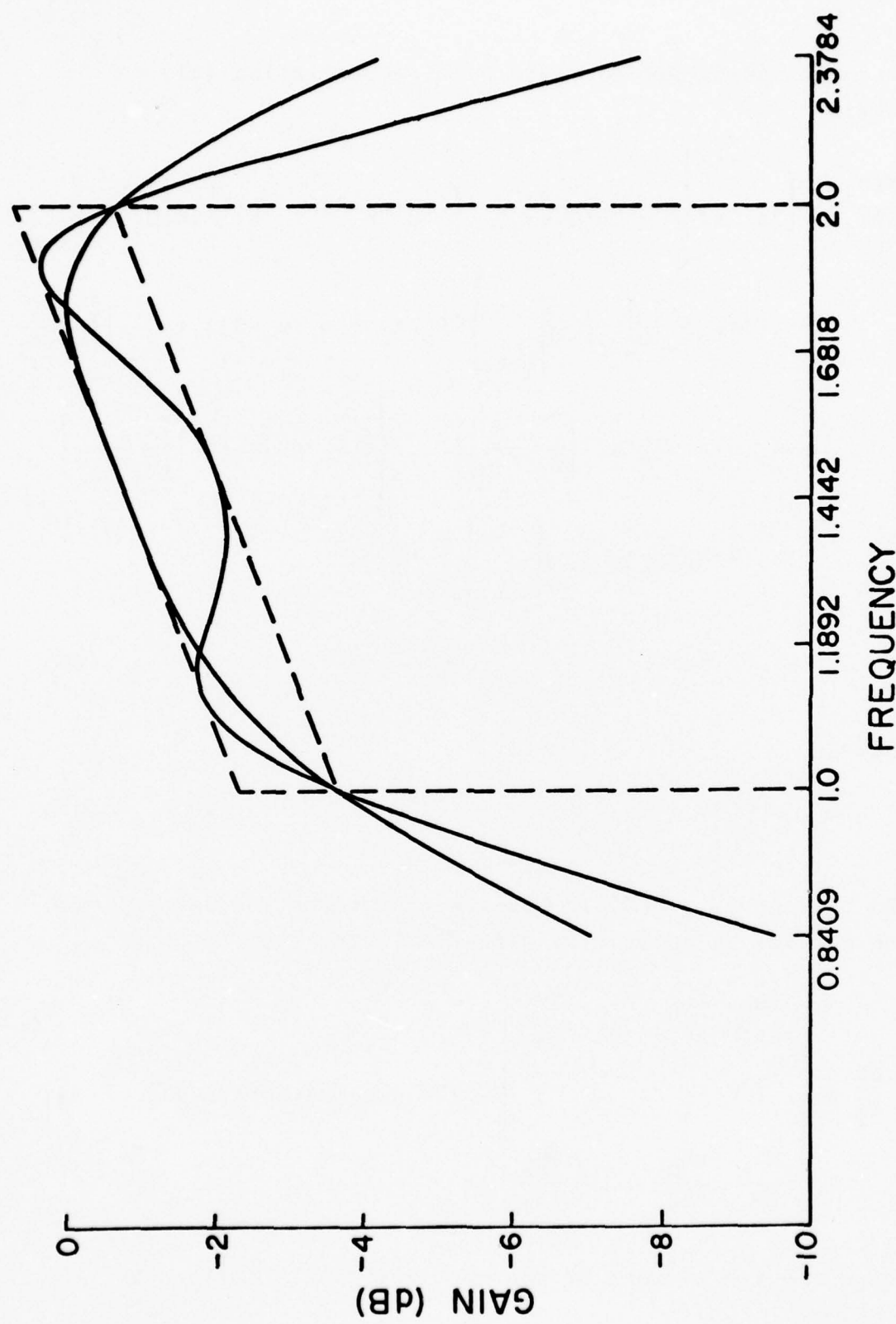where the ith element of the vector $\underset{\sim}{R}'(\underset{\sim}{x})$ is defined by

107

Figure 12. Typical Maximally-Flat and Equiripple Gain Responses for an Octave-Band Tapered-Gain (3dB/octave) Function for n=4, n_j=2, n_h=2, and ϵ=0.6572dB.

108

$$\left[\underset{\sim}{R}'(\underset{\sim}{x})\right]_i = \left.\frac{x^{n_h}(1+x)^{n_c}e^{(-1)^{i+1}\varepsilon}}{G_I(x)}\right|_{x=x_i} . \qquad (69)$$

All the expressions needed to use (62) are now known. Therefore, the transfer function can be obtained for any desired set of parameters n_ℓ, n_h, n_c, S, ε, x_ℓ, x_h, and $\hat{K}$. In the lumped element case, G_I is given by (1) and n_c must be set to zero, while G_I is given by (29) for the distributed case.

Figure 12 shows a typical equiripple gain response corresponding to an octave-band matching network with prescribed gain slope of 3 dB/octave, $n = 4$, $n_\ell = 2$, $n_h = 2$, and a passband ripple of $\pm$ 0.6572 dB. A maximally-flat response with the same set of design parameters is also plotted on Figure 12 for comparison.

References

1. W. H. Ku and W. C. Petersen, "Optimum Gain-Bandwidth Limitations of Transistor Amplifiers as Reactively Constrained Active Two-Port Network," IEEE Trans. on Circuits and Systems, Vol. CAS-22, pp. 523-533, June 1975.

2. R. S. Tucker, "Gain-Bandwidth Limitations of Microwave Transistor Amplifiers," IEEE Trans. on Microwave Theory and Tech., Vol. MTT-21, pp. 322-327, May 1973.

3. O. Pitzalis, Jr. and R. A. Gilson, "Tables of Impedance Matching Networks which approximate prescribed attenuation versus Frequency Slopes," IEEE Trans. on Microwave Theory and Tech., Vol. MTT-19, pp. 381-386, April 1971.

4. D. J. Mellor, "Computer-Aided Synthesis of Matching Networks for Microwave Amplifiers," Stanford Electronics Laboratories Report No. SEL-75-005, March 1975.

5. R. S. Tucker, "Broad-Band Design of Microwave Transistor Amplifiers," Ph.D. Thesis, University of Melbourne, July, 1975.

6. P. I. Richards, "Resistor-Transmission-Line Circuits," Proc. IRE, Vol.36, pp. 217-220, Feb. 1948.

7. H. W. Bode, Network Analysis and Feedback Amplifier Design, New York: Van Norstrand, 1945.

8. R. M. Fano, "Theoretical Limitations on the Broadband Matching of Arbitrary Impedances," J. Franklin Inst., Vol. 249, pp. 57-83, Jan. 1950; pp. 139-155, Feb. 1950.

9. F. F. Kuo and J. F. Kaiser (Eds) System Analysis by Digital Computer, Wiley, 1966.

10. A. Ralston, Mathematical Methods for Digital Computers, John Wiley and Sons, 1966.

OPTIMUM DESIGN OF BROADBAND IMPATT REFLECTION AMPLIFIERS

Jing-Shown Wu, Walter H. Ku[*]

Introduction

The design of broadband microwave IMPATT diode reflection amplifiers is a difficult circuit problem of great practical importance. An optimum broadbanding theory for a class of negative-resistance reflection amplifiers has been derived based on a lumped 5-element frequency-independent equivalent circuit proposed by Gupta[1]. This theory is more general than the presently available design theories and includes some earlier work[2] as special cases. The optimum design theory is applied to the design of broadband IMPATT reflection amplifier using silicon double-drift IMPATT diodes to illustrate the general design techniques.

The lumped equivalent circuits of IMPATT diodes are derived using measured diode characteristics. Based on this equivalent circuit, fundamental integral constraints are derived from which explicit optimum gain-bandwidth limitations are derived for an ideal gain response. The approximation of the ideal gain response with either maximally-flat or equi-ripple responses is solved using both analytical and computer-aided techniques. Finally, the broadband matching networks are synthesized using the realizable gain functions.

Equivalent Circuit of an IMPATT DIODE

The lumped equivalent circuit of an IMPATT diode chip proposed by Gupta is shown in Figure 1. The diode impedance is given by

$$Z_D(p) = r + \frac{-p^2 LCR + p(L-R\hat{R}C) + \hat{R}}{p^2 LC + pC(\hat{R}-R) + 1}$$

$$\frac{p^2 LC(r-R) + p\left[L-C(rR+R\hat{R} - r\hat{R})\right] + (r+\hat{R})}{p^2 LC + pC(\hat{R}-R) + 1} \qquad (1)$$
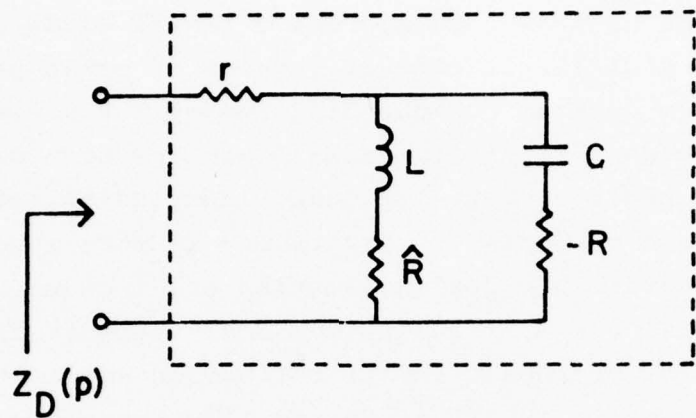
111

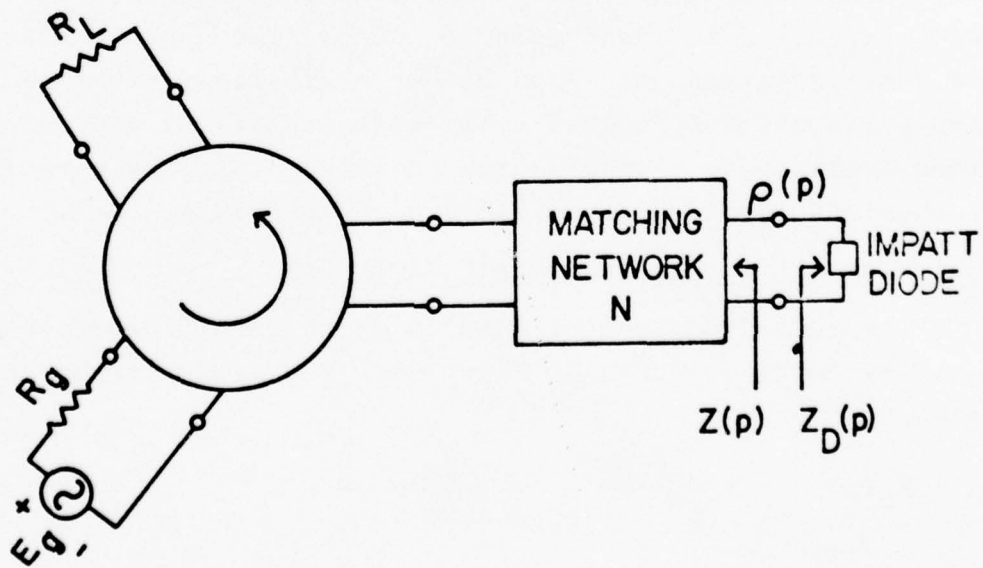Figure 1. Lumped Equivalent Circuit Model of an IMPATT Diode.

Figure 2. Schematic Diagram of a Circulator-Coupled IMPATT
Reflection Amplifier

Writing this expression in terms of

$$Z_D(p) = \frac{a_2 p^2 + a_1 p + a_o}{b_2 p^2 + b_1 p + b_o} \ , \tag{2}$$

we have

$$
\begin{aligned}
a_2 &= LC(r-R), \\
a_1 &= L-C(rR + R\hat{R} - r\hat{R}), \\
a_o &= r + \hat{R}, \\
b_2 &= LC, \\
b_1 &= C(\hat{R}-R), \\
b_o &= 1.
\end{aligned}
\tag{3}
$$

The circulator-coupled reflection amplifier configuration is shown in Figure 2 where the matching network N is assumed to be lossless. The transducer power gain of the reflection amplifier is given by

$$G_t(\omega^2) = |\rho(j\omega)|^2 \ , \tag{4}$$

where

$$\rho(j\omega) = \frac{Z(j\omega) - \overline{Z}_D(j\omega)}{Z(j\omega) + Z_D(j\omega)} \ . \tag{5}$$

In (5), $Z(j\omega)$ is the impedance looking into the matching network and bar denotes complex conjugate. Note that scattering parameters with complex normalization has been used. The analytical continuation of $\rho(j\omega)$ to the entire complex frequency p-plane is given by

$$\rho(p) = \frac{Z(p) - Z_D(-p)}{Z(p) + Z_D(p)} \ . \tag{6}$$

Fundamental Gain-Bandwidth Limitations

Applying the broadband matching theory of Fano[3] and Youla[4], we now derive the fundamental gain-bandwidth limitations for an IMPATT diode reflection amplifier. The even

113

part of the diode impedance from (1) and (2) is given by

$$r_D(p) = \frac{1}{2} \left[Z_D(p) + Z_D(-p) \right]$$

$$= \frac{a_2 b_2 p^4 + (a_2 - a_1 b_1 + a_o b_2) p^2 + a_o}{b_2 p^4 + (2b_2 - b_1^2) p^2 + 1} \,. \tag{7}$$

The zeros of $r_D(p)$ are the zeros of transmission[4,5]. These are given by

$$a_2 b_2 p^4 + (a_2 - a_1 b_1 + a_o b_2) p^2 + a_o = 0, \tag{8}$$

or

$$p_r^2 = \frac{-(a_2 - a_1 b_1 + a_o b_2) \pm \sqrt{(a_2 - a_1 b_1 + a_o b_2)^2 - 4 a_o a_2 b_2}}{2 a_2 b_2} \,. \tag{9}$$

Practical IMPATT diodes exhibit bandpass type of negative-resistance characteristics; i.e.,

$$r > R. \tag{10}$$

From the definitions (3), we see that

$$a_2 > 0, \tag{11}$$

and the two transmission zeros are on the $j\omega$ axis given by

$$\omega_{r_1} = \left[\frac{(a_2 - a_1 b_1 + a_o b_2) - \sqrt{(a_2 - a_1 b_1 + a_o b_2)^2 - 4 a_o a_2 b_2}}{2 \, a_2 b_2} \right]^{1/2}, \tag{12}$$

and

$$\omega_{r_2} = \left[\frac{(a_2 - a_1 b_1 + a_o b_2) + \sqrt{(a_2 - a_1 b_1 + a_o b_2)^2 - 4 a_o a_2 b_2}}{2 \, a_2 b_2} \right]^{1/2}. \tag{13}$$

For the bandpass type of negative resistance characteristic,

114

$$r_D(j\omega) = \text{Re}\left[Z_D(j\omega)\right] \leq 0, \quad \omega_r, \leq \omega \leq \omega_{r_2} \quad . \tag{14}$$

From (6), let p_O be the zero of $\rho(p)$ in the right-half p-plane (RHP),

$$Z(p_O) = Z_D(-p_O) \quad . \tag{15}$$

Since $Z(p)$ is a positive real (PR) function corresponding to a passive 1-port, we have from (15),

$$\left|<Z_D(-p_O)\right| \leq \left| < p_O \right| \quad . \tag{16}$$

Constraints are imposed on $\rho(p)$ by the transmission zeros at ω_{r_1} and ω_{r_2}, the poles of $Z_D(p)$ and $Z_D(-p)$ in the RHP and the stability condition

$$Z(p) + Z_D(p) \neq 0, \tag{17}$$

for Re $p \geq 0$.

Let $\rho_1(p)$ be the all-pass factor which is due to the poles of $Z_D(p)$ or $Z_D(-p)$ in RHP.

$$\rho_1(p) = \frac{b_2 p^2 + b_1 p + 1}{b_2 p^2 - b_1 p + 1} \quad . \tag{18}$$

Let

$$\rho_2(p) = \prod_{k=1}^{N} \frac{p - \lambda_k}{p + \lambda_k} \quad , \tag{19}$$

where

$$\lambda_k = \sigma_k + j\omega_k$$

and $\sigma_k > 0$ and $\left| < Z_D(-\lambda_k)\right| \leq \left| < \lambda_k\right|$ for all k. The λ_k's are the right-half plane zeros of the all-pass factor $\rho_2(p)$, which may be needed to satisfy the reactive constraints simultaneously.

The reflection coefficient $\rho(p)$ can be written as

115

$$\rho(p) = \rho_O(p)\rho_1(p)\rho_2(p), \tag{20}$$

where $\rho_O(p)$ has only LHP poles and zeros.

At the zeros of transmission, ω_{r_1} and ω_{r_2},

$$\rho(j\omega_{ri}) = 1, \quad i = 1, 2. \tag{21}$$

Use (18)-(20), we have[4,5]

$$\ln \rho(p) = \ln\rho_O(p) + \ln\rho_1(p) + \ln\rho_2(p) + j\epsilon\pi, \tag{22}$$

$$\ln\rho_1(j\omega_{ri}) = j \; 2 \; \tan^{-1} \frac{b_1\omega_{ri}}{1 - b_2\omega_{ri}^2} \quad , \tag{23}$$

$$\ln\rho_2(j\omega_{ri}) = j \sum_{k=1}^{N} \tan^{-1} \frac{2\sigma_k\omega_{ri}}{|\lambda_k|^2 - \omega_{ri}^2}, \tag{24}$$

and

$$\ln\rho_O(p) = \frac{2p}{\pi} \int_O^\infty \frac{\ln|\rho_O(p)|}{p^2 + \omega^2} \; d\omega . \tag{25}$$

The integral constraints of the IMPATT diodes are then given by

$$\frac{2\omega_{ri}}{\pi} \int_O^\infty \frac{\ln|\rho_O(j\omega)|}{\omega^2 - \omega_{ri}^2} \; d\omega = -\epsilon\pi - 2\tan^{-1} \frac{b_1\omega_{ri}}{1-b_2\omega_{ri}^2}$$

$$+ \sum_{k=1}^{N} \tan^{-1} \frac{2\sigma_k\omega_{ri}}{|\lambda_k|^2-\omega_{ri}^2} \, . \tag{26}$$

In (22) and (26),, $\epsilon = 0$ or 1. When $\rho_O(0)$ is negative, $\epsilon = 1$ is used.

It can be shown that one RHP zero is necessary to satisfy the two simultaneous constraints presented in (26). Let $\lambda = \sigma$ and $\epsilon = 0$ in (26), we have

$$\frac{2\omega_{r_1}}{\pi} \int_0^\infty \frac{\ln|\rho_o(j\omega)|}{\omega^2 - \omega_{r_1}^2}\, d\omega = -2\tan^{-1}\frac{b_1\omega_{r_1}}{1-b_2\omega_{r_1}^2} + \tan^{-1}\frac{2\sigma\omega_{r_1}}{\sigma^2 - \omega_{r_1}^2} \quad (27)$$

$$\frac{2\omega_{r_2}}{\pi} \int_0^\infty \frac{\ln|\rho_o(j\omega)|}{\omega_{r_2}^2 - \omega^2}\, d\omega = -2\tan^{-1}\frac{b_1\omega_{r_2}}{b_2\omega_{r_2}^2 - 1} - \tan^{-1}\frac{2\sigma\omega_{r_2}}{\sigma^2 - \omega_{r_2}^2}. \quad (28)$$

The integral constraints (27) and (28) contain the gain-bandwidth limitations for an IMPATT diode reflection amplifier based on the lumped 5-element equivalent circuit.

Consider the ideal gain response shown in Figure 3 defined by

$$\ln|\rho(j\omega)| = H, \qquad \omega_{c_1} < \omega < \omega_{c_2},$$
$$= 0, \qquad \text{elsewhere.} \quad (29)$$

The integral constraints (27) and (28) can be evaluated to give the explicit optimum gain-bandwidth relationships as follows:

$$\frac{H}{\pi}\ln\frac{(\omega_{c_1}+\omega_{r_1})(\omega_{c_2}-\omega_{r_1})}{(\omega_{c_1}-\omega_{r_1})(\omega_{c_2}+\omega_{r_1})} = -2\tan^{-1}\frac{b_1\omega_{r_1}}{1-b_2\omega_{r_1}^2} + \tan^{-1}\frac{2\sigma\omega_{r_1}}{\sigma^2 - \omega_{r_1}^2} \quad (30)$$

$$\frac{H}{\pi}\ln\frac{(\omega_{r_2}-\omega_{c_1})(\omega_{c_2}+\omega_{r_2})}{(\omega_{c_1}+\omega_{r_2})(\omega_{r_2}-\omega_{c_2})} = -2\tan^{-1}\frac{b_1\omega_{r_2}}{b_2\omega_{r_2}^2 - 1} - \tan^{-1}\frac{2\sigma\omega_{r_2}}{\sigma^2 - \omega_{r_2}^2}. \quad (31)$$

Realizable Gain Functions

Realizable gain functions for an IMPATT reflection amplifier must satisfy the following conditions

(i) $G_t(\omega^2) \geq 1$, $\omega_{r_1} \leq \omega \leq \omega_{r_2}$,
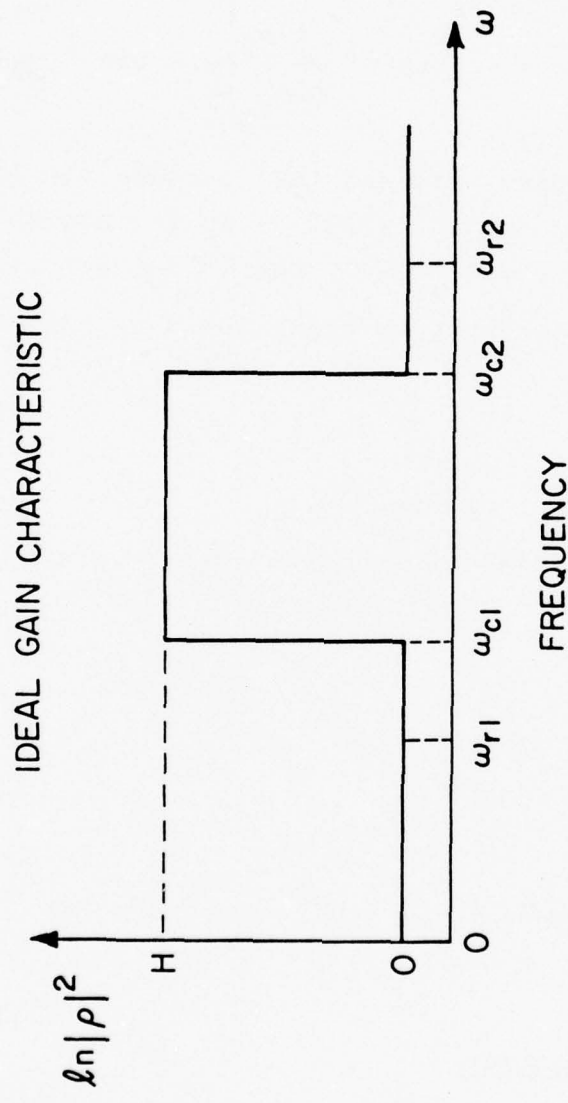< 1, elsewhere ;

Figure 3. Ideal Gain Response of an IMPATT Reflection Amplifier.

(ii) $G_t(\omega^2) = 1$,   at $\omega = \omega_{r_1}$ and $\omega = \omega_{r_2}$;

(iii) Integral Restrictions (30) and (31).

(iv) $|<Z_D(-p_o)| \leq |<p_o|$, where p_o is the zero
of the reflection coefficient $\rho(p)$ in RHP;
i.e., Re $p_o > 0$.

We now consider classes of realizable gain functions
with maximally-flat and equiripple magnitude characteristics.
A typical gain function can be written as

$$G_t(\omega^2) = |\rho(j\omega)|^2 = 1 + \cfrac{K}{\cfrac{(\omega^2+\alpha^2)P_n(\omega^2)}{\omega^{2m}(\omega^2-\omega_{r_1}^2)(\omega_{r_2}^2-\omega^2)} - K} \quad , \qquad (32)$$

where α is the required RHP zero, ω_{r_1} and ω_{r_2} are the
transmission zeros of $G_t(\omega^2)$, and $P_n(\omega^2)$ is an nth order
polynomial of ω^2.

Maximally-Flat Amplifier Response

For the maximally-flat amplitude characteristic, the
polynomial $P_n(\omega^2)$ in (32) is solved analytically to obtain
a maximally-flat approximation at a prescribed band center
frequency. Let $x = \omega^2$, (32) becomes

$$G_t(x) = 1 + \cfrac{K}{\cfrac{(x+\sigma)\ P_n(x)}{x^m(x-x_1)(x_2-x)} - K} \quad , \qquad (33)$$

where

$$\sigma = \omega^2,$$
$$x_1 = \omega_{r_1}^2 ,$$
$$x_2 = \omega_{r_2}^2 .$$

Define the (n+1)th order polynomial.

$$q_{n+1}(x) = (x+\sigma)P_n(x) - (K+1)x^m(x-x_1)(x_2-x). \tag{34}$$

It can be represented by its Taylor series expansion about the band center frequency $x_o = \omega_o^2$ as

$$q_{n+1}(x) = \alpha_o + \alpha_1(x-x_o) + \alpha_2(x-x_o)^2 + \ldots + \alpha_{n-1}(x-x_o)^{n-1} \tag{35}$$
$$+ \alpha_n(x-x_o)^n + \alpha_{n+1}(x-x_o)^{n+1} \ .$$

The criteria for maximally flat error can be expressed in terms of the Taylor series coefficient as

$$\alpha_i = 0, \quad i = 0, 1, \ldots, n-1 \ . \tag{36}$$

Thus (35) becomes

$$q_{n+1}(x) = \alpha_n(x-x_o)^n + \alpha_{n+1}(x-x_o)^{n+1} \ , \tag{37}$$

The coefficients α_n and α_{n+1} can be used to control the bandwidth of the approximation as well as to satisfy the constraint imposed by the form of (34). From the definition (34),

$$(x+\sigma)P_n(x) = q_{n+1}(x) + (K+1)x^m(x-x_1)(x_2-x) \ . \tag{38}$$

The right-hand side of (38) must have a factor $(x+\sigma)$. Therefore,

$$q_{n+1}(-\sigma) + (K+1)(-\sigma)^m(-\sigma - x_1)(x_2+\sigma) = 0. \tag{39}$$

Invoking (37), (39) becomes

$$\alpha_n(\sigma+x_o)^n - \sigma_{n+1}(+x_o)^{n+1} - (-1)^{m-n}(K+1)\sigma^m(\sigma+x_1)(x_2+\sigma) = 0, \tag{40}$$

or

$$\alpha_n = \alpha_{n+1}(\sigma+x_o) + \frac{(-1)^{m-n}(K+1)\sigma^m(\sigma+x_1)(x_2+\sigma)}{(\sigma+x_o)^n} \ . \tag{41}$$

120

Finally, (37) can be written as

$$q_{n+1}(x) = \{\alpha_{n+1}(\sigma+x_o) + \frac{(-1)^{m-n}(K+1)\sigma^m(\sigma+x_1)(\sigma+x_2)}{(\sigma+x_o)^n}\}$$

$$(x-x_o)^n + \alpha_{n+1}(x-x_o)^{n+1} . \qquad (42)$$

In (42), x_1 and x_2 are known parameters given by the trans-
mission zeros, σ is the required RHP zero to satisfy the
integral constraints, and only α_{n+1} is used as a bandwidth
parameter. This technique can be generalized to cases
where more than one RHP zero are required.

Equiripple Amplifier Response

From the general gain function given by (32), the
equiripple amplitude characteristic can be expressed in
terms of

$$\frac{(\omega^2 + \alpha^2)P_n(\omega^2)}{\omega^{2m}(\omega^2-\omega_{r_1}^2)(\omega_{r_2}^2-\omega^2)} = K + 1 + \varepsilon, \ \omega_{c_1} \leq \omega \leq \omega_{c_2} . \qquad (43)$$

The nth order polynomial $P_n(\omega^2)$ will be chosen for an equi-
ripple approximation within the prescribed passband from
ω_{c_1} to ω_{c_2} with a ripple of ε. This approximation problem
has been solved by using the numerical technique developed
by Petersen for broadband transistor amplifier design[6].
This will be illustrated later for some specific reflection
amplifier designs.

In this section, an approximate but analytical method
will be presented. In general,

$$\alpha << \omega_{c_2} , \qquad (44)$$

and we can use the approximation that

$$\frac{(\omega^2+\alpha^2)P_n(\omega^2)}{\omega^{2m}(\omega^2-\omega_{r_1}^2)(\omega_{r_2}^2-\omega^2)} \cong \frac{P_n(\omega^2)}{\omega^{2(m-1)}(\omega^2-\omega_{r_1}^2)(\omega_{r_2}^2-\omega^2)} \qquad (45)$$

for $\omega_{c_1} < \omega < \omega_{c_2}$ and $m > 1$. For an equiripple error

121

characteristic, the rational function

$$C(\omega)^2 = \frac{P_n(\omega^2)-(K+1)\omega^{2(m-1)}(\omega^2-\omega_{r1}^2)(\omega_{r2}^2-\omega^2)}{\omega^{2(m-1)}(\omega^2-\omega_{r1}^2)(\omega_{r2}^2-\omega^2)} \qquad (46)$$

must be equiripple over the interval $\omega_{c1}<\omega<\omega_{c2}$ with ripples of magnitude $\pm\,\varepsilon$ around zero.

Consider the transformation

$$\omega^2 = \frac{\omega_{c2}^2+\omega_{c1}^2}{2} + \frac{\omega_{c2}^2-\omega_{c1}^2}{2}\,y \quad , \qquad (47)$$

$$y = \cos\,\phi\,,$$

which maps the interval $(\omega_{c_1},\;\omega_{c_2})$ into $(-1,1)$ in y-axis. Substitution of (47) into (46) yields

$$C(y) = \frac{q_n(y)}{(y-\alpha_1)^{m-1}(y-\alpha_2)(y-\alpha_3)} \quad . \qquad (49)$$

where $q_n(y)$ is an nth order polynomial in y defined by

$$q_n(y) = -P_n(\frac{\omega_{c2}^2+\omega_{c1}^2}{2} + \frac{\omega_{c2}^2-\omega_{c1}^2}{2}\,y)(\frac{2}{\omega_{c2}^2-\omega_{c1}^2})^{m+1}$$

$$+(k+1)(y-\alpha_1)^{m-1}(y-\alpha_2)(y-\alpha_3). \qquad (50)$$

$$\alpha_1 = -\frac{\dfrac{\omega_{c2}^2+\omega_{c1}^2}{2}}{\dfrac{\omega_{c2}^2-\omega_{c1}^2}{2}} < -1 \quad . \qquad (51)$$

$$\alpha_2 = -\frac{\dfrac{\omega_{c2}^2+\omega_{c1}^2-2\omega_{r1}^2}{2}}{\dfrac{\omega_{c2}^2-\omega_{c1}^2}{2}} < -1 \quad . \qquad (52)$$

122

$$\alpha_3 = \frac{2\omega_{r2}^2 - \omega_{c2}^2 - \omega_{c1}^2}{\omega_{c2}^2 - \omega_{c1}^2} > 1 \quad , \tag{53}$$

The approximation problem is now to construct a rational function $C(y)$ in (49) with prescribed poles at $y = \alpha_1$ (of the order m-1), $y = \alpha_2$, and $y = \alpha_3$ to have an equiripple error in the transformed interval of $-1 \leq y \leq 1$.

The analytical solution to this problem is obtained using the method introduced by Sharpe.[7] Consider first the following function

$$C_1(y) = \cos\left((n-m-1)\phi + (m-1)\delta_1 + \delta_2 + \delta_3\right), \tag{54}$$

with

$$\cos \phi = y.$$

In (54), the δ_i's (i = 1,2,3) will be defined such that $C_1(y)$ will be a rational function with the desired equiripple error characteristic and the prescribed poles at $y = \alpha_1$, α_2, α_3. For this purpose, $\delta_i(y)$ must not only introduce the poles but also must vary monotonically from zero to π in the interval $-1 \leq y \leq 1$. If the δ_i's have these prescribed properties, then the argument of (54) will vary over the range $0 \leq (n-m-1)\phi + (m-1)\delta_1 + \delta_2 + \delta_3 < n\pi$.

The suitable definition of δ_i is given by

$$\cos \delta_i = \frac{1 - \alpha_i y}{y - \alpha_i} \quad , \quad i = 1,2,3 \quad . \tag{55}$$

Corresponding to (55), we have

$$\sin \delta_i = \text{sgn}(-\alpha_i) \frac{(\alpha_i^2 - 1)(1 - y^2)}{y - \alpha_i} \quad . \tag{56}$$

123

The definitions contained in (55) and (56) guarantee that $\cos \delta_i$ changes monotonically between -1 and $+1$ over the interval $0 \leq \delta < \pi$ or $-1 \leq y \leq 1$. The factor $(y - \alpha_i)$ in $\cos \delta_i$ is the required pole in $C_1(y)$. This can be verified by substituting (55) in (54) to obtain

$$C_1(y) = \cos((n-m-1)\phi(m-1)\delta_1 + \delta_2 + \delta_3)$$

$$= \frac{1}{2}\left[e^{j((n-m-1)\phi + (m-1)\delta_1 + \delta_2 + \delta_3)} + \text{conjugate}\right]$$

$$= \frac{1}{2(y-\alpha_1)^{m-1}(y-\alpha_2)(y-\alpha_3)}\left[(y + \sqrt{y^2-1})^{n-m-1}(1 + \alpha_1 y + \right.$$

$$\sqrt{(\alpha_1^2-1)(y^2-1)}\ ^{m-1}\ )$$

$$(1 - \alpha_2 y \sqrt{(\alpha_2^2-1)(y^2-1)}\ )(1 - \alpha_3 y - \sqrt{(\alpha_3^2-1)(y^2-1)}\ )$$

$$+ (y - \sqrt{y^2-1})^{n-m-1}\ (1 - \alpha, \ y - \sqrt{(\alpha_1^2-1)(y^2-1)})^{m-1}$$

$$\left. (1 - \alpha_2 y - \sqrt{(\alpha^2-1)(y^2-1)}(1 - \alpha_3 y + \sqrt{(\alpha_3^2-1)(y^2-1)}\ )\right]. \quad (57)$$

The rational function $C_1(y)$ given in (54) and (57) oscillates between ± 1 in the interval $-1 \leq y \leq 1$ and (57) clearly shows the prescribed poles at α_1, α_2, α_3 with order $m-1$, 1, and 1 respectively. Using this result, the desired rational function $C(\omega^2)$ in (46) is given by

$$C(\omega^2) = \varepsilon\ C_1\ \left(\frac{2\omega^2}{\omega_{c2}^2 \omega_{c1}^2} - \frac{\omega_{c2}^2 + \omega_{c1}^2}{\omega_{c2}^2 - \omega_{c1}^2}\right), \quad (58)$$

where ε is the magnitude of the ripple in the passband from ω_{c1} to ω_{c2}. It should be mentioned that the same result can be obtained by using the method presented by Darlington.[8]

The numerator of $c_1(y)$, i.e., $g_n(y)$, can be obtained from (57). For example, the approximation function $C_1(y)$ of a double-tuned amplifier (n=4, m=2) is given by

$$C_1(y) = \frac{d_0 + d_1 y + d_2 y^2 + d_3 y^3 + d_4 y^4}{(y-\alpha_1)(y-\alpha_2)(y-\alpha_3)} \quad , \tag{59}$$

where

$$d_0 = \alpha_1 \alpha_2 \alpha_3 - \alpha_1 \sqrt{(\alpha_2^2-1)(\alpha_3^2-1)} - \alpha_2 \sqrt{(\alpha_3^2-1)(\alpha_1^2-1)} + \alpha_3 \sqrt{(\alpha_1^2-1)(\alpha_2^2-1)} \tag{60}$$

$$d_1 = 1 + \sqrt{(\alpha_2^2-1)(\alpha_3^2-1)} - \sqrt{(\alpha_1^2-1)(\alpha_2^2-1)} + \sqrt{(\alpha_1^2-1)(\alpha_3^2-1)} - \alpha_2 \sqrt{\alpha_3^2-1}$$

$$+ \alpha_3 \sqrt{\alpha_2^2-1} + \alpha_1 \sqrt{\alpha_2^2-1} - \alpha_1 \sqrt{\alpha_3^2-1} + \alpha_2 \sqrt{\alpha_1^2-1} + \alpha_3 \sqrt{\alpha_1^2-1} \quad . \tag{61}$$

$$d_2 = -\alpha_1 - \alpha_2 - \alpha_3 - \alpha_1 \sqrt{(\alpha_2^2-1)(\alpha_3^2-1)} - \alpha_2 \sqrt{(\alpha_1^2-1)(\alpha_3^2-1)} + \alpha_3 \sqrt{(\alpha_1^2-1)(\alpha_2^2-1)}$$

$$+ \sqrt{\alpha_1^2-1} + \sqrt{\alpha_2^2-1} - \sqrt{\alpha_3^2-1} + \sqrt{(\alpha_1^2-1)(\alpha_2^2-1)(\alpha_3^2-1)} - \alpha_2 \sqrt{\alpha_3^2-1} + \alpha_3 \sqrt{\alpha_2^2-1}$$

$$+ \alpha_1 \sqrt{\alpha_2^2-1} - \alpha_1 \sqrt{\alpha_3^2-1} + \alpha_2 \sqrt{\alpha_1^2-1} + \alpha_3 \sqrt{\alpha_1^2-1} \quad . \tag{62}$$

$$d_3 = \alpha_2 \alpha_3 + \alpha_1 \alpha_2 + \alpha_3 \alpha_1 - \sqrt{(\alpha_1^2-1)(\alpha_3^2-1)} + \sqrt{(\alpha_1^2-1)(\alpha_2^2-1)} - \sqrt{(\alpha_1^2-1)(\alpha_3^2-1)}$$

$$+ \alpha_2 \sqrt{\alpha_3^2-1} - \alpha_3 \sqrt{\alpha_2^2-1} - \alpha_1 \sqrt{\alpha_2^2-1} + \alpha_1 \sqrt{\alpha_3^2-1} - \alpha_2 \sqrt{\alpha_1^2-1} - \alpha_3 \sqrt{\alpha_1^2-1} \quad . \tag{63}$$

$$d_4 = -\alpha_1 \alpha_2 \alpha_3 + \alpha_1 \sqrt{(\alpha_2^2-1)(\alpha_3^2-1)} + \alpha_2 \sqrt{\alpha_2^2-1)(\alpha_3^2-1)} - \alpha_3 \sqrt{(\alpha_1^2-1)(\alpha_2^2-1)}$$

$$+ \alpha_2 \alpha_3 \sqrt{\alpha_1^2-1} - \alpha_1 \alpha_2 \sqrt{\alpha_3^2-1} + \alpha_1 \alpha_3 \sqrt{\alpha_2^2-1} \sqrt{(\alpha_1^2-1)(\alpha_2^2-1)(\alpha_3^2-1)} \quad . \tag{64}$$

Similarly, for a triple-tuned amplifier (n=6, m=3), $C_1(y)$ is given by

$$C_1(y) = \frac{d'_0 + d'_1 y + d'_2 y^2 + d'_3 y^3 + d'_6 y^4 + d'_5 y^5 + d'_6 y^6}{(y-\alpha_1)^2 (y-\alpha_2)(y-\alpha_3)} \quad , \tag{65}$$

where

$$d'_0 = -d_0 \sqrt{\alpha_1^2 - 1} - \sqrt{(\alpha_1^2-1)(\alpha_2^2-1)(\alpha_3^2-1)} - \alpha_1 \alpha_2 \sqrt{\alpha_3^2 - 1} + \alpha_2 \alpha_3 \sqrt{\alpha_1^2 - 1} \quad ,$$

$$+ \alpha_1 \alpha_3 \sqrt{\alpha_2^2 - 1} \tag{66}$$

$$d'_1 = -d_1 \sqrt{\alpha_1^2 - 1} + d_0 - \sqrt{\alpha_1^2 - 1} - \sqrt{\alpha_2^2 - 1} + \sqrt{\alpha_3^2 - 1} - \sqrt{(\alpha_1^2-1)(\alpha_2^2-1)(\alpha_3^2-1)}$$

$$- \alpha_1 - \alpha_2 - \alpha_3 - \alpha_1 \sqrt{(\alpha_2^2-1)(\alpha_3^2-1)} - \alpha_2 \sqrt{(\alpha_1^2-1)(\alpha_3^2-1)} + \alpha_3 \sqrt{(\alpha_1^2-1)(\alpha_2^2-1)}$$

$$+ (\alpha_1 - \sqrt{\alpha_1^2 - 1}) \sqrt{(\alpha_1^2-1)(\alpha_2^2-1)(\alpha_3^2-1)} + \alpha_1 \alpha_2 \sqrt{\alpha_3^2 - 1} - \alpha_2 \alpha_3 \sqrt{\alpha_1^2 - 1}$$

$$- \alpha_1 \alpha_3 \sqrt{\alpha_2^2 - 1}) \quad , \tag{67}$$

$$d'_2 = -d_2 \sqrt{\alpha_1^2 - 1} + d_1 - d_0 (\alpha_1 - \sqrt{\alpha_1^2 - 1}) + \sqrt{(\alpha_1^2-1)(\alpha_2^2-1)(\alpha_3^2-1)} + \alpha_1 \alpha_2 \sqrt{\alpha_3^2 - 1}$$

$$- \alpha_2 \alpha_3 \sqrt{\alpha_1^2 - 1} - \alpha_1 \alpha_3 \sqrt{\alpha_2^2 - 1} - \alpha_2 \sqrt{\alpha_3^2 - 1} + \alpha_3 \sqrt{\alpha_2^2 - 1} + \alpha_1 \sqrt{\alpha_2^2 - 1} - \alpha_1 \sqrt{\alpha_3^2 - 1}$$

$$+ \alpha_2 \sqrt{\alpha_1^2 - 1} + \alpha_3 \sqrt{\alpha_1^2 - 1} + \alpha_1 \alpha_2 + \alpha_2 \alpha_3 + \alpha_3 \alpha_1 - \sqrt{(\alpha_1^2-1)(\alpha_3^2-1)}$$

$$+ \sqrt{(\alpha_1^2-1)(\alpha_2^2-1)} - \sqrt{(\alpha_1^2-1)(\alpha_3^2-1)} + \alpha_1 - \alpha_1^2 - 1)(\sqrt{\alpha_1^2 - 1} + \sqrt{\alpha_2^2 - 1}$$

$$- \sqrt{\alpha_3^2 - 1} + \alpha_1 + \alpha_2 + \alpha_3 + \sqrt{(\alpha_1^2-1)(\alpha_2^2-1)(\alpha_3^2-1)} + \alpha_1 \sqrt{(\alpha_2^2-1)(\alpha_3^2-1)}$$

$$+ \alpha_2 \sqrt{(\alpha_1^2-1)(\alpha_3^2-1)} - \alpha_3 \sqrt{(\alpha_1^2-1)(\alpha_2^2-1)} \quad , \tag{68}$$

126

$$d_3' = -\alpha_3\sqrt{\alpha_1^2-1}+\alpha_2-(\alpha_1-\sqrt{\alpha_1^2-1})\alpha_1+\sqrt{\alpha_1^2-1}+\sqrt{\alpha_2^2-1}+\sqrt{\alpha_3^2-1}$$

$$+\alpha_1+\alpha_2+\alpha_3+2\sqrt{(\alpha_1^2-1)(\alpha_2^2-1)(\alpha_3^2-1)}+2\alpha_1\sqrt{(\alpha_2^2-1)(\alpha_3^2-1)}$$

$$+2\alpha_2\sqrt{(\alpha_1^2-1)(\alpha_3^2-1)}-2\alpha_3\sqrt{(\alpha_1^2-1)(\alpha_2^2-1)}-(\alpha_1-\sqrt{\alpha_1^2-1})$$

$$\left[\sqrt{(\alpha_1^2-1)(\alpha_2^2-1)(\alpha_3^2-1)}+\alpha_1\alpha_2\sqrt{\alpha_3^2-1}-\alpha_2\alpha_3\sqrt{\alpha_1^2-1}\right.$$

$$\left.-\alpha_1\alpha_3\sqrt{\alpha_2^2-1}\right]-\alpha_2\alpha_3\sqrt{\alpha_1^2-1}+\alpha_1\alpha_2\sqrt{\alpha_3^2-1}-\alpha_1\alpha_3\sqrt{\alpha_2^2-1}$$

$$-\alpha_1\alpha_2\alpha_3+(\alpha_1-\sqrt{\alpha_1^2-1})\left[\alpha_2\sqrt{\alpha_3^2-1}-\alpha_3\sqrt{\alpha_2^2-1}-\alpha_1\sqrt{\alpha_2^2-1}\right.$$

$$+\alpha_1\sqrt{\alpha_3^2-1}-\alpha_2\sqrt{\alpha_1^2-1}-\alpha_3\sqrt{\alpha_1^2-1}-\alpha_2\alpha_3-\alpha_3\alpha_1-\alpha_1\alpha_2$$

$$+\sqrt{(\alpha_1^2-1)(\alpha_3^2-1)}-\sqrt{(\alpha_1^2-1)(\alpha_2^2-1)}+\sqrt{(\alpha_3^2-1)(\alpha_1^2-1)}\bigg] \quad , \qquad (69)$$

$$d_4' = -_4\sqrt{\alpha_1^2-1}+d_3-d_2(\alpha_1-\sqrt{\alpha_1^2-1})+\alpha_2\sqrt{\alpha_3^2-1}+\alpha_3\sqrt{\alpha_2^2-1}-\alpha_1\sqrt{\alpha_2^2-1}$$

$$+\alpha_1\sqrt{\alpha_3^2-1}-\alpha_2\sqrt{\alpha_1^2-1}-\alpha_3\sqrt{\alpha_1^2-1}-\alpha_2\alpha_3-\alpha_1\alpha_2-\alpha_3\alpha_1+\sqrt{(\alpha_1^2-1)(\alpha_3^2-1)}$$

$$-\sqrt{(\alpha_1^2-1)(\alpha_2^2-1)}+\sqrt{(\alpha_1^2-1)(\alpha_3^2-1)}-(\alpha_1-\sqrt{\alpha_1^2-1})\left[\alpha_1+\alpha_2+\alpha_3+\sqrt{\alpha_1^2-1}\right.$$

$$+\sqrt{\alpha_2^2-1}-\sqrt{\alpha_3^2-1}+2\sqrt{(\alpha_1^2-1)(\alpha_2^2-1)(\alpha_3^2-1)}+2\alpha_1\sqrt{(\alpha_2^2-1)(\alpha_3^2-1)}$$

$$+2\alpha_2\sqrt{(\alpha_1^2-1)(\alpha_3^2-1)}-2\alpha_3\sqrt{(\alpha_1^2-1)(\alpha_2^2-1)}-\alpha_2\alpha_3\sqrt{\alpha_1^2-1}+\alpha_1\alpha_2\sqrt{\alpha_3^2-1}$$

$$-\alpha_1\alpha_3\sqrt{\alpha_2^2-1}-\alpha_1\alpha_2\alpha_3\bigg], \qquad (70)$$

$$d_5' = d_4-(\alpha_1-\sqrt{\alpha_1^2-1})d_3+\alpha_2\alpha_3\sqrt{\alpha_1^2-1}-\sqrt{(\alpha_1^2-1)(\alpha_2^2-1)(\alpha_3^2-1)}$$

$$-\alpha_1\alpha_2\sqrt{\alpha_3^2-1}+\alpha_1\alpha_3\sqrt{\alpha_2^2-1}+\alpha_1\alpha_2\alpha_3-\alpha_1\sqrt{(\alpha_2^2-1)(\alpha_3^2-1)}-\alpha_2\sqrt{(\alpha_1^2-1)}$$

$$\sqrt{(\alpha_3^2-1)}+\alpha_3\sqrt{(\alpha_1^2-1)(\alpha_2^2-1)}-(\alpha_1-\sqrt{\alpha_1^2-1})\left[\alpha_2\sqrt{\alpha_3^2-1}\right.$$

$$-\alpha_3\sqrt{\alpha_2^2-1}-\alpha_1\sqrt{\alpha_2^2-1}+\alpha_1\sqrt{\alpha_3^2-1}-\alpha_2\sqrt{\alpha_1^2-1}-\alpha_3\sqrt{\alpha_1^2-1}$$

$$-\alpha_2\alpha_3+\sqrt{(\alpha_1^2-1)(\alpha_3^2-1)}-\alpha_1\alpha_2-\alpha_1\alpha_3-\sqrt{(\alpha_1^2-1)(\alpha_2^2-1)}\bigg] \quad (71)$$

$$+\sqrt{(\alpha_1^2-1)(\alpha_3^2-1)})\,,$$

$$d_6' = -(\alpha_1\sqrt{\alpha_1^2-1})d_4 - (\alpha_1\sqrt{\alpha_1^2-1})(\alpha_2\alpha_3\sqrt{\alpha_1^2-1} - \sqrt{(\alpha_1^2-1)(\alpha_2^2-1)(\alpha_3^2-1)}$$

$$-\alpha_1\alpha_2\sqrt{\alpha_3^2-1} + \alpha_1\alpha_3\sqrt{\alpha_2^2-1} + \alpha_1\alpha_2\alpha_3 - \alpha_1\sqrt{(\alpha_2^2-1)(\alpha_3^2-1)} -$$

$$- \alpha_2\sqrt{(\alpha_1^2-1)(\alpha_3^2-1)} + \alpha_3\sqrt{(\alpha_1^2-1)(\alpha_2^2-1)} \quad . \tag{72}$$

Amplifier Design Procedure and Example

The exact design procedure of an IMPATT reflection amplifier can be briefly outlined as follows:

1. Model the IMPATT diode by the 5-element equivalent circuit based on the measured data. Derive the integral constraints. Once the model of the diode is known, the ideal gain-bandwidth limitations may be checked to determine the approximation gain of the matching network and the necessary RHP zero α for the specified bandwidth.

2. Determine the order of the amplifier, the distribution of high pass and low pass elements, the bandwidth, and the ripple parameter ϵ.

3. Given the initial guess of the amplifier gain K and the RHP zero α, find the approximation function $|\rho(j\omega)|^2$ with prescribed equiripple or maximally-flat property by either the analytic approximation or the computer program.

4. Substitute the approximation function into the two integral constraints. Use the computer to evaluate the integral constraints numerically and obtain a new set of gain k and the location of the RHP zero α.

5. Repeat Step 3 and 4 until the errors of the two integrations are less than some specified bound.

6. Factorize $|\rho(j\omega)|^2$ to obtain $\rho(p)$. From $\rho(p)$, calculate $Z(p)$ by using (6). The constraints on $\rho(p)$ guarantee the realizability of $Z(p)$. Synthesize the lossless 2-port network N.

7. If the variation of the gain response of the amplifier with actual measured data is too large, use the optimization program to minimize the gain variation.

Based on data provided by the HP Application Notes, the admittance of the HP double drift silicon IMPATT diode #5082-0610 and the admittance of its equivalent circuit model have been plotted in Figure 4.

The element values of the model of the HP double-drift diode is given by

$$r = 0.9509\Omega\ , \qquad L = 0.9351\ nH, \qquad \hat{R} = 9.983\Omega,$$

$$C = 0.4926pF, \qquad R = 6.843\Omega\ ,$$

$$Z_D(p) = \frac{0.1228039 \times 10^{-20}p^2 + 0.9161568 \times 10^{-9}p + 19.492}{0.4606303 \times 10^{-21}p^2 + 0.1546764 \times 10^{-11}p + 1}\ , \qquad (73)$$

$$\omega_{r1} = 2\pi \times (8.238940\ GHz)\ , \qquad (74)$$

$$\omega_{r2} = 2\pi \times (18.047381\ GHz)\ . \qquad (75)$$

Design Example 1

Consider the design of a double-tuned IMPATT reflection amplifier over the 12-14 GHz frequency band with 1 dB ripple. The ripple parameter ε can be calculated from (32), (43) to
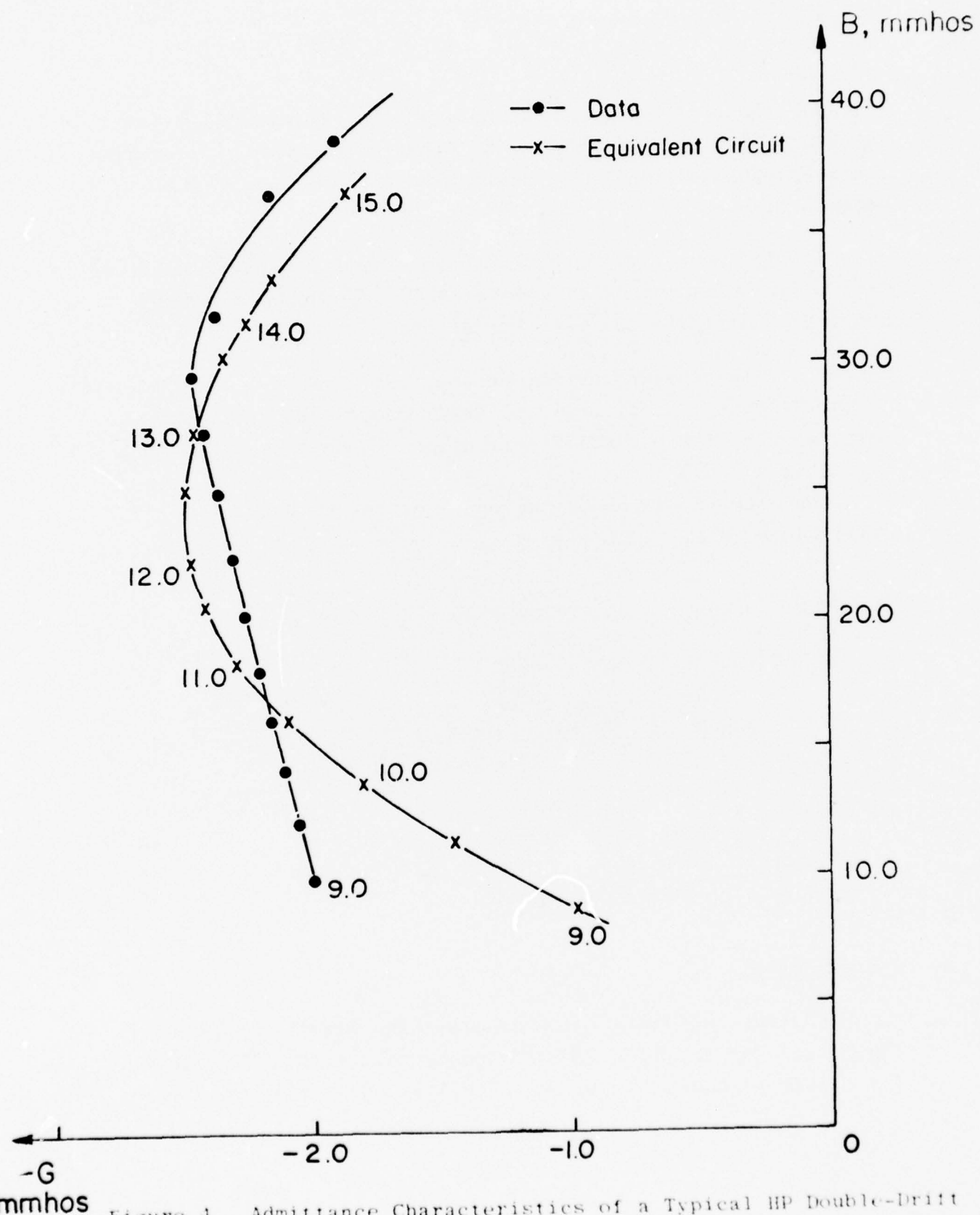
Figure 4. Admittance Characteristics of a Typical HP Double-Drift Silicon IMPATT Diode (HP 5082-0610)

130

be $\epsilon = 0.142$. The optimal gain-bandwidth limitations for different center frequencies are plotted in Figures 5 and 6. The RHP zero α for the optimal design is shown in Figure 7.

In order to use the computer program, we have to normalize the impedance of the diode to 14 GHz. Rewrite $Z_D(p)$ as

$$Z_D(p) = \frac{9.502287p^2 + 80.58935p + 19.4920}{3.56425p^2 + 0.13606p + 1.0} \tag{76}$$

The normalized transmission zeros are calculated to be

$$\omega_{r1} = 0.588496 \quad , \tag{77}$$

$$\omega_{r2} = 1.289099 \quad . \tag{78}$$

Let $x = \omega^2$, the normalized gain function is given by

$$G(x) = 1 + \frac{K}{\dfrac{(x + \alpha^2)P_4(x)}{x^2(x - x_1)(x_2 - x)} - K} \tag{79}$$

where $x_1 = \omega_{r1}^2$, $x_2 = \omega_{r2}^2$.

The normalized passband are specified by

$$\omega_{c1} = 0.8571428, \qquad \omega_{c2} = 1.0. \tag{80}$$

Using Petersen's program[6], the approximation polynomial $P_4(x)$, the gain constant K, and the normalized RHP zero α are given respectively by
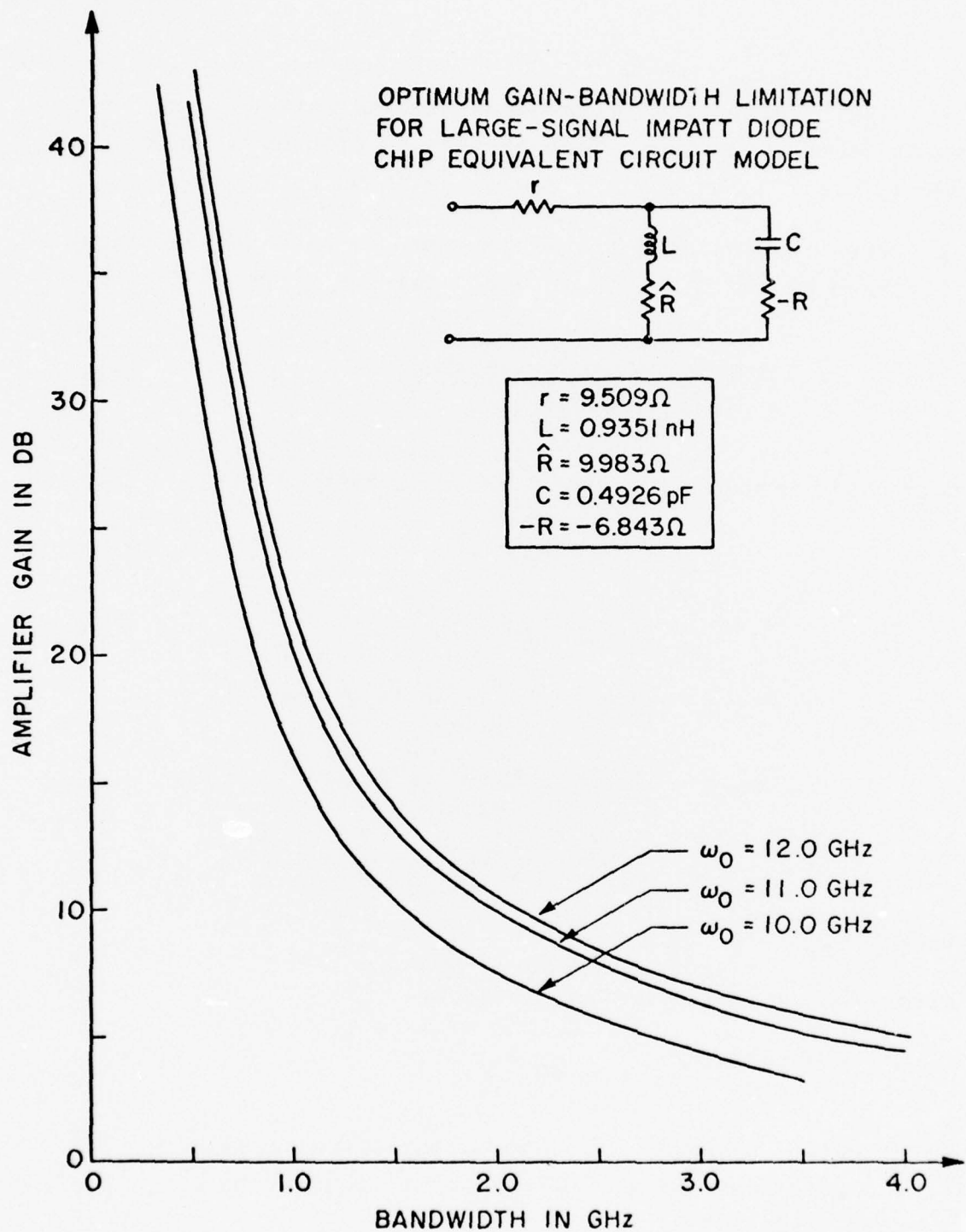
Figure 5. Optimum Gain-Bandwidth Limitations of a typical HP IMPATT Diode with a Center Frequency of $\omega_0 =$ 10, 11, and 12 GHz.
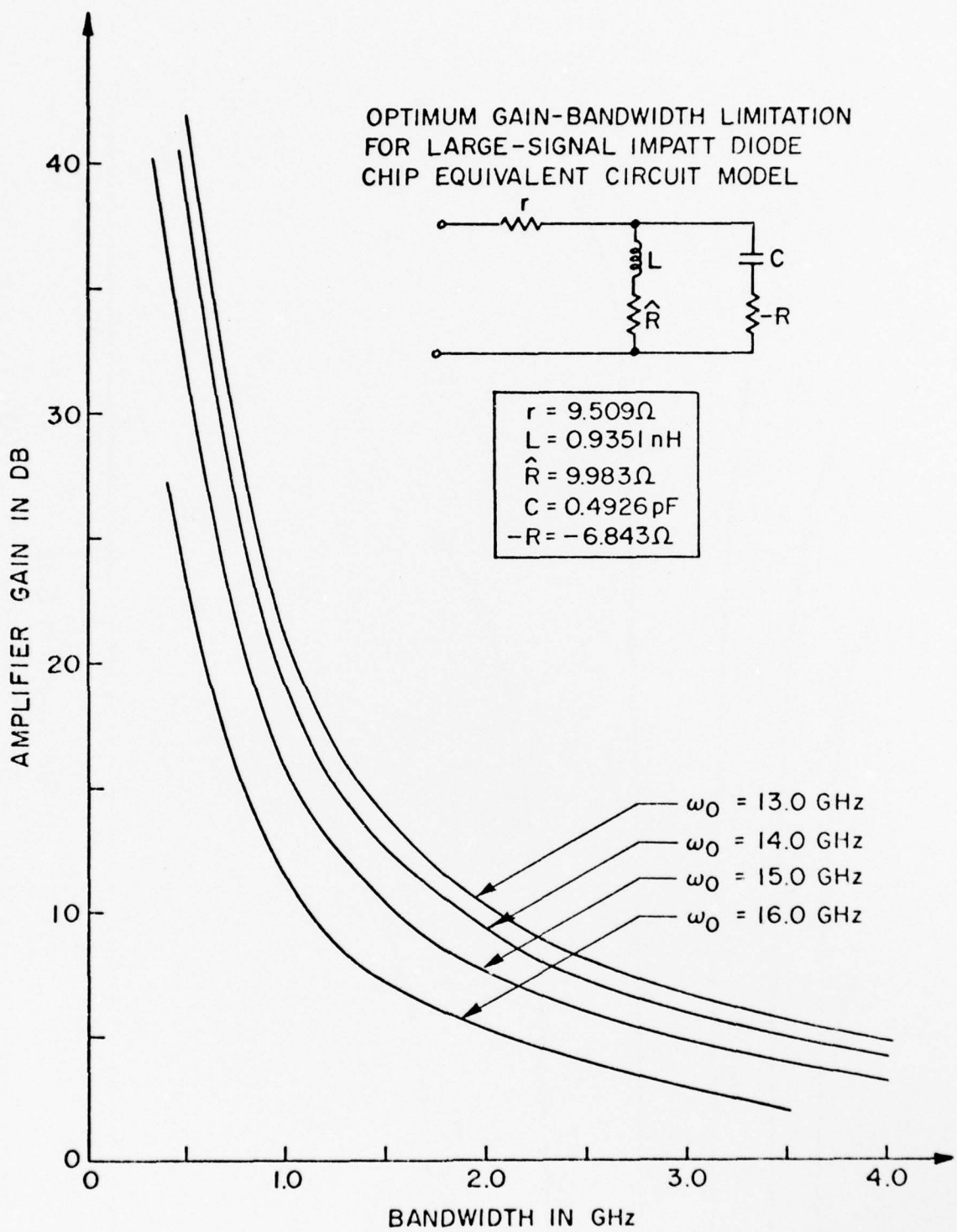
Figure 6. Optimum Gain-Bandwidth Limitations of a typical HP
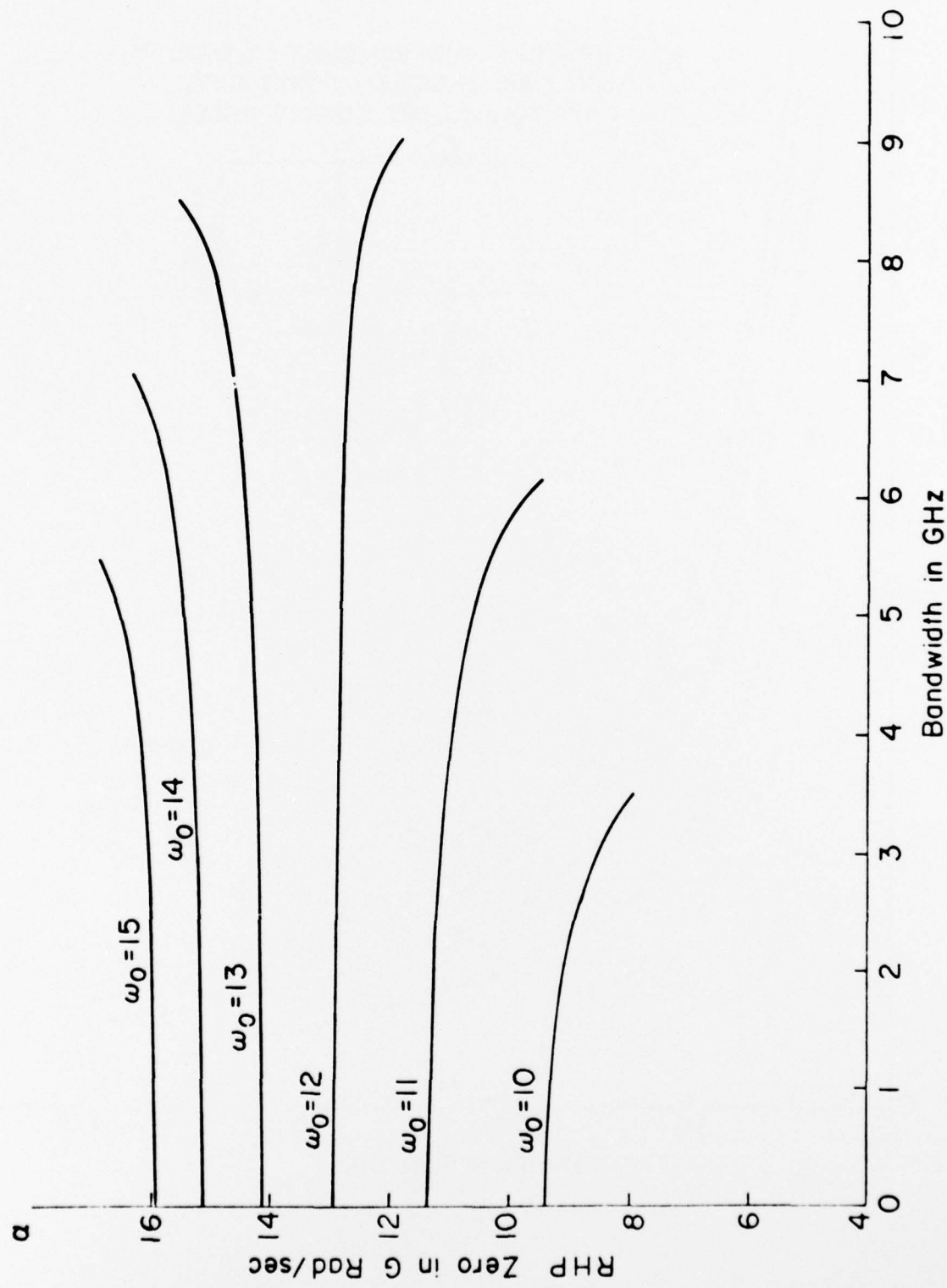IMPATT Diode with a Center Frequency of ω_0=13, 14, 15,
and 16 GHz.

133

Figure 7. Location of the Required Right-Half-Plane Zero to Satisfy the Simultaneous Gain-Bandwidth Integral Constraints.

134

$$P_4(x) = 673.0637 - 3158.8209x + 5537.1061x^2 - 4290.7088x^3 \qquad (81)$$
$$+ 1241.3356x^4 \quad,$$

$$K = 3.5428, \qquad\qquad\qquad (82)$$

$$\alpha = 0.16066 \quad.$$

Using now the analytic approximation method presented in the previous section, the approximation polynomial and parameters K, α are given by

$$P_4(x) = 673.4298 - 3160.0275x + 5539.3348x^2 - 4292.2165x^3$$
$$+ 1241.6992x^4, \qquad\qquad (84)$$

$$K = 3.5532 \quad, \qquad\qquad\qquad (85)$$

$$\alpha = 0.16080 \quad. \qquad\qquad\qquad (86)$$

The configuration of the amplifier is shown in Figure 8. The gain functions are plotted in Figure 9.

By factorizing the gain functions $G(\omega^2)$'s to obtain the corresponding $Z(p)$'s, the element values of the matching network are presented in the following table:

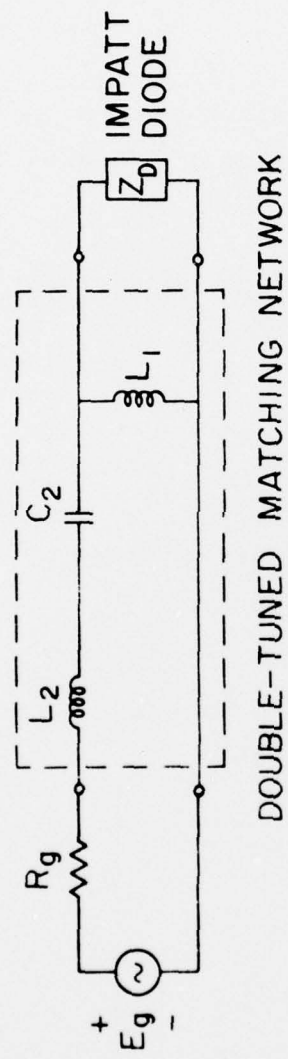| Element	Numerical Method	Analytic Approximation
L_1 (nH)	0.44918	0.44857
c_2 (pF)	0.01846	0.01846
L_2 (nH)	8.1944	8.1979
R_g (Ω)	139.088	139.266

Figure 8. Double-Tuned (n=2) Matching Network for IMPATT Diode Reflection Amplifier.
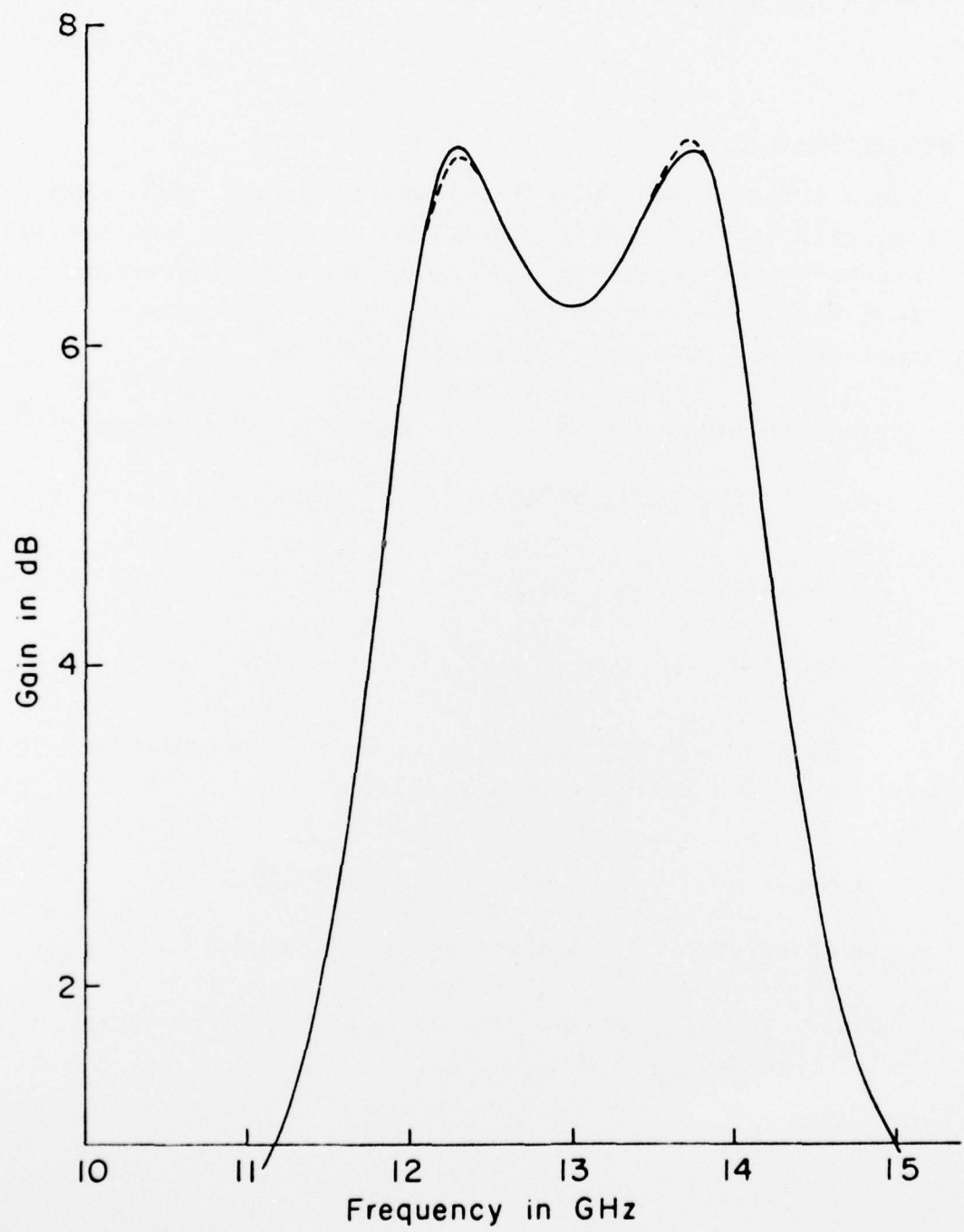
Figure 9. Gain Functions of a Typical Double-Tuned IMPATT
Reflection Amplifier.

137

The   gain   responses of the double-tuned IMPATT reflection amplifiers are plotted in Figure 10.

Design Example 2:

For a triple-tuned reflection amplifier (n=6, m=3) with the same silicon double-drift IMPATT diode and the same operating band and passband ripple, we can employ the computer program to obtain the approximation polynomial $P_6(x)$, the gain constant, and the RHP zero, which are given by

$$P_6(x)=9.21365x10^4-6.48333x10^5x+1.89635x10^4x^2-2.95122x10^6x^3$$

$$+2.5735x10^6x^4-1.19759x10^6x^5+2.31313x10^5x^6 \quad , \qquad (87)$$

$$K = 5.59486 \quad , \tag{88}$$

$$\alpha = 0.160609 \quad . \tag{89}$$

The configurations of the amplifier is shown in Figure 11. The element values are listed in the following

$$L_1 = 0.44867 \text{ nH}, \quad C_2 = 0.00786 \text{pF}, \quad L_2 = 19.229 \text{nH},$$

$$C_3 = 0.32314 \text{ pF}, \quad L_3 = 0.46704 \text{nH}, \quad R_g = 189.34\Omega \quad .$$

The   gain   response of the triple-tuned IMPATT reflection amplifier is presented in Figure 12.
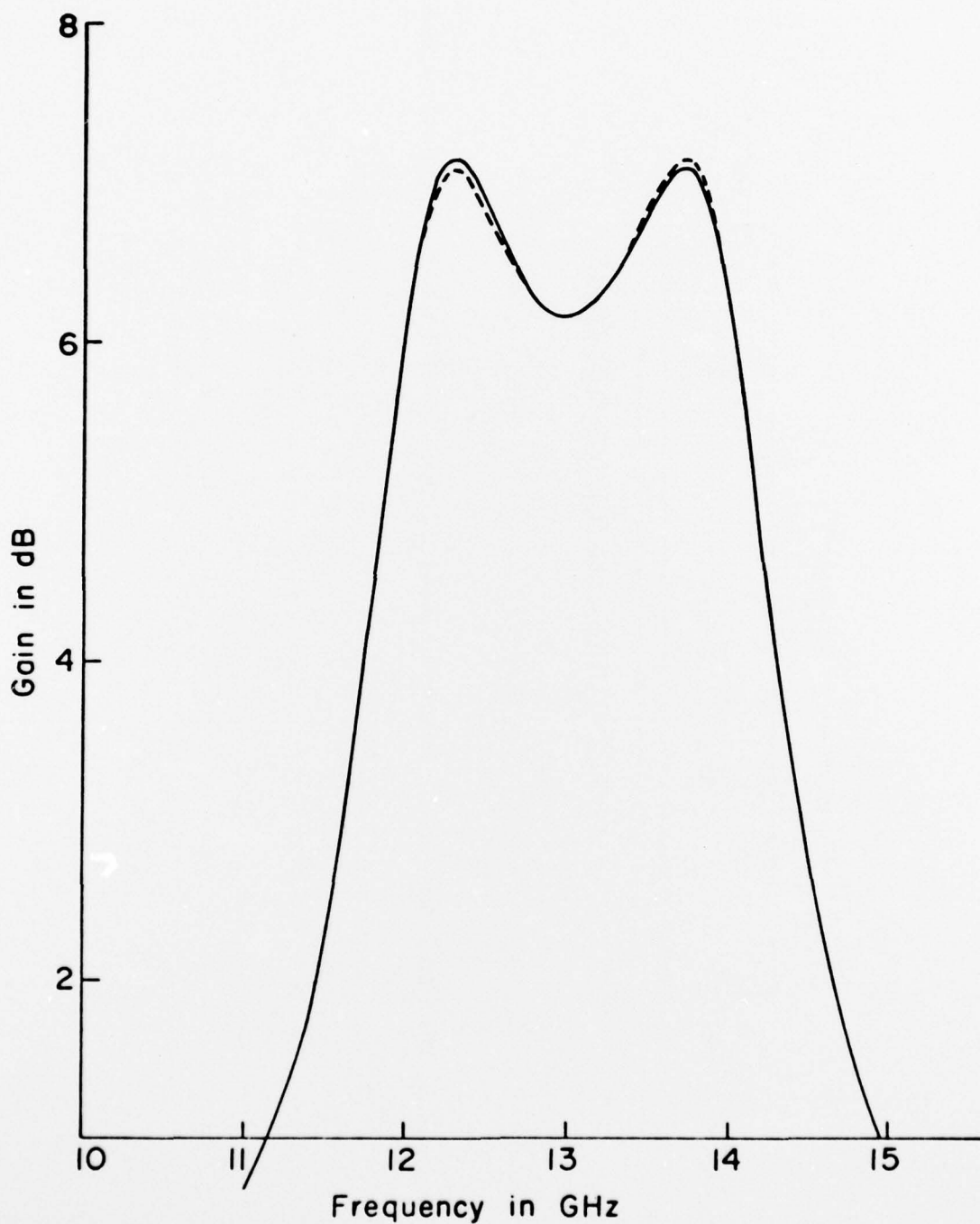
Figure 10.   Gain Response of a Typical Double-Tuned IMPATT Reflection
Amplifier.
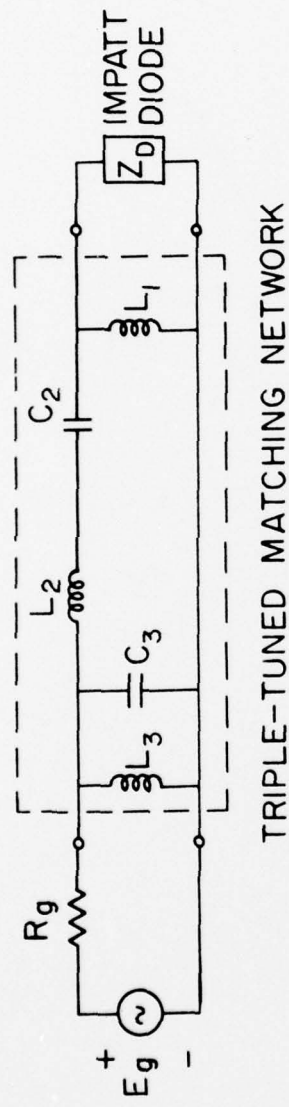
139

TRIPLE-TUNED MATCHING NETWORK

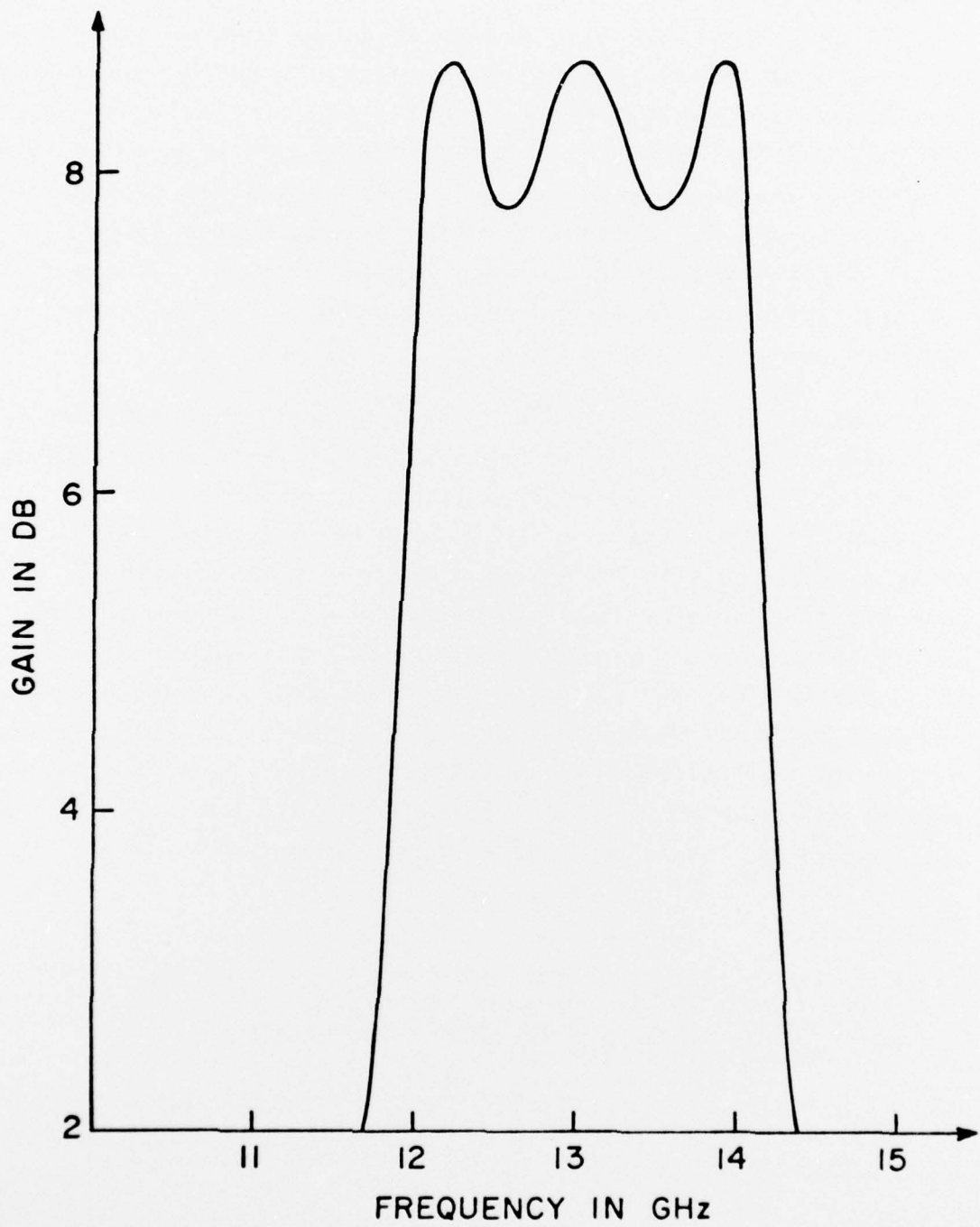Figure 11. Triple-Tuned (n-3) Matching Network for IMPATT Diode Reflection Amplifier.

Figure 12. Gain Response of a Typical Triple-Tuned Reflection Amplifier.

141

Conclusions

In this report we have presented an optimum design theory for broadband IMPATT reflection amplifiers based on a lumped frequency-independent 5-element equivalent circuit model of the IMPATT diode. This rigorous design theory is more general than the presently available design techniques and provides an exact design for broadband reflection amplifiers with either maximally-flat or equiripple gain responses. Computer-aided optimization is needed only to correct for the inaccuracy in the model.

Explicit analytical results have been derived for the maximally-flat case and the equiripple case with a simplifying assumption to obtain an analytical approximation. Without invoking the approximation, results have been obtained by using a computer program to solve the exact equiripple approximation problem together with the simultaneous integral constraints imposed by the IMPATT diode. For practical IMPATT diode parameters, the analytical results are very close to the exact solutions. Design examples for double- and triple-tuned reflection amplifiers using a typical Hewlett-Packard silicon double-drift IMPATT diode characteristics are presented in this report to illustrate the general design techniques.

References:

1. M.S. Gupta, "Large-Signal Equivalent Circuit for IMPATT-diode Characterization and its Application to Amplifiers," IEEE Trans. on Microwave Theory and Techniques, Vol. MTT-21, pp. 689-694, November 1973.

2. W. H. Ku and E. R. Scherer, "Gain-Bandwidth Optimization of Avalanche Diode Amplifiers," IEEE Transactions on Microwave Theory and Techniques, Vol. MTT-18, pp. 932-942.

3. R. M. Fano, "Theoretical Limitations on the Broadband Matching of Arbitrary Impedance," Journal of the Franklin Institute, Vol. 249, pp. 57-83, Jan. 1950, pp. 139-155, Feb. 1950.

4. D. C. Youla, "A New Theory of Broadband Matching," IEEE Transactions on Circuit Theory, Vol. CT-11, pp. 30-50, March 1974.

5. Y. T. Chan and E. S. Kuh, "A General Matching Theory and its Application to Tunnel Diode Amplifiers," IEEE Trans. on Circuit Theory, Vol. CT-13, No. 1, pp. 6-18, March 1966.

6. Wendell C. Petersen, "Analytical and Computer-Aided Design Techniques for Bipolar and FET Transistor Amplifiers," Ph.D. Thesis, Cornell University, Ithaca, NY, January 1976.

7. C. B. Sharpe, "A General Tchebycheff Rational Function," Proc. IRE, Vol. 42, Feb. 1954, pp. 454-457.

8. Sidney Darlington, "Aanalytical Approximations to Approximations in the Chebyshev Sense," Bell Syst. Tech. Journal, Vol. 49, pp. 1-32, Jan. 1970.

The Growth and Evaluation of Thin GaAs Layers for Use in
Microwave FET's.

H. Morkoc[*], L. F. Eastman[**]

Early work yielded two epitaxial layers 1μm thick with
$2 \times 10^{16}/cm^3$ electron concentration for use by R. Gurney in longer
gate devices. More recent work has yielded four epitaxial
layers about .3 microns thick and with $9 \times 10^{16}/cm^3$ electron
concentration for use in shorter gate devices. The substrates
used were supplied by Wright Patterson Air Force Base personnel,
as part of a sponsored program at Laser Diode Corporation, and
were cut 3° off the [100] in the [110].

Measurements were made of pinch-off voltage to see if
repeatable and uniform thickness epitaxial layers were being
produced. The latter four wafers were the correct thickness.
In some earlier cases the layers were thicker than predicted
and needed to be etched down.

Finally, layers were sent to a few industrial laboratories,
for processing into FET devices, using their techniques. Bell
Laboratories made 500 μm gate width and .8μm gate length
devices with one of our layers with a buffer. The mutual
transconductance was 60 millimhos, which compares well with
the range of 40-60 millimhos gotten with their own VPE material.
No looping of the I-V curve occurred in the dark, in contrast
to the VPE material. Finally, microwave noise figure measure-
ments were made at 6 GHz yielding 2.3 -2.6 db, compared to
1.3 - 1.6 db for state of the art results at Bell Laboratories.
The lowest noise figure was gotten with our material at 25%
of I_{DSS} current, whereas 10-15% of I_{DSS} current is normally
the value for lowest noise. The buffer layer had 10,000Ω

sheet resistance and was 5μm thick. This value should eventually be raised more than an order of magnitude for best results.

This project is now complete.

Experimental and Theoretical Studies of Ion-Implanted
Silicon Read IMPATT Diode

Richard Kwor, G. C. Dalman[*], C. A. Lee[*]

This research has been completed and a final report
has been prepared. The following is an Abstract:

The Properties of an X-band silicon Read IMPATT diode were
studied both experimentally and theoretically. Diodes with a
structure of $p^+n\nu n^+$ were fabricated using ion-implantation
techniques. Phosphorus was implanted into the ν on n^+ epitaxial
wafers as the n-region dopant. Boron was then implanted as
the p^+ contact. The implanted wafer was annealed at 950°C for
half an hour. Diodes were fabricated and were subjected to various
microwave tests, including noise, reflection amplifier and
oscillator measurements. As an oscillator, the implanted diode
showed an efficiency of 8.4% at 200 A/cm^2 bias current density.
It was found that, as a result of high reverse saturation
current, the phase lag angle between the avalanche particle
current and the external field excitation is less than the ideal
value of 90°. This was the principal cause for the lower-than-
expected efficiency.

*Project Supervisor

MISSION
of
Rome Air Development Center

RADC plans and conducts research, exploratory and advanced development programs in command, control, and communications (C^3) activities, and in the C^3 areas of information sciences and intelligence. The principal technical mission areas are communications, electromagnetic guidance and control, surveillance of ground and aerospace objects, intelligence data collection and handling, information system technology, ionospheric propagation, solid state sciences, microwave physics and electronic reliability, maintainability and compatibility.